International Journal of Biological Macromolecules 310 (2025) 143157

Contents lists available at ScienceDirect

International Journal of Biological Macromolecules

journal homepage: www.elsevier.com/locate/ijbiomac

Potent HIV-1 miniprotein inhibitors targeting highly conserved gp41 epitopes

Daniel Polo-Megías [a], Mario Cano-Muñoz [a,1], Pierre Gantner [b], Géraldine Laumond [b], Thomas Decoville [b], Jasmine Grezzani [a], Ilaria La Rocchia [a], M. Carmen Salinas-Garcia [a], Ana Cámara-Artigas [c], José A. Gavira [d], Francisco Conejero-Lara [a,*], Christiane Moog [b,e,**]

[a] Departamento de Química Física, Instituto de Biotecnología e Unidad de Excelencia de Química Aplicada a Biomedicina y Medioambiente (UEQ), Facultad de Ciencias, Universidad de Granada, 18071 Granada, Spain
[b] Laboratoire d'ImmunoRhumatologie Moléculaire, Institut National de la Santé et de la Recherche Médicale (INSERM) UMR_S 1109, Institut Théematique Interdisciplinaire (ITI) de Médecine de Précision de Strasbourg, Transplantex NG, Faculté de Médecine, Fédération Hospitalo-Universitaire OMICARE, Fédération de Médecine Translationnelle de Strasbourg (FMTS), Université de Strasbourg, F-670.00 Strasbourg, France
[c] Department of Chemistry and Physics, University of Almería, Agrifood Campus of International Excellence (ceiA3), Research Centre for Agricultural and Food Biotechnology (BITAL), Carretera de Sacramento s/n, Almería, 04120, Spain
[d] Laboratorio de Estudios Cristalográficos, IACT-CSIC, Armilla, 18100 Granada, Spain
[e] Vaccine Research Institute (VRI), F-94000 Créteil, France

ARTICLE INFO

Keywords:
Fusion inhibitors
Antivirals
Chimeric proteins

ABSTRACT

The viral envelope glycoprotein (Env) mediates HIV entry to the cell. During this process, its gp41 subunits must assemble into a highly stable six-helix bundle (6HB) by association between their N-terminal and C-terminal heptad repeats (NHR or HR1 and CHR or HR2, respectively), bringing the viral and cell membranes into close proximity. Further interactions involving the gp41 fusion peptide and the membrane proximal external region (MPER) facilitate membrane fusion. Disrupting 6HB formation is a strategy to inhibit HIV. Previously, we reported chimeric miniproteins (termed covNHR-N) that mimic the first half of gp41 NHR and potently inhibit HIV-1. Stabilization of these miniproteins with disulfide bonds was essential for high inhibitory activity. Here, we introduce newly designed covNHR-N miniproteins, further stabilized by polar-to-hydrophobic mutations. Moreover, we incorporated additional structural motifs that interact with the MPER, a target of broadly neutralizing antibodies (bNAbs). These novel miniproteins showed increased binding affinity for gp41-derived peptides and improved HIV-1 inhibitory activity, particularly against infectious primary viruses on peripheral blood mononuclear cells (PBMC). Furthermore, they exhibited strong synergy with bNAbs and reduced HIV-1 replication in *ex vivo* experiments with cells from infected donors. These miniproteins could be developed as part of drug compositions against HIV-1.

1. Introduction

HIV-1 infection continues to be a global health issue, with >37 millions of people living with the virus, and over 600,000 deaths per year, directly or indirectly associated with the infection. AIDS remains one of the leading causes of death in underdeveloped countries, and the rate of new infections remains remarkably high, with 1.0–1.7 million cases per year [1]. Despite decades of efforts to develop an effective, safe, and affordable HIV vaccine, only a few vaccine candidates have reached phases IIb or III of clinical trials, with little to no efficacy [2]. Meanwhile, antiretroviral therapies (ART) have significantly improved the life expectancy of HIV-infected patients by reducing the viral load to

* Corresponding author.
** Correspondence to: C. Moog, Laboratoire d'ImmunoRhumatologie Moléculaire, Institut National de la Santé et de la Recherche Médicale (INSERM) UMR_S 1109, Institut Théematique Interdisciplinaire (ITI) de Médecine de Précision de Strasbourg, Transplantex NG, Faculté de Médecine, Fédération Hospitalo-Universitaire OMICARE, Fédération de Médecine Translationnelle de Strasbourg (FMTS), Université de Strasbourg, F-670.00 Strasbourg, France.
E-mail addresses: conejero@ugr.es (F. Conejero-Lara), c.moog@unistra.fr (C. Moog).
[1] Present address: Department of Biotechnology and Environmental Protection, Estación Experimental del Zaidín, Consejo Superior de Investigaciones Científicas, Granada, 18,008, Spain.

https://doi.org/10.1016/j.ijbiomac.2025.143157
Received 29 January 2025; Received in revised form 11 April 2025; Accepted 12 April 2025
Available online 14 April 2025

undetectable levels, keeping the virus latent and integrated into the DNA of infected cells, and turning AIDS into a chronic disease [3]. Nevertheless, the emergence of multidrug-resistant viral strains and, in some cases, serious drug interactions necessitate expanding the repertoire of therapeutic approaches targeting different stages of the HIV-1 replication cycle.

A widely pursued strategy to combat HIV-1 is inhibiting its entry into the cells mediated by the envelope glycoprotein (Env). Inhibiting viral entry before integration is highly recommended to prevent the establishment of new viral reservoirs, one of the major challenges for achieving HIV cure. Env is a non-covalently associated trimer of heterodimers composed of two glycoprotein subunits, gp120 and gp41, which decorate the viral membrane [4]. In its pre-fusion state, the three gp120 subunits cover the transmembrane gp41 subunits, stabilizing them in a closed, spring-loaded metastable conformation. Attachment of the virus to the host cell begins with gp120 binding to the CD4 receptor. This event induces a secondary binding to a co-receptor (CCR5 or CXCR4), which triggers gp41 release and the insertion of its N-terminal fusion peptide (FP) into the cell membrane. This is followed by a series of conformational changes that ultimately lead to the formation of a more energetically favorable conformation, known as the 6-helix bundle (6HB), formed by the N-terminal heptad repeat (NHR or HR1) and C-terminal heptad repeat (CHR or HR2) regions of gp41. In this 6HB structure, three CHR regions associate externally over an inner helical coiled-coil NHR trimer in an antiparallel orientation, thus bringing the viral and host-cell membranes into proximity. The helical zippering between NHR and CHR extends toward the membrane external proximal region (MPER) and the fusion peptide proximal region (FPPR) of gp41, promoting lipid mixing and eventually causing membrane fusion. Consequently, compounds that interact with these gp41 regions interfere with this key process and thereby constitute HIV fusion inhibitors.

HIV-1 infection rapidly elicits non-neutralizing antibodies (Abs) within just a week, while neutralizing antibodies against variable regions of gp120 emerge between 3 to 12 months. The virus readily escapes the selection pressure exerted by strain-specific Ab responses. Only a small percentage of infected people develop potent Ab responses of the type associated with the most effective broadly neutralizing Abs (bNAbs). These bNAbs recognize a few conserved epitopes shared across virus subtypes and isolates, including the variable loops at the trimer apex, the CD4 binding site, a gp120 glycan epitope, the gp120-gp41 interface, and the gp41 MPER [5,6]. Passive immunotherapy based on bNAbs is a promising strategy for treating or preventing HIV-1 infection, and some of these Abs have advanced to clinical trials [7]. They are being tested in "shock and kill" strategies, to suppress HIV rebound following treatment with latency-reversing agents (LRAs) [8]. However, serious challenges remain, such as viral load rebound, the emergence of bNAb-resistant strains, and reduced efficacy in cell-to-cell transmission.

Due to its key role in the fusion process and high sequence preservation, the gp41 MPER contains highly pursued epitopes for HIV neutralization mediated by antibodies [9,10]. Among these, 2F5 and 4E10 have been studied for decades as leads for vaccine design. These bNAbs recognize their MPER epitopes aided by their binding to the viral membrane through their long CDR H3 loops [11]. Despite extensive efforts, no vaccine or immunization strategy has induced robust MPER bNAb responses. To explain this, it has been argued that the MPER is highly flexible, conformationally complex [12], and sterically constrained [13], making immunogen design targeting these epitopes particularly challenging.

We have previously shown that the C-terminal half of CHR, located immediately upstream of the MPER, can be targeted by small chimeric proteins (named covNHR-N) that mimic the gp41 NHR in a stabilized three-helix bundle conformation [14]. The small size of these miniproteins (approximately 12 kDa) makes them particularly suitable for accessing CHR epitopes that are partially occluded by glycans and sterically constrained by the narrow ectodomain-membrane space. We demonstrated that the inhibitory activity of these miniproteins does not rely on the interaction involving the conserved NHR hydrophobic pocket and the CHR pocket-binding domain [15], but solely on their binding to the C-terminal half of CHR, which is also highly conserved (Fig. S1). Moreover, the inhibitory potency of these small NHR mimics is strongly correlated with their structural stability [16].

In this work, we further stabilized the covNHR-N miniprotein by substituting three buried glutamine residues with isoleucine, resulting in a hyper stable miniprotein. Subsequently, we used this miniprotein as a stable scaffold to graft additional FPPR motifs, extending its interaction toward the gp41 MPER region. The newly designed miniproteins exhibited enhanced binding affinity for a modified version of the T20 peptide (enfuvirtide) [17], which includes part of the MPER. All miniproteins demonstrated potent and broad HIV inhibitory activity in standard *in-vitro* cell infection assays. Remarkably, the inhibitory activity of the miniproteins was especially high against the infection of peripheral blood mononuclear cells (PBMC) with primary virus isolates, showing efficacy comparable to that of the best bNAbs. Additionally, the miniproteins inhibited virus reactivated *ex vivo* from CD4 T cells isolated from HIV infected patients. Furthermore, they exhibited considerable synergy with bNAbs in combination inhibition assays. These results highlight the potential of these miniproteins as highly promising anti-HIV molecules.

2. Materials and methods

2.1. Protein and peptide samples

Modelling was carried out using SwissPDBviewer [18] and YASARA Structure [19], using as a template the previously reported crystallographic structure of the complex between the C34 peptide and a covNHR protein (PDB entry 6R2G) [20]. Miniproteins mimicking the N-terminal half of gp41 NHR had been previously modelled, incorporating disulfide bonds that tether each loop to its neighboring chain end (covNHR-N-dSS) [16]. Stabilizing mutations and FPPR extensions were computationally designed, as described in more detail in the Results section and Supplementary Appendix S1. The amino acid sequences of the miniproteins and their physical properties are listed in Tables S1 and S2. Alphafold 2 was used *via* the Colabfold server [21] to predict the three-dimensional structures of the miniproteins.

The DNA encoding the sequences of the miniproteins were synthesized and cloned into pET303 expression vectors (Thermo Fisher Scientific, Waltham MA). The sequences (Table S1 in the Supplementary Information) included an N-terminal methionine and a C-terminal six-histidine tag, with the sequence GGGGSHHHHHH. The proteins were overexpressed in *E. coli* BL21 (DE3) cells transformed with the plasmids. Protein purification was performed using nickel-tag affinity (NTA) chromatography, followed by cation exchange chromatography, as previously described [22]. The purity and identity of the proteins were assessed by SDS-PAGE and mass spectrometry. Pure protein aliquots were stored frozen at −80 °C. For biophysical characterization, the protein solutions were extensively dialyzed against the appropriate buffer and centrifuged at 4 °C for 30 min in a benchtop microcentrifuge before concentration measurement.

Synthetic peptides derived from the gp41 CHR sequence were obtained from Genecust (Boynes, France) with a purity >95 %, in *N*-acetylated and C-amidated form. Stock peptide solutions were freshly prepared by weighing the required amount of lyophilized peptide and dissolving it in the appropriate buffer. Thereafter, the pH was measured and adjusted, if necessary, using diluted HCl or NaOH, followed by centrifugation at 4 °C for 30 min in a microcentrifuge to remove any insoluble material. The final peptide concentration was measured spectrophotometrically. Protein-peptide mixtures were prepared by adding the required volume of peptide stock solution to the previously prepared protein sample. Protein and peptide concentrations were measured by UV absorption at 280 nm, using extinction coefficients calculated based on their respective amino acid sequences with the

ExPasy ProtParam web server (https://web.expasy.org/protparam/ accessed on 5 February 2024) [23]. However, the T20-4R peptide exhibited anomalous UV absorption at pH 3.0, requiring its extinction coefficient to be corrected by a factor of 1.45, as determined by NMR using potassium hydrogen phthalate as an internal reference. All samples were freshly prepared and immediately used in experiments.

2.2. Circular dichroism (CD)

CD spectra were recorded in a Jasco J-715 spectropolarimeter (Jasco, Tokyo, Japan) equipped with a Peltier thermostatic cell holder. Far-UV CD spectra (260–200 nm) were measured using a 1-mm pathlength quartz cuvette at a protein concentration of approximately 15 μM. Spectra were recorded at a scan rate of 100 nm/min, 1-nm step resolution, 1-s response, and 1-nm bandwidth. The resulting spectra were usually the average of five scans. For thermal melting experiments, the CD signal was monitored as a function of temperature at 222 nm. Each spectrum was baseline-corrected by subtracting the blank spectrum obtained with the buffer. Finally, the CD signal was normalized to molar ellipticity ([θ], in deg.·dmol^{-1}·cm^2). Binding experiments with CHR peptides were conducted at a 1:2 molar ratio between the proteins and the corresponding peptide.

2.3. Dynamic light scattering (DLS)

Particle size distributions of the covNHR-N miniproteins were assessed by DLS measurements using a DynaPro MS-X instrument (Wyatt, Santa Barbara, CA, USA). DLS data were measured at 25 °C with an average number of 50 acquisitions and an acquisition time of 10 s.

2.4. Differential scanning calorimetry (DSC)

DSC experiments were carried out in PEAQ-DSC or VP-DSC microcalorimeters equipped with autosamplers (Malvern Panalytical, Malvern, UK). Scans were typically performed from 5 to 120 °C, at a scan rate of 90 °C·h^{-1} and a protein concentration of 30 μM, unless stated specifically. Instrumental baselines were recorded before each experiment with both cells filled with buffer and subtracted from the experimental thermograms of the protein samples. Consecutive reheating runs were performed to assess the reversibility of thermal denaturation. The excess heat capacity (ΔC_p) relative to the buffer was calculated from the experimental DSC thermograms using Origin software (OriginLab, Northampton, MA) and normalized per mole of protein. In experiments with protein-peptide mixtures, the excess heat capacity of the free peptide was measured independently and subtracted from the thermograms of the mixtures.

2.5. Isothermal titration calorimetry

ITC measurements were carried out using a Microcal VP-ITC microcalorimeter (Malvern Instruments, Worcestershire, UK). The protein solutions were typically titrated with 25–30 injections of 7.5 μL of the peptide solution at 480 s intervals. Protein concentration in the cell was ~10 to 15 μM, while the ligands in the syringe were typically ~125 μM for T20-4R and ~ 180 μM for Y24L. The experiments were carried out in 50 mM sodium phosphate buffer, pH 7.4, or 50 mM glycine/HCl buffer, pH 3.0, at 25 °C, as stated in each experiment. The experimental thermograms were baseline corrected, and the peaks were integrated to determine the heats produced by each ligand injection. Each heat was then normalized per mole of added ligand. The resulting binding isotherms were fit using a binding model of identical and independent sites, allowing the determination of the binding constant, K_b, the binding enthalpy, ΔH_b, and the binding stoichiometry, n, for each interaction. The heat of dilution of the ligand was estimated from the final heats of the titrations, once the protein was saturated, and included as a fitting parameter. From the fitting parameters, the Gibbs energy and entropy of binding could be derived as $\Delta G_b = -RT \cdot \ln K_b$ and $T \cdot \Delta S_b = \Delta H_b - \Delta G_b$.

2.6. X-ray crystallography

Freshly purified Q23I-ex2 was dialyzed against 10 mM Tris pH 7.5 buffer and concentrated to 5 mg·mL^{-1}. Crystallization conditions were screened by the sitting-drop vapor-diffusion method using commercial screening kits Structure 1 and 2 Eco Screen from Molecular Dimensions (Suffolk, UK). 2 μL of complex solution and 2 μL of reservoir solution were mixed and equilibrated at 298 K against 200 μL reservoir solution in 48-well MRC Maxi Optimization plates (Cambridge, UK). Several favorable conditions were identified and further optimized to obtain protein crystals. The best diffracting crystals were obtained in 0.1 M sodium phosphate monobasic monohydrate, 0.1 M potassium monobasic phosphate, and 2 M sodium chloride.

Before data collection, Q23I-ex2 crystals were soaked in a cryoprotectant solution (30 % PEG200) and flash-cooled in liquid nitrogen. Data sets were collected at 100 K at the beamline XALOC at the ALBA synchrotron (Barcelona, Spain), using a wavelength of 0.979 Å [24]. Diffraction data were indexed and integrated with XDS in the AutoPROC toolbox [25]. Data scaling was performed using the program Aimless from the CCP4 suite [26]. Data collection statistics are shown in Table S3. Solution and refinement of the structures were performed using the PHENIX suite [27]. Molecular-replacement phasing using PHASER [28] was performed with the coordinates of the crystallographic structure of covNHR in complex with the synthetic CHR peptide C34 (PDB entry 6R2G [20]). Manual model building was performed using COOT [29]. Refinement was performed using phenix.refine in PHENIX [30]. To model flexible regions of the protein, ensemble refinement (ER) was performed with phenix.ensemble_refinement [31]. ER is a structure determination method that samples alternate conformations through molecular-dynamics (MD) simulations that are restrained by crystallographic data, and generates structural ensembles that better represent the conformational diversity of biomolecules compared to traditional single-structure models. For this purpose, the refined final model was used as initial coordinates, and the resulting 100 models were analyzed. The quality of the structure was checked using Molprobity [32]. Structural refinement statistics are collected in Table S3. All residues fall within the allowed region of the Ramachandran plot. The protein coordinates were deposited at the Protein Data Bank under the accession code 9HS7.

2.7. Binding assays to Env spike

The capacity of the covNHR miniproteins to bind soluble HIV-1 envelope protein (Env) was determined by ELISA, as previously described [14]. Briefly, 96-well ELISA plates (Maxisorp, Nunc) were coated at 4 °C overnight with 0.5 μg/mL Env gp160 MN/LAI (a hybrid oligomeric gp160 Env with gp120 derived from HIV-1 MN and gp41 derived from HIV-1 LAI). After washing and saturation with 2 % BSA, 0.05 % Tween in PBS for 1.5 h at 25 °C, 0.02 μM of covNHR molecules were added and incubated for 2 h at room temperature. The plate was then washed five times and covNHR binding was detected with 100 μL anti-6× His-tag antibody conjugated to horseradish peroxidase (HRP) (Abcam, Cambridge, UK). Antibody binding was then revealed with tetramethylbenzidine (TMB) substrate buffer, the reaction was stopped with 1 M H_2SO_4 and optical density was read at 450 nm with a Molecular Device Plate Reader equipped with SoftMax Pro 6 program. Background binding was measured in plates without Env and subtracted from the data. The percentage of binding was calculated using the readings with wells coated with His-tagged Env incubated with PBS buffer instead of covNHR-N molecules as a control for 100 % binding.

2.8. HIV

The HIV strains used were either pseudoviruses or primary isolates.

The viruses and plasmids were obtained through the NIH HIV Reagent Program, Division of AIDS, NIAID, NIH. Pseudoviruses SF162 and MW965.26 were produced by co-transfection with SF162 or MW965.26 Env plasmids and HIV pSG3 delta Env backbone. Primary isolates of SF162 and 92RW009 strains were produced on PBMC. Virus stocks were titrated to obtain about 20,000 RLU for TZM-Bl assay and 5 to 10 % p24-positive infected cells for the PBMC assay.

2.9. Virus binding assay

We analyzed the capacity of miniproteins to retain whole virus particles, as previously described [33]. Plate wells were coated with each miniprotein at different concentrations and incubated with primary virus particles (Bal, SF162 and 927RW009) at 37 °C for 1 h. After washing, the amount of intact virus captured was quantified by the measurement of p24 by ELISA in the supernatant after virus breakup. 4B3, 246D and polyclonal antibodies were used as positive controls. 2F5 has been described to have limited binding capacity to the whole virus, as its epitope is poorly accessible before conformational modifications caused by binding to CD4 [34].

2.10. Virus inhibition assays

Virus inhibition was analyzed using either the conventional TZM-Bl neutralization assay or a PBMC based assay on primary virus stocks [35,36]. Briefly, TZM-Bl based assay was performed with two pseudo viruses (SF162 of clade B and MW965.26 of clade C) and a primary isolate 92RW009 (clade A). The two pseudo viruses are classified as easy-to-neutralize Tier 1 viruses, therefore efficiently neutralized by bNAbs such as 3BNC117 [37]. PBMC-based assay was performed with SF162 and 92RW009 primary isolates (virus stocks produced on PBMC). 3 days after infection, PBMC were stained for the detection of intracellular p24 to measure the % of infected cells. The inhibitory concentration 50 (IC_{50}) was calculated as the concentration of the molecule required to achieve a 50 % reduction in virus growth. To identify potential miniprotein toxicity, staining was performed using LIVE/DEAD™ Fixable Violet Dead Cell Stain (Molecular Probes) before intracellular p24 staining.

2.11. Combination inhibition assays

Combinations of miniproteins and mAbs were performed with serial dilutions of both molecules at concentrations selected to encompass their respective IC_{50} values. IC_{50}, IC_{70}, IC_{90} and IC_{95} values were calculated for each single molecule and combined molecules. Hill's plots corresponding to the individual and combination molecules were drawn using the constant ratio combination inhibition data. Data were analyzed according to the Chou and Talalay method [38] to calculate the combination index (CI) and the dose-reduction index (DRI). Details of the analysis are described in the Supplementary Appendix S2.

2.12. Ex vivo inhibition assays

2.12.1. Ethics

PBMCs samples (30–50 × 10^6) from 8 viremic participants included in the APRIL study (Analysis of the Persistence, Reservoir and HIV Latency) were used. This monocentric, observational, and prospective study was approved by the institutional review board CPP (Comité de Protection des Personnes) Est I on January the 5th 2023 (2022-A02567-36), and promoted by the University Hospitals of Strasbourg, France (NCT05752318). All participants provided informed consent for the use of their data and samples in biological research. Participant's characteristics are presented in Table S6.

2.12.2. Cell culture

CD4+ T cells were isolated by negative magnetic selection using the EasySep Human CD4+ T Cell Enrichment Kit (StemCell Technology, Cat#19052). Purity was typically >98 %. 5 × 10^6 to 15 × 10^6 CD4+ T cells resuspended at 2 × 10^6 cells/mL in RPMI +10 % Fetal Bovine Serum (FBS) + IL-2 (10 ng/mL) were left resting for 3 days at 37 °C with 5 % CO_2. Cell medium was changed, and cells were split equally into four conditions by adding either: (i) antiretroviral drugs (raltegravir [RAL] + lamivudine [3TC], 200 nM each), (ii) Q23I-ex2 (0.2 μM), (iii) bNAbs (clones 3BNC117 + 10–1074, 1 μg/mL each) and (iv) control (PBS). Cells were then cultured for four additional days, harvested and stained using HIV-Flow [39] allowing to reveal productively infected cells (p24+ cells). Supernatants were collected for HIV-RNA and p24 measurements.

3. Results

3.1. Design of hyper-stable NHR-mimetic miniproteins harboring MPER-binding motif

We started from a previously designed covNHR-N-dSS miniprotein that mimics the N-terminal half of gp41 NHR in a trimeric coiled-coil helical conformation [14,16]. This single-chain miniprotein contains two disulfide bonds tethering each loop with the first and third helix edges. The addition of each disulfide bond increased the melting temperature by about 19–20 °C compared to similar proteins with none or one disulfide bond. Moreover, disulfide bond stabilization strongly and progressively increased HIV-1 inhibitory activity *in vitro* [16]. Accordingly, since there is a strong correlation between the structural stability of the miniproteins and their inhibitory activity, we aimed to further stabilize them. It was previously shown that substituting triads of buried polar amino acids with isoleucine within the NHR coiled coil produces a dramatic stabilizing effect [40,41]. The N-terminal part of gp41 NHR contains two buried glutamine triads (corresponding to Q562 and Q572 in Env sequence numbering) that establish internal hydrogen bond networks involving buried water molecules [20]. While the Q562 side chain actively participates in water-mediated interactions with CHR, Q572 is totally buried within the NHR trimeric coil. We previously showed that substituting this glutamine triad for isoleucine in a covNHR protein produced a stabilization of >40 °C, converting the NHR mimetic protein into a hyper stable protein, while preserving its potent inhibitory activity [41]. Therefore, we decided to introduce similar Gln to Ile mutations (Q23I, Q41I and Q86I) to create a hyperstable covNHR-N miniprotein named covNHR-N-Q23I, for simplicity abbreviated Q23I (Fig. 1).

Then, we used the Q23I miniprotein as a scaffold to graft additional motifs that could interact with the highly conserved MPER region that follows C-terminally the CHR region. To achieve this goal, we based our design on a previously published gp41 construct in fusion intermediate conformation, including the MPER region [42]. This structure (PDB entry 2X7R) shows clearly defined contacts between part of the MPER and part of the fusion peptide proximal region (FPPR), which are organized as splayed helical extensions of the NHR-CHR core. To mimic this interaction in our constructs, we extended N-terminally the NHR helices of our mimetic miniprotein to include several FPPR residues in helical conformation and ligated their ends with appropriate loops (Fig. 1A). Since these helical extensions and the longer loops connecting them will naturally tend to destabilize the structure of the miniprotein, we engineered stabilizing interhelical interactions and recreated the disulfide bond tethering the C-terminus and the new loop (see additional details of the design in Appendix S1 and Figs. S2 and S3 of the Supplementary Information). We designed two new miniproteins with different lengths of the FPPR extensions (named Q23I-ex1 and Q23I-ex2) (Fig. 1). The sequences and molecular characteristics are collected in Tables S1 and S2. The predicted structures of the three miniproteins using Alphafold 2 through the Colabfold web server [21] are very similar to the designed models (Fig. S4).

The three miniproteins were overexpressed in *E. coli*, purified and

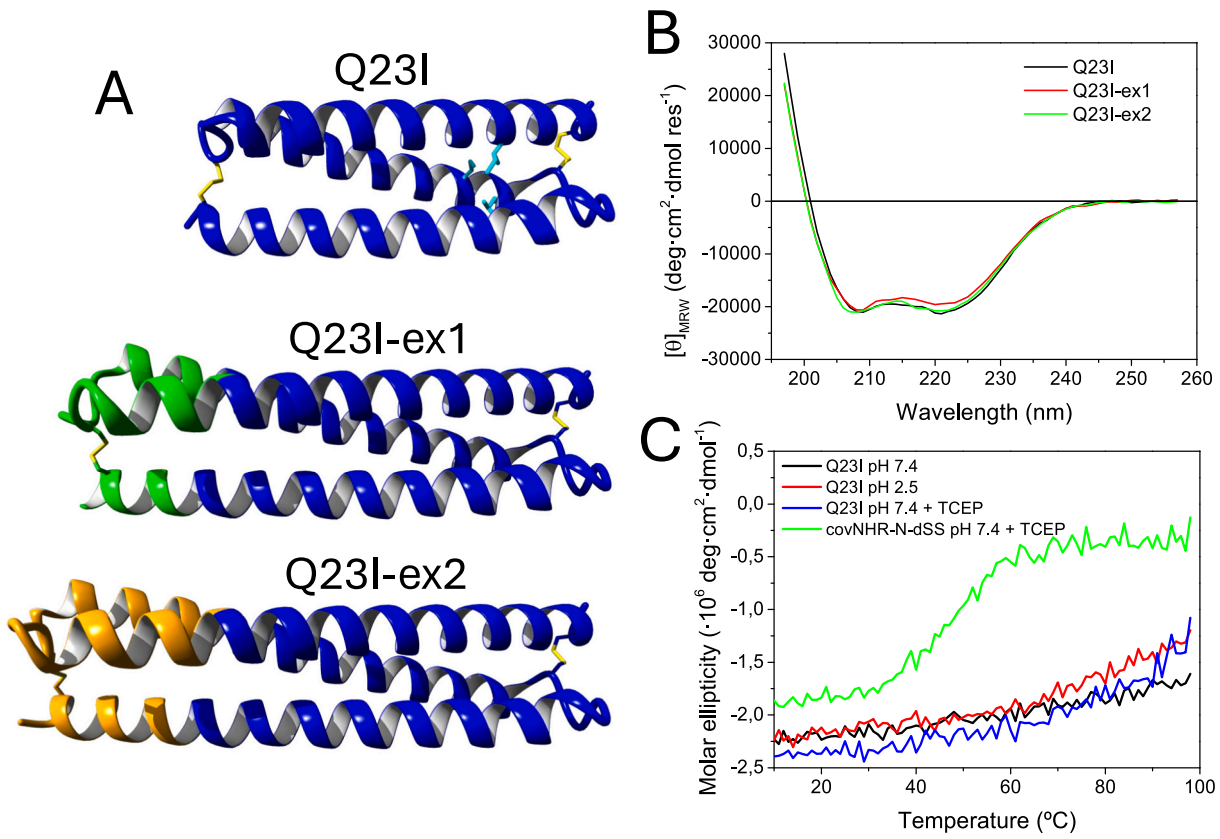

Fig. 1. Design and characterization of covNHR-N miniproteins. (A) Ribbon representation of the designed models. Mutated side chains (Q23I, Q41I and Q86I) in covNHR-N-Q23I and disulfide bonds tethering each chain end with its adjacent loop are highlighted with sticks and colored by atom type. The FPPR extensions in Q23I-ex1 and Q23I-ex2 are colored in green and orange, respectively. (B) Far-UV CD spectra of each miniprotein, showing a typical α-helical structure. Data are presented as mean-residue ellipticity. (C) Thermal unfolding profiles of Q23I and its parent protein covNHR-N-dSS followed by CD at 222 nm.

biophysically characterized. They could all be produced with high yields and were highly soluble, folded in an α-helical structure (Fig. 1B, Table S2), and behaved as monomeric particles in solution according to DLS measurements (Fig. S5). The thermal unfolding profile of the Q23I miniprotein, measured by circular dichroism (CD) at pH 7.4 (Fig. 1C), did not show any unfolding transition within the temperature range explored, from 5 °C to 98 °C, whereas the non-mutated covNHR-N-dSS protein unfolded with a melting temperature (T_m) of about 84 °C [16]. At pH 2.5 or at pH 7.5 in the presence of the reducing agent tris(2-carboxyethyl)phosphine (TCEP), the Q23I protein only showed incipient unfolding near 100 °C due to reduction of disulfide bonds. In contrast, the non-mutated parent protein covNHR-N-dSS unfolded at about 45 °C, at pH 7.4 and in the presence of TCEP, demonstrating a strong stabilization of >50 °C exerted by the triad of Gln-to-Ile mutations. DSC experiments at pH 7.4 and 3.0 showed that the three proteins are highly thermostable, with no discernible unfolding transitions within the explored temperature range (Fig. S6). At pH 7.4, the DSC thermograms showed strong exothermic effects at high temperature, which could be associated with irreversible disulfide bond degradation [43].

To investigate if the miniproteins can bind to the gp41 CHR region, we used a synthetic peptide (named Y24L), which encompasses Env residues Tyr638-Leu661, corresponding approximately to the second half of the CHR region. This CHR peptide is complementary to the NHR region imitated by our covNHR-N miniproteins in the gp41 post-fusion structure [14], and contains a highly preserved CHR polar motif that binds to a N-terminal NHR pocket (Fig. S1). Mixing the Y24L peptide with each miniprotein produced a significant increase in α-helix structure according to the CD spectra (Figs. 2A and S7), indicating that the peptide binds to the miniproteins acquiring an α-helical conformation, whereas in its free form, it is almost unstructured.

Subsequently, we carried out isothermal titration calorimetry (ITC) experiments at pH 7.4 with the Y24L peptide and the three miniproteins (Fig. S8; Table 1). The binding of Y24L to Q23I is strongly exothermic, with a dissociation constant roughly 2.5-fold lower than that measured previously for the covNHR-N-dSS parent protein under identical conditions [16]. The binding enthalpy is slightly more negative, indicating a tighter interaction as a result of the structural stabilization of the miniprotein produced by the Gln-to-Ile mutations. At pH 7.4, the binding affinity of Y24L for the FPPR-extended miniproteins is quite similar to the Q23I miniprotein, as expected, because they expose an identical NHR complementary groove to this peptide.

To test whether the FPPR-extended miniproteins can also interact with the gp41 CHR sequence including MPER residues, we analyzed the binding to the T20 peptide (enfuvirtide; Env residues Tyr638-Phe673) [17], which encompasses the C-terminal half of CHR and the initial part of the MPER, including the putative gp41 core epitope recognized by the bNAb 2F5 [44,45]. However, at pH 7.4, adding T20 to the miniprotein solutions induced a heavy precipitation, as previously observed also for full-length covNHR proteins [20], precluding the study of their interaction under these conditions. We also tested a modified version of T20 (T20-4R) containing four arginine residues at the C-terminus to increase its solubility. However, it produced a similar co-precipitation at pH 7.4. Then, we explored the binding of T20-4R to the covNHR-N miniproteins at other pH values and found that the protein-peptide mixtures remained soluble at pH 3.0 and below. Thus, we decided to characterize their interaction at pH 3.0 to evaluate possible differences in interaction strength that could be attributed to an extended interaction interface involving the FPPR and the MPER regions. The molecular size of the protein-peptide complexes in 1:2 protein:peptide mixtures

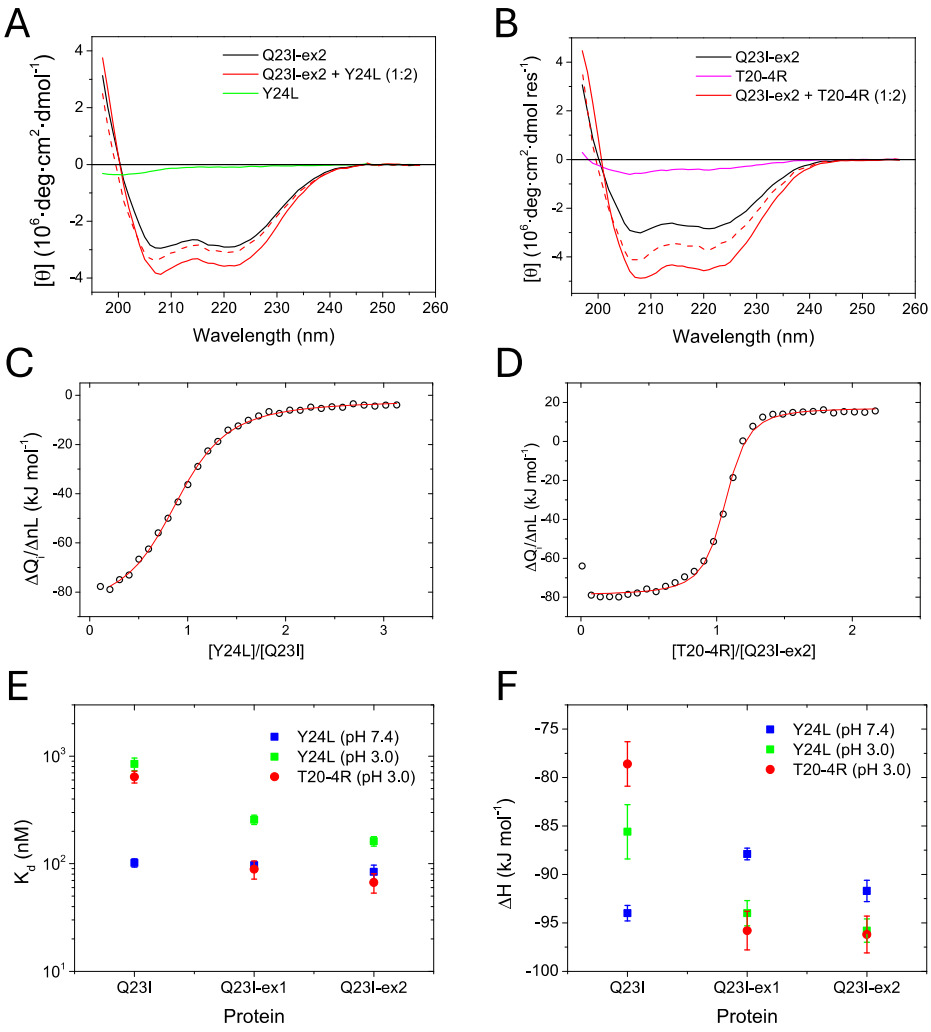

Fig. 2. Binding of the covNHR-N miniproteins to gp41-derived peptides. (A, B): Effect of peptide binding on α-helix structure. (A) Far-UV CD spectra of Q23I in free form and in 1:2 mixture with Y24L peptide at pH 7.4. (B) Far-UV CD spectra of the Q23I-ex2 in free form and in 1:2 mixture with T20-4R peptide at pH 3.0. For comparison, the spectra of the free peptides and the theoretical sum of the spectra (dashed lines) of the free molecules in 1:2 ratio are also shown. (C, D): Binding curves measured by ITC for the titrations at 25 °C and pH 3.0 of Q23I with Y24L peptide (C), and Q23I-ex2 with T20-4R (D). The symbols correspond to the experimental binding heats normalized per mole of added peptide during the titrations. The solid red lines represent the best fits obtained using a binding model of independent and identical sites. (E, F): Dissociation constants (E) and binding enthalpies (F) measured by ITC (Table 1) for each covNHR-N miniprotein and the two peptides.

ruled out formation of high order aggregates at pH 3.0, according to DLS measurements (Fig. S5).

Mixing Y24L or T20-4R with the different miniproteins at pH 3.0 produced considerable increases in negative ellipticity in the far-UV CD spectra, similar to those observed at pH 7.4 (Figs. 2B and S9), once again indicating binding of the peptides to the miniproteins with acquisition of α-helical structure. Notably, at this acidic pH the free T20-4R peptide contains a significant amount of α-helical structure, in contrast with the Y24L peptide, which is mostly unstructured. Despite this, the increase in helical structure formation produced by T20-4R binding to the extended miniproteins appears very similar to that of the shorter Y24L peptide. From the mean-residue ellipticity values at 222 nm, measured for the free molecules and the mixtures [46], we estimated that about 16–22 residues of Y24L form α-helix in the complexes (only 3–4 in the free peptide), whereas 27–33 residues of T20-4R are α-helical in the complexes (12–13 in the free peptide). This result suggests that the MPER region has a high propensity for adopting a helical conformation in the free peptide [47] and remains helical when bound to any of the three proteins.

To further explore the interaction between the miniproteins and the peptides, DSC experiments with protein:peptide mixtures at different molar ratios showed the development of characteristic endothermic transitions corresponding to dissociation of the protein-peptide complexes (Fig. S10), confirming the binding of the peptides to the miniproteins. The dissociation transitions of the Q23I protein with Y24L and T20-4R peptides suggest a slightly less stable complex with the MPER-extended peptide. The protein-peptide complexes of the FPPR-extended miniproteins were more stable than those of Q23I. It is noteworthy that, for each extended miniprotein, the dissociation transition of the T20-4R peptide is shifted toward a higher temperature compared to the Y24L peptide, indicating additional interactions at the FPPR-MPER interface that increase the stability of the complexes. Moreover, Q23I-ex2 forms the most stable complex with T20-4R due to its longer FPPR extension and more extensive interactions with the peptide's MPER region.

To corroborate the differences in peptide binding strength produced by the inclusion of the FPPR-MPER interaction motifs, we carried out isothermal titration calorimetry (ITC) experiments at 25 °C and pH 3.0 with the three miniproteins and the two peptides (Figs. 2C–D and S11). The ITC thermograms revealed exothermic, high-affinity binding for all protein-peptide complexes. The thermodynamic parameters of binding are collected in Table 1. The affinity of Q23I for the Y24L peptide at pH

Table 1
Thermodynamic parameters measured by ITC for the binding of gp41-derived peptides to the covNHR-N miniproteins. Parameters correspond to best fits using a binding model of independent and identical sites. Uncertainties correspond to 95 % confidence intervals of each fitting parameter.

Protein	Peptide	n[a]	K_b[b] ($\cdot 10^6$ M^{-1})	K_d[c] (nM)	ΔH_b[d] (kJ·mol^{-1})
pH 7.4					
covNHR-N-dSS[e]	Y24L	0.89	4.12 ± 0.17	243 ± 10	−90 ± 4
Q23I		0.82	9.8 ± 0.9	102 ± 9	−94.0 ± 0.8
Q23I-ex1		0.81	10.3 ± 0.9	97 ± 8	−87.9 ± 0.6
Q23I-ex2		0.82	11.9 ± 1.8	84 ± 13	−91.7 ± 1.1
pH 3.0					
Q23I	Y24L	0.91	1.18 ± 0.16	850 ± 115	−86 ± 3
Q23I-ex1		0.90	3.9 ± 0.4	257 ± 25	−94.0 ± 1.3
Q23I-ex2		0.88	6.2 ± 0.6	162 ± 16	−95.8 ± 1.2
pH 3.0					
Q23I	T20-4R	0.89	1.55 ± 0.20	643 ± 81	−78.6 ± 2.3
Q23I-ex1		1.03	11.2 ± 0.21	89 ± 17	−95.8 ± 2.0
Q23I-ex2		1.04	15 ± 3	67 ± 14	−96.2 ± 1.9

[a] Apparent binding stoichiometry.
[b] Binding constant.
[c] Dissociation constant.
[d] Binding enthalpy.
[e] Data taken from [16].

3.0 is about 8-fold lower than at pH 7.4, although still within the submicromolar range. This indicates a relatively mild influence of pH in the NHR-CHR interaction. The binding affinity of the Y24L and T20-4R peptides for the Q23I miniprotein is almost the same (Fig. 2E), as expected because this miniprotein does not harbor the FPPR motif for MPER binding. However, the T20-4R binding enthalpy of is slightly lower than that of Y24L for this miniprotein. This difference might be related to the preexisting α-helical structure in the free T20-4R peptide. As a result, the binding entropy loss is also lower, resulting in a very similar binding Gibbs energy.

In the case of the two FPPR-extended miniproteins, the binding affinities for both peptides at pH 3.0 are significantly increased compared to the Q23I variant (Fig. 2E), which agrees with the DSC results. The affinity increment is higher in the case of T20-4R compared to Y24L for both extended miniproteins, due to additional interactions at the FPPR-MPER interface. Moreover, the binding enthalpies for both peptides are higher than that observed for Q23I (Fig. 2F). This might be related to a cooperative communication along the NHR groove, as previously described [48,49]. These results collectively indicate that the FPPR extensions establish interactions with the MPER residues, enhancing the miniproteins' binding to their gp41 target.

3.2. Crystal structure of Q23I-ex2

The three miniproteins and their complexes with Y24L and T20-4R peptides were submitted to crystallization screens. Only the free Q23I-ex2 produced crystals of sufficient quality for X-ray diffraction. The crystal structure of Q23I-ex2 was solved by molecular replacement using the experimental model of the complex between covNHR and C34 (PDB entry 6R2G [20]). The final structure shows some regions with high B-factors, especially in the FPPR-extended region, indicating high flexibility. Only residues 3–128 were modelled (Fig. 3A). Ensemble refinement (ER) was performed with the final model to account for poorly modelled regions (Fig. 3B). This refinement removes the modeller bias through a Bayesian ensemble of structures. Since proteins are flexible and dynamic molecules —a characteristic partially hidden in the B-factors— ER is a valuable tool to reveal this flexibility [31]. The resulting ensemble shows lower R factors (R/Rfree = 0.18/0.22 *vs* R/Rfree = 0.20/0.24 for the single model). The greatest conformational flexibility is observed in the FPPR extension, particularly in the N-terminal part of the first helix and the loop connecting the second and third helices. This is likely due to poor interhelical contacts in this region, despite efforts to stabilize it by engineering interhelical interactions to reduce conformational flexibility and entropy. Moreover, two disulfide bridges (Cys3-Cys86 and Cys45-Cys128) were designed to bring together the three helices. The disulfide bridge in the carboxyl-terminal region reduces flexibility, but the bridge between Cys3-Cys86 in the amino-terminal region does not. Residues surrounding this disulfide bridge exhibit poor electron density, making them difficult to model. Moreover, a comparison of the experimental model with that obtained with AlphaFold 2 (Fig. 3A) shows evident discrepancies in the amino terminal part of the trimeric helical bundle structure. Indeed, the per-residue pLDDT score from the AlphaFold model indicates reduced prediction reliability in regions with higher RMSD in the ensemble obtained by ER.

In contrast to the FPPR-extended region, the core NHR region of the miniprotein shows lower B-factors and flexibility. Replacing the three buried glutamine residues with isoleucine (Ile35, Ile53 and Ile120) results in tighter packing of the helices, enhancing dramatically the thermostability of these miniproteins. Indeed, Ile35 and Ile53 are fully buried (ASA 1.2 and 3.4 Å^2), and Ile120 (19.1 Å^2) is mostly buried (Fig. 3C).

These results highlight a considerable difficulty in designing a structurally stable FPPR motif to interact with the gp41 MPER region. Despite this, the two extended miniproteins show a clearly increased affinity for the T20-4R peptide compared to Q23I, suggesting that the flexible FPPR extension adapts to interact with the MPER region of the peptide.

3.3. HIV inhibition assays

To evaluate whether the increases in binding affinity for the CHR-MPER peptide sequence observed in the extended miniproteins result in enhanced inhibitory activity against HIV-1 infection in cells, we carried out *in vitro* inhibition assays with different viral strains. First, single-cycle infection assays on TZM-Bl cells were performed using two pseudoviruses (SF162 and MW965.26) and one primary isolate (92RW009) in the presence of the three miniproteins (Fig. 4), as well as the parent miniprotein covNHR-N-dSS [16]. As a reference, we also tested the potent bNAb 3BNC117 [37]. All miniproteins showed considerable inhibitory activity against the three strains, with IC_{50} values in the nanomolar range, similar to other fusion inhibitors. The inhibitory activity of the miniproteins was further tested with four additional Tier 2 viruses (Fig. S12 and Table S4), demonstrating considerable inhibition breadth.

The three Q23I stabilized variants showed significantly higher activity than the less stable covNHR-N-dSS ($p < 0.01$ for Q23I; $p < 0.05$ for Q23I-ex1 and Q23I-ex2) (Fig. 4 and Table 2). This is consistent with a previously observed correlation between fusion inhibition activity and structural stability for these miniproteins [16]. However, we did not observe significant differences in IC_{50} between the Q23I variant and the two extended miniproteins in these assays (Table 2), despite the above-described differences in affinity for the gp41 CHR-MPER target sequence. These results suggest that, under the context of the virus-cell interface, the MPER region might be partially occluded, possibly embedded in part into the lipid membrane. In comparison to the 3BNC117 mAb, which targets the gp120 CD4 binding site, the covNHR-N miniproteins exhibit IC_{50} values >2 orders of magnitude higher in nM units (over one order of magnitude in μg/mL units).

Then, we assayed the inhibitory capacity of the miniproteins in PBMC cells using real virus isolates (Fig. 5 and Table 3). Notably, in these assays the miniproteins showed an inhibitory activity comparable to the potent 3BNC117 mAb for the two viruses tested. In the case of the difficult-to-neutralize 92RW009 virus, the miniproteins have a two-fold lower IC_{50} than 3BNC117 (Table 3). These inhibition activities were

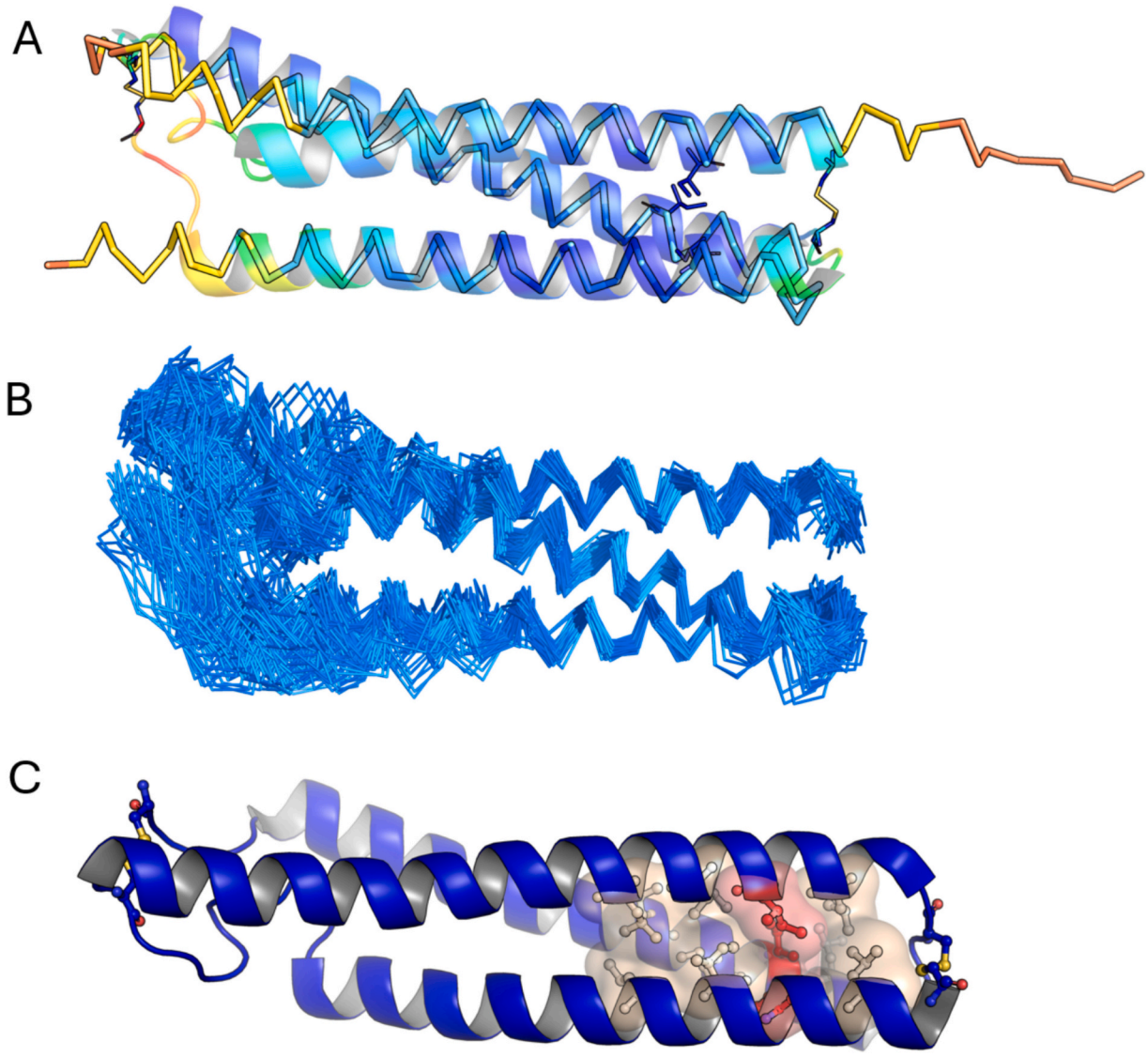

Fig. 3. Crystal structure of Q23I-ex2. (A) Superposition between the crystal structure (PDB entry 9HS7) with the AlphaFold model of Q23I-ex2: The experimental crystal structure model (residues 3–129) is represented with ribbons colored by the B-factor values, whereas the AlphaFold model backbone (residues 1–140) is drawn with sticks and colored by plDDT score (predicted Local Distance Difference Test). The isoleucine residues (Ile35, Ile53 and Ile120) and the disulfide bridges (Cys3-Cys86 and Cys45-Cys128) are shown in sticks. (B) Ensemble refinement of the coordinates of the best crystallographic model (9HS7), where the backbones of 100 molecular dynamics models have been represented with lines. (C) Packing of the mutated isoleucine residues (Ile35, Ile53 and Ile120, in red sticks) and surrounding hydrophobic residues (in grey sticks) represented by their Gaussian surface. Molecular graphics figures are drawn using PyMOL (The PyMOL Molecular Graphics System, Schrödinger, LLC).

observed in the absence of any toxic effect of miniproteins (Fig. S13). It is well established that the observed neutralizing potency of the bNAb decreases in PBMC assay compared to TZM-Bl [50–52]. Such a decrease in neutralization potency was not observed for our miniproteins. On the contrary, the IC_{50} values for the Tier 2 92RW009 virus in PBMC cells were even 100-fold lower than those measured in TZM-Bl cells, indicating that under the more *in vivo*-like conditions of the PBMC assay, the miniproteins are particularly efficient in blocking infection by primary viruses. This high efficacy may be explained by an efficient binding of the miniproteins to the few Envs present at the surface of primary isolates. Indeed, primary viruses have been described as having fewer Envs with a more constrained trimeric conformation compared to virus-adapted strains [53]. The small size of the miniproteins may still allow them to access the few Envs in closed conformation compared to virus adapted strains. Besides, the enhanced inhibitory effectiveness of the miniproteins could be attributed to particularly efficient inhibition of primary cell-to-cell transfer. Thus, for primary viruses with closed trimeric Envs and under the tight space of the virological synapse during cell-to-cell transfer, bNAbs are often less effective in blocking cell-to-cell transmission [54,55], whereas our small miniproteins may be able to access gp41 more easily to block membrane fusion in a primary virus environment.

3.4. Binding to Env spike

To investigate binding of the covNHR-N miniproteins to their target in a context more akin to the native viral Env, we performed ELISA experiments with soluble uncleaved gp160 MN/LAI Env (Fig. S14). The three miniproteins showed a high binding level to the Env spike, similarly to that previously observed for the parent covNHR-N miniproteins and for full covNHR [14,16]. This confirms that the CHR region of the native Env spike is accessible to the miniproteins. No significant differences were found between the binding levels of the three miniproteins, in agreement with their similar inhibitory activity.

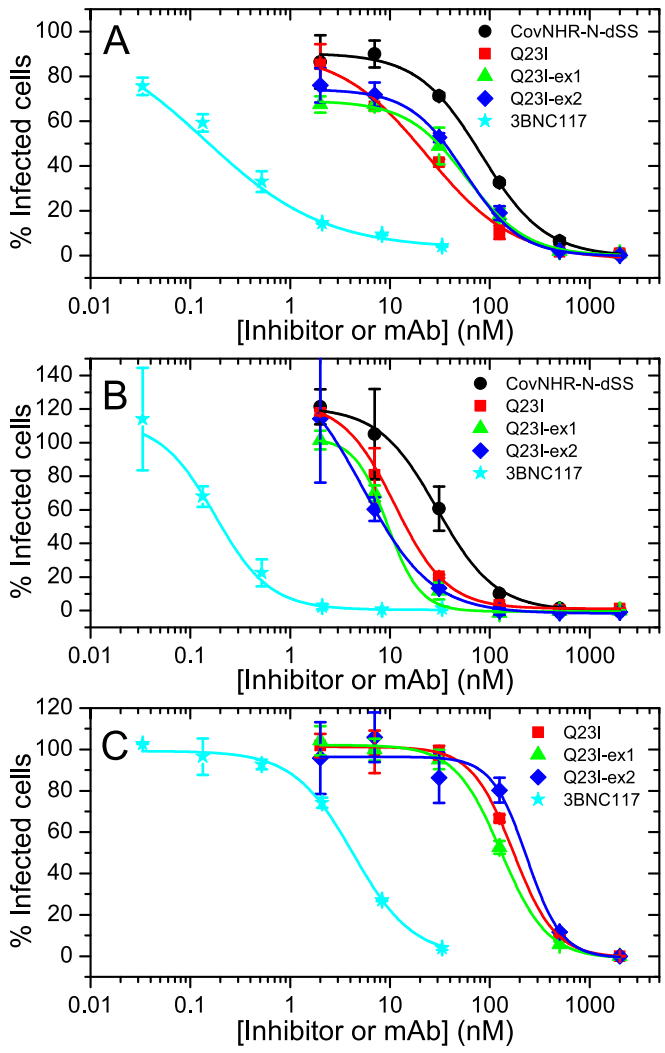

Fig. 4. TZM-Bl cell infection assays in presence of the inhibitory covNHR-N miniproteins or the 3BNC117 mAb. TZM-Bl cells were infected with different HIV strains in presence of variable concentrations of covNHR-N miniproteins or the 3BNC117 mAb. Two pseudoviruses, SF162 (A) and MW965.26 (B), and a primary isolate, 92RW009 (C), were used. Data correspond to the percentage of infected cells relative to the controls in absence of inhibitor. The lines represent the best fit using a Hill's sigmoidal function. Error bars correspond to the standard deviation from the mean values from duplicates.

3.5. Capture of virus particles

To further understand the mechanism by which these miniprotein inhibitors could block HIV-1 infection, we tested whether they could directly capture the primary infectious virus particles (SF162 and 92RW009). The amount of intact captured virus was quantified by p24 ELISA. As a positive control, we used mAb 447-52D directed to V3 loop and sera containing polyclonal neutralizing Abs. We also added 2F5 bNAb, which previously showed a limited binding capacity to whole virus particles [33].

The three miniproteins were unable to capture the two viruses tested (SF162 and 92RW009) (Fig. S15), although efficient inhibition of HIV replication was observed on primary cells. 2F5 was also unable to capture these viruses, whereas Abs against V3 loop and polyclonal samples bound SF162 viral particles efficiently. This lack of viral capture, even though they were inhibiting these viruses, suggests that structural modifications occurring during the fusion may be necessary for accessibility to these epitopes. These structural changes were described as crucial for 2F5 Ab binding to primary viruses [34]. It is also possible that

Table 2
Inhibitory activity of covNHR-N miniproteins and the 3BNC117 mAb in TZM-Bl assay for two pseudoviruses and one primary isolate.

Inhibitor	IC_{50}[a] (nM)	m[a]	IC_{50} (nM)	m	IC_{50} (nM)	m
	SF162		MW965.26		92RW009	
covNHR-N-dSS	82 ± 4[b]	1.36 ± 0.07	29.7 ± 2.5	1.49 ± 0.17		
Q23I	24 ± 7**	1.0 ± 0.3	11.2 ± 1.0*	1.67 ± 0.11	172.3 ± 1.4	2.06 ± 0.02
Q23I-ex1	59 ± 5*	1.45 ± 0.14	9.4 ± 2.6*	2.7 ± 1.8	130 ± 7	1.88 ± 0.22
Q23I-ex2	56 ± 6*	1.56 ± 0.09	5.4 ± 0.4**	1.26 ± 0.08	235 ± 69	2.5 ± 1.0
3BNC117	0.14 ± 0.05	0.73 ± 0.13	0.18 ± 0.08	1.6 ± 0.3	4.26 ± 0.13	1.45 ± 0.13

[a] The 50 % inhibitory concentrations (IC_{50}) and the Hill's coefficients (m) have been obtained by fitting the data of Fig. 4 using a Hill's sigmoidal function.
[b] Standard errors of the fits. Statistical significance *versus* covNHR-N-dSS: ** $p < 0.01$; * $p < 0.05$.

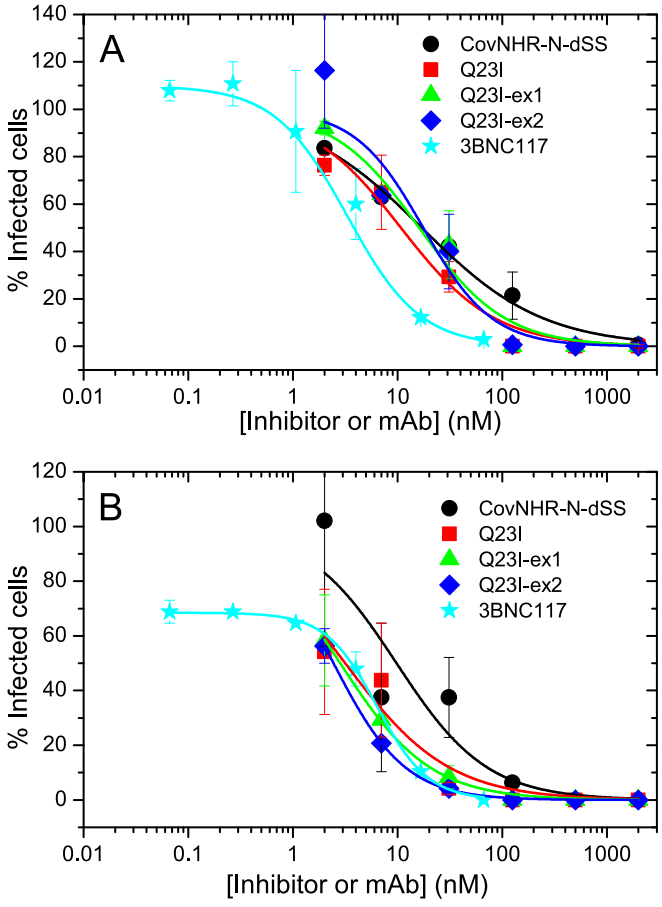

Fig. 5. PBMC infection assays in the presence of the inhibitory covNHR-N miniprotein or the 3BNC117 mAb. PBMCs were infected with virus isolates in the presence of variable concentrations of covNHR-N miniproteins or the 3BNC117 mAb. Viruses used were SF162 (A) and 92RW009 (B). Data correspond to the percentage of infected cells relative to the controls in the absence of an inhibitor. The lines represent the best fits using a Hill's sigmoidal function. Error bars correspond to the standard deviation from the mean values out of duplicates.

immobilized miniproteins and 2F5 at the plate surface are sterically unable to access the base of the virions' Envs where their epitopes are located. In contrast, the more exposed gp120 epitopes are more easily

Table 3
Inhibitory activity of covNHR-N miniproteins and the 3BNC117 mAb in PBMC assay for two different primary isolates.

Inhibitor	IC_{50} [a] (nM)	m [a]	IC_{50} (nM)	m
	SF162NN		92RW009	
covNHR-N-dSS	17 ± 3 [b]	0.75 ± 0.08	10 ± 4	1.0 ± 0.4
Q23I	11 ± 2	0.98 ± 0.16	3.1 ± 0.8	0.88 ± 0.23
Q23I-ex1	16 ± 4	1.06 ± 0.21	2.8 ± 0.1	1.01 ± 0.04
Q23I-ex2	17 ± 6	1.3 ± 0.5	2.44 ± 0.03	1.27 ± 0.02
3BNC117 mAb	3.3 ± 0.7	1.26 ± 0.13	6.36 ± 0.23	1.78 ± 0.09

[a] The 50 % inhibitory concentrations (IC_{50}) and the Hill's coefficients (m) have been obtained by fitting the data of Fig. 5 using a Hill's sigmoidal function.
[b] Standard errors of the fits.

accessible to the mAbs in this capture assay. Additional experiments, such as kinetics and avidity of attachment, will be necessary to decipher the mechanism leading to efficient inhibition on primary cells by the miniproteins.

3.6. Combination assays with broadly neutralizing mAbs

To further evaluate the significance of the inhibitory activity of these miniproteins and their relevance as potential antivirals in combination therapy, we tested the possible synergy of each miniprotein with bNAbs. First, combination experiments with each miniprotein and the bNAb 3BNC117 were conducted on TZM-Bl assays using SF162 pseudoviruses. Data were analyzed according to the Chou and Talalay method [38] to calculate the combination index (CI) and dose-reduction index (DRI) (Fig. 6; see Appendix S2, Table S5A, and Figs. S16–S18 in the Supplementary Material for additional details). We observed considerable synergistic effects between the miniproteins and 3BNC117, which inhibits virus attachment to the cells by targeting the CD4 receptor binding site on gp120. Synergy with a CI < 1 was observed at all dose levels corresponding to high inhibition percentages, whereas antagonism was only observed at two doses with low inhibition percentages. Synergy was more pronounced for Q23-ex1 and, especially, for Q23I-ex2 compared to the Q23I variant. Q23I-ex2, which contains the largest FPPR extension and interacts with part of the MPER (see above). Interestingly, the cooperativity parameter m (slopes in Hill's plots) in the miniprotein-mAb mixtures increased compared to the mAb alone or the miniproteins alone (Fig. S16). A cooperativity parameter m > 1 has been related to multiple interaction sites, whereas m < 1 has been attributed to target heterogeneity [56]. This enhancement resulted in significant dose reductions of 3BNC117 when combined with each miniprotein and more favorable instantaneous inhibitory potential (IIP) at therapeutically relevant doses (inhibition percentage > 90 %) [56]. These results suggest a mechanistic relationship between the inhibition of CD4 attachment to the cells by 3BNC117 and gp41-mediated fusion inhibition targeting the CHR-MPER.

We carried out similar combination experiments between the miniproteins and the bNAbs 2F5 and 4E10 (Fig. 6, Table S5B and Figs. S19–S22). These mAbs inhibit membrane fusion by targeting gp41 MPER epitopes that partially overlap (2F5) or are immediately downstream (4E10) to the interaction target of our miniproteins. Similar to the results obtained with 3BNC117, we observed strong synergy at high inhibition percentages and some antagonism at low doses (Fig. 6). The cooperativity parameters of the mixtures were also higher than those of the bNAbs alone and similar or higher than those of the miniproteins alone, giving rise to considerable dose reductions and IIP improvements. Since these mAbs and our miniproteins share a common inhibition mechanism, *i.e.*, blocking the membrane fusion, the observed synergy at high doses might be a result of a mutual enhancement in epitope exposure produced between the bNAbs (MPER) and the miniproteins (CHR-MPER). Another possible explanation for the synergy may be related to the need to block a minimum number of Envs to impair pore formation. Interestingly, the synergic effects with 2F5 seem to be more pronounced for Q23I-ex2, which harbors the longest FPPR extension to interact with part of the MPER. In contrast, the synergy with 4E10, which has a non-overlapping epitope, is quite similar across the three miniproteins.

Finally, we also tested the synergy between 3BNC117 and Q23I-ex1 using PBMC assays with two different primary isolates (SF162 and 92RW009 strains) (Fig. 6, Table S5C and Figs. S23–S25). In PBMC assays, synergy was even stronger at high inhibition percentages (CI < 0.3), while antagonism was observed at low percentages for the 92RW009 virus. A marked increase in the cooperativity m parameter was also observed for both viruses, compared to the m values found for the isolated proteins or mAb. In this type of assay, synergy could reflect an increased accessibility of masked epitopes, following simultaneous targeting of the CD4 binding site and the CHR-MPER region.

Assay (virus): TZM-Bl (SF162)

	%inhibition	CI	Miniprotein Alone (nM)	Miniprotein Mix (nM)	Miniprotein DRI	mAb Alone (nM)	mAb Mix (nM)	mAb DRI
					+ 3BNC117 (107:1)			
Q23I	50%	1.04	23	11	2.1	0.18	0.1	1.8
	70%	0.68	49	19	2.6	0.62	0.18	3.5
	90%	0.38	163	45	3.6	4.4	0.42	10
	95%	0.29	315	73	4.3	13	0.69	19
Q23I-ex1	50%	0.9	47	19	2.4	0.37	0.18	2.1
	70%	0.61	88	30	3	1	0.28	3.6
	90%	0.35	242	58	4.2	4.9	0.54	9
	95%	0.27	422	84	5	12	0.79	15
Q23I-ex2	50%	0.54	51	12.5	4.1	0.4	0.12	3.4
	70%	0.42	98	21	4.6	0.95	0.2	4.8
	90%	0.29	276	48	5.8	3.8	0.45	8.4
	95%	0.24	489	75	6.5	8.1	0.7	11.5
					+ 2F5 (3:1)			
Q23I	50%	1.16	43	12	3.7	4.4	3.9	1.1
	70%	0.91	74	20	3.7	10.6	6.7	1.6
	90%	0.64	175	48	3.6	44	16	2.7
	95%	0.55	282	78	3.6	95	26	3.7
Q23I-ex1	50%	0.94	31	6.4	4.8	2.9	2.1	1.4
	70%	0.68	76	14	5.4	9.5	4.7	2
	90%	0.41	319	49	6.6	62	16	3.8
	95%	0.32	707	97	7.3	176	32	5.5
Q23I-ex2	50%	0.54	37	6.7	5.3	6.5	2.3	2.8
	70%	0.47	71	13.5	5.3	16.4	4.5	3.6
	90%	0.38	202	39	5.1	71	13.1	5.4
	95%	0.35	360	71	5.1	159	24	6.7
					+ 4E10 (3:1)			
Q23I	50%	0.77	38	12.3	3.1	9.1	4.1	2.2
	70%	0.53	70	22	3.2	33	7.3	4.5
	90%	0.36	185	53	3.5	246	18	14
	95%	0.32	316	88	3.6	755	29	26
Q23I-ex1	50%	0.85	43	13.2	3.3	8.1	4.4	1.8
	70%	0.63	84	25	3.4	25	8.2	3
	90%	0.44	236	67	3.5	147	22	6.5
	95%	0.37	420	116	3.6	395	39	10.1
Q23I-ex2	50%	0.83	40	14.6	2.7	10.6	4.9	2.2
	70%	0.57	78	24	3.2	30	8	3.8
	90%	0.34	226	52	4.3	160	17.5	9.2
	95%	0.27	407	81	5	405	27	15

Assay (virus): PBMC (SF162)

	%inhibition	CI	Miniprotein Alone (nM)	Miniprotein Mix (nM)	Miniprotein DRI	mAb Alone (nM)	mAb Mix (nM)	mAb DRI
					+ 3BNC117 (3:1)			
Q23I-ex1	50%	0.81	13.5	2.7	5.1	1.4	0.9	1.6
	70%	0.43	68	4	17	3.5	1.3	2.7
	90%	0.18	907	7.7	118	15	2.6	5.8
	95%	0.11	3792	11	342	33	3.7	9

Assay (virus): PBMC (92RW009)

					+ 3BNC117 (3:1)			
Q23I-ex1	50%	1.02	3	1.6	1.9	1	0.5	2
	70%	0.62	10	2.9	3.5	2.8	1	3
	90%	0.29	67	7.5	9	14	2.5	5.6
	95%	0.19	193	13	15	34	4.2	7.9

Fig. 6. Combination index (CI) and dose reductions index (DRI) for inhibition of HIV-1 cell infection with combinations of covNHR-N miniproteins and different bNAbs. Data have been calculated as described in detail in the Supplementary Appendix S2. The background colour intensity indicates higher synergic effects in red (CI) and green (DRI).

3.7. *Ex vivo* inhibition

Finally, we evaluated the capacity of one of our miniproteins to inhibit virus replication in cells of HIV-1 infected donors. We chose to focus on Q23I-ex2 for this analysis because it exhibited the most pronounced overall synergistic effect with bNAbs. *Ex vivo* inhibition assays are extremely relevant for inhibitory analysis, as the virus is directly reactivated from infected cells without a prior amplification step. We used CD4+ T cells isolated from 8 viremic participants, covering 5 different HIV-1 clades (Table S6). HIV-1 production was

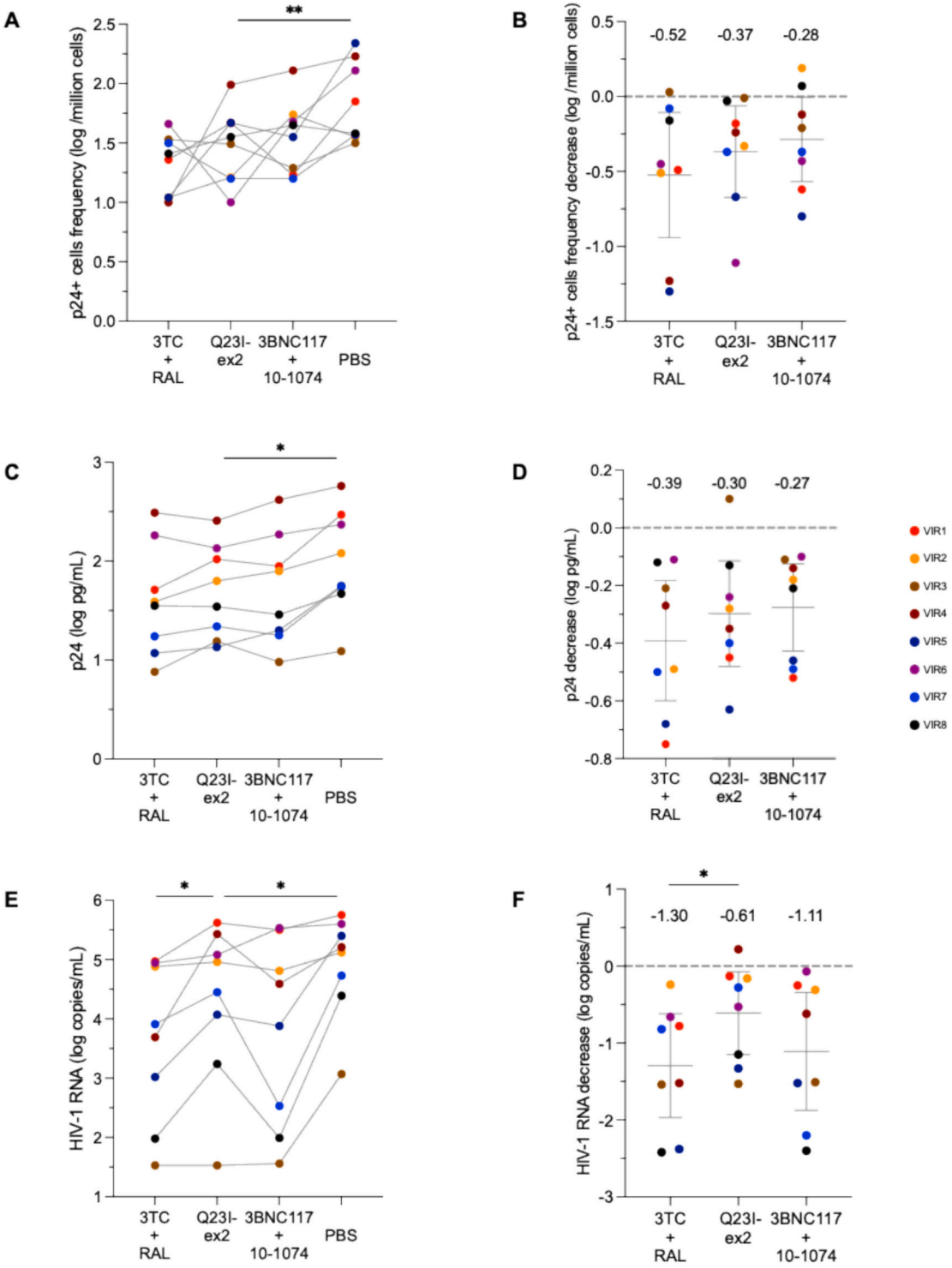

Fig. 7. *Ex vivo* inhibition assays in presence of Q23I-ex2 or the 3BNC117 + 10–1074 mAbs or antiretroviral drugs. Isolated CD4+ T cells from viremic HIV-infected individuals failing antiretroviral therapy were treated with either: (i) antiretroviral drugs (raltegravir [RAL] + lamivudine [3TC], 200 nM each), (ii) Q23I-ex2 (200 nM), (iii) bNAbs (clones 3BNC117 + 10-1074, 7 nM each) and (iv) control (PBS). The frequency of HIV-infected cells (p24+) (A-B), p24 in supernatants (C–D) and HIV-RNA in supernatants (E–F) were measured. Either the frequency of cells or levels are depicted (A, C, E) or the difference between the control and treated conditions (B, D, F) for each participant (VIR1 to 8). Each colored dot represents another viremic infected individual. Significant differences between the Q23I-ex2 condition and other conditions are highlighted (Wilcoxon; *$p < 0.05$, **$p < 0.01$, ***$p < 0.001$, ****$p < 0.0001$).

analyzed upon Q23I-ex2 treatment and compared to the combination of two bNAbs (3BNC117 + 10-1074), previously used in clinical trials [57] and two well-known antiretroviral drugs (RAL + 3TC). Cell viability was comparable across all conditions (Fig. S26), indicating that Q23I-ex2 was not toxic to the cells. Compared to the control condition, Q23I-ex2 effectively prevented new cell infections, as evidenced by the decrease in the frequency of p24+ cells (Fig. 7A). This decrease in the frequency of productively infected cells was in a similar range as for antiretroviral drugs and combined bNAbs (Fig. 7B). Similarly, p24 levels in supernatants decreased upon Q23I-ex2 treatment (Fig. 7C) to a similar extent as antiretroviral drugs and combined bNAbs conditions (Fig. 7D). Finally, Q23I-ex2 was also able to decrease HIV-RNA levels in the supernatants (Fig. 7E), similar to combined bNAbs but to a lesser extent than antiretroviral drugs (Fig. 7F). Altogether, although used alone, Q23I-ex2 effectively prevented HIV-1 infection of new target cells in *ex vivo* treated CD4+ T cells from viremic individuals with a similar magnitude as for combined antiretroviral drugs or combined bNAbs.

4. Discussion

Here, we have described a set of small artificial miniproteins aimed at blocking gp41-mediated membrane fusion and, by this means, inhibit HIV-1 infection. These miniproteins faithfully mimic the N-terminal half of the NHR region of gp41 and were engineered based on our previous designs with two objectives: first, to increase their conformational stability, since we previously found that this property was strongly correlated with HIV-1 inhibitory activity [14,16]. A similar correlation was also found for chimeric miniproteins mimicking HR1 in SARS-CoV-2 S2 [58,59]. Here, we indeed found about a 2.5-fold increase in the binding affinity of the Q23I stabilized miniprotein for its complementary CHR sequence compared to the non-mutated counterpart (Table 1). This translates to a 3-fold increase in inhibitory potency against HIV-1 cell infection (Table 2). A second objective was to extend the targeted interaction by prolonging the N-terminus of the miniproteins with FPPR sequence segments that could interact with part of the MPER, a highly pursued neutralizing epitope targeted by bNAbs [9]. We found that the inclusion of these FPPR extensions in the miniproteins enhanced the binding affinity for the gp41-derived peptides, despite the considerable flexibility of the FPPR region, as shown in the crystal structure of Q23I-ex2. Moreover, only the extended miniproteins showed enhanced binding to the T20-4R peptide compared to the Y24L peptide, devoid of MPER residue, suggesting a contribution of the FPPR-MPER interaction. However, this binding affinity enhancement did not produce significant increases in the inhibitory potency of the miniproteins for different strains. It is possible that, under the complex environment of viral infection assays, factors other than direct binding to the target sequence may play an important role in inhibition. For instance, the MPER region might be less accessible to the miniproteins due to its embedment into the viral membrane [60].

There is increasing evidence that HIV-1 can infect cells not only at the plasma membrane but also *via* endocytosis and fusion with endosomes [61–63]. Accordingly, effective fusion inhibitors may need to prebind the Env and/or co-localize with the virus before it becomes endocytosed. Additionally, an inhibitor also needs to resist the acidic pH and harsh proteolytic activity in the late endosome. In this scenario, high conformational stability may play an important role in inhibiting endosome-mediated viral infection and might explain why more stable mimetic proteins show higher inhibitory activity than less stable ones. We have recently shown that conformational stability also plays a major role in SARS-CoV-2 inhibition potency of HR1-mimetic proteins [58]. Recently, Wu et al. demonstrated that covalent stabilization of a trimeric 51-residue gp41 prehairpin intermediate increased epitope accessibility and immunogenicity [64]. These studies highlight the importance of conformational stabilization strategies to improve protein-based inhibitors and vaccine candidates.

Although our miniproteins were unable to capture virus particles in ELISA assays, they showed unexpectedly high and broad inhibitory activity on primary cell infection. Moreover, Q23I-ex2 was able to inhibit replication of different HIV-1 clades in CD4+ T cells purified from eight distinct contemporaneously infected individuals *ex vivo*. These broad anti-HIV-1 activities were comparable to combined ART or bNAbs, demonstrating the extensive potency of Q23I-ex2 even when used alone. We suggest that the small size and robust stability of the miniproteins may play an important role in these high inhibitory activities. Miniproteins may access to the highly masked CHR epitope on primary HIV, thereby supporting viral inhibition. Likewise, single-chain variable fragments (scFvs) of bNAbs are more effective in inhibiting cell-cell fusion than their IgG counterparts due to their smaller size, which allows them access to sterically constrained epitopes [65].

The observed synergy between 3BNC117 and the CHR targeting miniproteins indicates a mechanistic linkage between gp120 binding to CD4 and gp41-mediated fusion. However, it is very difficult to establish whether this cooperative connection is due to allosteric effects within the Env structure or is a result of more complex factors, including the need for multiple Env trimers to cooperate in the fusion process. At a molecular level, soluble CD4 (sCD4) and b12 binding to the gp120 binding site induce an open conformation of Env, with considerable conformational rearrangements in gp41, reorienting both NHR and CHR and repositioning the fusion peptide [66]. These conformational changes enhance the exposure of CHR and MPER, favoring the binding of inhibitors and bNAbs. However, in contrast to CD4 and b12, 3BNC117 binding stabilizes the closed Env conformation, not supporting a direct allosteric effect with fusion inhibitors. An alternative explanation may be related to multiple interaction sites. For instance, PRO542, a tetravalent CD4-immunoglobulin fusion protein that blocks virus attachment to the CD4 receptor, shows significant synergy with T20 in the inhibition of virus-cell and cell-cell fusion [67]. The authors suggested that blocking the virus attachment to CD4 may impair clustering of multiple Envs necessary for pore formation, rendering prefusion intermediates more susceptible to fusion inhibitors. We observed significant increases in the cooperative parameter with $m > 1$ in the combination assays, compared to single miniproteins or bNAbs, favoring multiple interactions. In addition, a recent study shows that combining Abs that recognize different epitopes may be beneficial to mitigate the effect of antibody escape [68].

In conclusion, the single-chain NHR mimetic miniproteins presented here are potent HIV-1 fusion inhibitors capable of efficiently reducing the replication of a broad range of HIV strains. Moreover, these molecules show significant synergic effects with bNAbs, demonstrating a strong potential to be developed as part of drug compositions to treat HIV-1 infection.

CRediT authorship contribution statement

Daniel Polo-Megías: Methodology, Investigation, Formal analysis, Data curation. **Mario Cano-Muñoz:** Methodology, Investigation, Formal analysis, Data curation. **Pierre Gantner:** Investigation. **Géraldine Laumond:** Investigation. **Thomas Decoville:** Investigation. **Jasmine Grezzani:** Investigation. **Ilaria La Rocchia:** Investigation. **M. Carmen Salinas-Garcia:** Methodology, Investigation. **Ana Cámara-Artigas:** Writing – review & editing, Visualization, Methodology, Investigation, Formal analysis, Data curation. **José A. Gavira:** Methodology, Investigation, Formal analysis, Data curation. **Francisco Conejero-Lara:** Writing – original draft, Validation, Supervision, Project administration, Methodology, Investigation, Funding acquisition, Formal analysis, Data curation, Conceptualization. **Christiane Moog:** Writing – review & editing, Validation, Supervision, Project administration, Methodology, Funding acquisition, Formal analysis, Data curation, Conceptualization.

Declaration of competing interest

The authors declare that they have no known competing financial interests or personal relationships that could have appeared to influence the work reported in this paper.

Acknowledgements

This work was supported by grant PID2019.107515RB.C21 from the Spanish State Research Agency (SRA/10.13039/501100011033). Work was further supported by ANRS (Agence Nationale de Recherches sur le SIDA et les hépatites virales), the Investissements d'Avenir program managed by the ANR under reference ANR-10-LABX-77 and EHVA (N°681032, Horizon 2020). P.G. is supported by a research grant from ANRS (N° ECTZ242220) and SIDACTION (N°13709).

The work is part of the Doctoral Thesis of Daniel Polo-Megías. Daniel Polo-Megías acknowledges a predoctoral fellowship from the Andalusian Regional Government. Mario Cano-Muñoz was supported by a Postdoctoral Research Program from the Spanish Research Agency: Juan de la Cierva (JDC2022-049681-I). We are grateful to the Spanish Radiation Synchrotron Source (ALBA), Barcelona, Spain, and the European Synchrotron Radiation Facility (ESRF), Grenoble, France, for the provision of beamtime and staff assistance at XALOC (ALBA, BAG number 2023087670) and ID30B and ID23-2 (ESRF, BAG number MX2650) beamlines during diffraction data collection.

Appendix A. Supplementary data

Supplementary data to this article can be found online at https://doi.org/10.1016/j.ijbiomac.2025.143157.

Data availability

Data will be made available on request.

References

[1] UNAIDS, UNAIDS data 2023, Https://Www.Unaids.Org/Sites/Default/Files/Media_asset/UNAIDS_FactSheet_en.Pdf (n.d.). https://www.unaids.org/en/resources/documents/2023/2023_unaids_data.

[2] B.F. Haynes, K. Wiehe, P. Borrow, K.O. Saunders, B. Korber, K. Wagh, A. J. McMichael, G. Kelsoe, B.H. Hahn, F. Alt, G.M. Shaw, Strategies for HIV-1 vaccines that induce broadly neutralizing antibodies, Nat. Rev. Immunol. 23 (2023) 142–158, https://doi.org/10.1038/s41577-022-00753-w.

[3] M.S. Saag, R.T. Gandhi, J.F. Hoy, R.J. Landovitz, M.A. Thompson, P.E. Sax, D. M. Smith, C.A. Benson, S.P. Buchbinder, C. del Rio, J.J. Eron, G. Fätkenheuer, H. F. Günthard, J.-M. Molina, D.M. Jacobsen, P.A. Volberding, Antiretroviral drugs for treatment and prevention of HIV infection in adults, JAMA 324 (2020) 1651, https://doi.org/10.1001/jama.2020.17025.

[4] A.B. Ward, I.A. Wilson, The HIV-1 envelope glycoprotein structure: nailing down a moving target, Immunol. Rev. 275 (2017) 21–32, https://doi.org/10.1111/imr.12507.

[5] D.R. Burton, L. Hangartner, Broadly neutralizing antibodies to HIV and their role in vaccine design, Annu. Rev. Immunol. 34 (2016) 635–659, https://doi.org/10.1146/annurev-immunol-041015-055515.

[6] B.F. Haynes, D.R. Burton, J.R. Mascola, Multiple roles for HIV broadly neutralizing antibodies, Sci. Transl. Med. 11 (2019) eaaz2686, https://doi.org/10.1126/scitranslmed.aaz2686.

[7] Y. Liu, W. Cao, M. Sun, T. Li, Broadly neutralizing antibodies for HIV-1: efficacies, challenges and opportunities, Emerg, Microbes Infect. 9 (2020) 194–206, https://doi.org/10.1080/22221751.2020.1713707.

[8] A. Rodari, G. Darcis, C.M. Van Lint, The current status of latency reversing agents for HIV-1 remission, Annu. Rev. Virol. 8 (2021) 491–514, https://doi.org/10.1146/annurev-virology-091919-103029.

[9] M.B. Zwick, R. Jensen, S. Church, M. Wang, G. Stiegler, R. Kunert, H. Katinger, D. R. Burton, Anti-human immunodeficiency virus type 1 (HIV-1) antibodies 2F5 and 4E10 require surprisingly few crucial residues in the membrane-proximal external region of glycoprotein gp41 to neutralize HIV-1, J. Virol. 79 (2005) 1252–1261, https://doi.org/10.1128/JVI.79.2.1252-1261.2005.

[10] J. Huang, G. Ofek, L. Laub, M.K. Louder, N.A. Doria-Rose, N.S. Longo, H. Imamichi, R.T. Bailer, B. Chakrabarti, S.K. Sharma, S.M. Alam, T. Wang, Y. Yang, B. Zhang, S. A. Migueles, R. Wyatt, B.F. Haynes, P.D. Kwong, J.R. Mascola, M. Connors, Broad and potent neutralization of HIV-1 by a gp41-specific human antibody, Nature 491 (2012) 406–412, https://doi.org/10.1038/nature11544.

[11] S.M. Alam, M. Morelli, S.M. Dennison, H.-X. Liao, R. Zhang, S.-M. Xia, S. Rits-Volloch, L. Sun, S.C. Harrison, B.F. Haynes, B. Chen, Role of HIV membrane in neutralization by two broadly neutralizing antibodies, Proc. Natl. Acad. Sci. U. S. A. 106 (2009) 20234–20239, https://doi.org/10.1073/pnas.0908713106.

[12] K. Rantalainen, Z.T. Berndsen, A. Antanasijevic, T. Schiffner, X. Zhang, W.H. Lee, J. L. Torres, L. Zhang, A. Irimia, J. Copps, K.H. Zhou, Y.D. Kwon, W.H. Law, C. A. Schramm, R. Verardi, S.J. Krebs, P.D. Kwong, N.A. Doria-Rose, I.A. Wilson, M. B. Zwick, J.R. Yates, W.R. Schief, A.B. Ward, HIV-1 envelope and MPER antibody structures in lipid assemblies, Cell Rep. 31 (2020) 107583, https://doi.org/10.1016/j.celrep.2020.107583.

[13] K. Tan, J. Chen, Y. Kaku, Y. Wang, L. Donius, R.A. Khan, X. Li, H. Richter, M. S. Seaman, T. Walz, W. Hwang, E.L. Reinherz, M. Kim, Inadequate structural constraint on fab approach rather than paratope elicitation limits HIV-1 MPER vaccine utility, Nat. Commun. 14 (2023), https://doi.org/10.1038/s41467-023-42097-6.

[14] S. Jurado, C. Moog, M. Cano-Muñoz, S. Schmidt, G. Laumond, V. Ruocco, S. Standoli, D. Polo-Megías, F. Conejero-Lara, B. Morel, Probing vulnerability of the gp41 C-terminal heptad repeat as target for Miniprotein HIV inhibitors, J. Mol. Biol. 432 (2020) 5577–5592, https://doi.org/10.1016/j.jmb.2020.08.010.

[15] D.C. Chan, D. Fass, J.M. Berger, P.S. Kim, Core structure of gp41 from the HIV envelope glycoprotein, Cell 89 (1997) 263–273, https://doi.org/10.1016/S0092-8674(00)80205-6.

[16] M. Cano-Muñoz, J. Lucas, L.-Y. Lin, S. Cesaro, C. Moog, F. Conejero-Lara, Conformational stabilization of Gp41-mimetic Miniproteins opens up new ways of inhibiting HIV-1 fusion, Int. J. Mol. Sci. 23 (2022) 2794, https://doi.org/10.3390/ijms23052794.

[17] J.M. Kilby, S. Hopkins, T.M. Venetta, B. DiMassimo, G.A. Cloud, J.Y. Lee, L. Alldredge, E. Hunter, D. Lambert, D. Bolognesi, T. Matthews, M.R. Johnson, M. A. Nowak, G.M. Shaw, M.S. Saag, Potent suppression of HIV-1 replication in humans by T-20, a peptide inhibitor of gp41-mediated virus entry, Nat. Med. 4 (1998) 1302–1307, https://doi.org/10.1038/3293.

[18] N. Guex, M.C. Peitsch, SWISS-MODEL and the Swiss-Pdb viewer: an environment for comparative protein modeling, Electrophoresis 18 (1997) 2714–2723, https://doi.org/10.1002/elps.1150181505.

[19] E. Krieger, G. Vriend, YASARA view-molecular graphics for all devices-from smartphones to workstations, Bioinformatics 30 (2014) 2981–2982, https://doi.org/10.1093/bioinformatics/btu426.

[20] S. Jurado, M. Cano-Muñoz, B. Morel, S. Standoli, E. Santarossa, C. Moog, S. Schmidt, G. Laumond, A. Cámara-Artigas, F. Conejero-Lara, Structural and thermodynamic analysis of HIV-1 fusion inhibition using small gp41 mimetic proteins, J. Mol. Biol. 431 (2019) 3091–3106, https://doi.org/10.1016/j.jmb.2019.06.022.

[21] M. Mirdita, K. Schütze, Y. Moriwaki, L. Heo, S. Ovchinnikov, M. Steinegger, ColabFold: making protein folding accessible to all, Nat. Methods 19 (2022) 679–682, https://doi.org/10.1038/s41592-022-01488-1.

[22] S. Crespillo, A. Cámara-Artigas, S. Casares, B. Morel, E.S. Cobos, P.L. Mateo, N. Mouz, C.E. Martin, M.G. Roger, R. El Habib, B. Su, C. Moog, F. Conejero-Lara, Single-chain protein mimetics of the N-terminal heptad-repeat region of gp41 with potential as anti–HIV-1 drugs, Proc. Natl. Acad. Sci. U. S. A. 111 (2014) 18207–18212, https://doi.org/10.1073/pnas.1413592112.

[23] E. Gasteiger, C. Hoogland, A. Gattiker, S. Duvaud, M.R. Wilkins, R.D. Appel, A. Bairoch, Protein Identification and Analysis Tools on the ExPASy Server, in: The Proteomics Protocols Handbook, Humana Press, Totowa, NJ, 2005, pp. 571–607, https://doi.org/10.1385/1-59259-890-0:571.

[24] J. Juanhuix, F. Gil-Ortiz, G. Cuní, C. Colldelram, J. Nicolás, J. Lidón, E. Boter, C. Ruget, S. Ferrer, J. Benach, Developments in optics and performance at BL13-XALOC, the macromolecular crystallography beamline at the Alba synchrotron, J. Synchrotron Radiat. 21 (2014) 679–689, https://doi.org/10.1107/S160057751400825X.

[25] W. Kabsch, XDS, Acta Crystallogr. D Biol. Crystallogr. 66 (2010) 125–132, https://doi.org/10.1107/S0907444909047337.

[26] M.D. Winn, C.C. Ballard, K.D. Cowtan, E.J. Dodson, P. Emsley, P.R. Evans, R. M. Keegan, E.B. Krissinel, A.G.W. Leslie, A. McCoy, S.J. McNicholas, G. N. Murshudov, N.S. Pannu, E.A. Potterton, H.R. Powell, R.J. Read, A. Vagin, K. S. Wilson, Overview of the *CCP* 4 suite and current developments, Acta Crystallogr. D Biol. Crystallogr. 67 (2011) 235–242, https://doi.org/10.1107/S0907444910045749.

[27] P.D. Adams, P.V. Afonine, G. Bunkóczi, V.B. Chen, I.W. Davis, N. Echols, J. J. Headd, L.-W. Hung, G.J. Kapral, R.W. Grosse-Kunstleve, A.J. McCoy, N. W. Moriarty, R. Oeffner, R.J. Read, D.C. Richardson, J.S. Richardson, T. C. Terwilliger, P.H. Zwart, *PHENIX* : a comprehensive Python-based system for macromolecular structure solution, Acta Crystallogr. D Biol. Crystallogr. 66 (2010) 213–221, https://doi.org/10.1107/S0907444909052925.

[28] A.J. McCoy, R.W. Grosse-Kunstleve, P.D. Adams, M.D. Winn, L.C. Storoni, R. J. Read, *Phaser* crystallographic software, J. Appl. Cryst. 40 (2007) 658–674, https://doi.org/10.1107/S0021889807021206.

[29] P. Emsley, B. Lohkamp, W.G. Scott, K. Cowtan, Features and development of *Coot*, Acta Crystallogr. D Biol. Crystallogr. 66 (2010) 486–501, https://doi.org/10.1107/S0907444910007493.

[30] P.V. Afonine, R.W. Grosse-Kunstleve, N. Echols, J.J. Headd, N.W. Moriarty, M. Mustyakimov, T.C. Terwilliger, A. Urzhumtsev, P.H. Zwart, P.D. Adams, Towards automated crystallographic structure refinement with *phenix.Refine*, Acta Crystallogr. D Biol. Crystallogr. 68 (2012) 352–367, https://doi.org/10.1107/S0907444912001308.

[31] N. Ploscariu, T. Burnley, P. Gros, N.M. Pearce, Improving sampling of crystallographic disorder in ensemble refinement, Acta Crystallogr. D Struct. Biol. 77 (2021) 1357–1364, https://doi.org/10.1107/S2059798321010044.
[32] C.J. Williams, J.J. Headd, N.W. Moriarty, M.G. Prisant, L.L. Videau, L.N. Deis, V. Verma, D.A. Keedy, B.J. Hintze, V.B. Chen, S. Jain, S.M. Lewis, W.B. Arendall, J. Snoeyink, P.D. Adams, S.C. Lovell, J.S. Richardson, D.C. Richardson, MolProbity: more and better reference data for improved all-atom structure validation, Protein Sci. 27 (2018) 293–315, https://doi.org/10.1002/pro.3330.
[33] C. Moog, N. Dereuddre-Bosquet, J.-L. Teillaud, M.E. Biedma, V. Holl, G. Van Ham, L. Heyndrickx, A. Van Dorsselaer, D. Katinger, B. Vcelar, S. Zolla-Pazner, I. Mangeot, C. Kelly, R.J. Shattock, R. Le Grand, Protective effect of vaginal application of neutralizing and nonneutralizing inhibitory antibodies against vaginal SHIV challenge in macaques, Mucosal Immunol. 7 (2014) 46–56, https://doi.org/10.1038/mi.2013.23.
[34] B.K. Chakrabarti, L.M. Walker, J.F. Guenaga, A. Ghobbeh, P. Poignard, D. R. Burton, R.T. Wyatt, Direct antibody access to the HIV-1 membrane-proximal external region positively correlates with neutralization sensitivity, J. Virol. 85 (2011) 8217–8226, https://doi.org/10.1128/JVI.00756-11.
[35] L. Heyndrickx, A. Heath, E. Sheik-Khalil, J. Alcami, V. Bongertz, M. Jansson, M. Malnati, D. Montefiori, C. Moog, L. Morris, S. Osmanov, V. Polonis, M. Ramaswamy, Q. Sattentau, M. Tolazzi, H. Schuitemaker, B. Willems, T. Wrin, E. M. Fenyö, G. Scarlatti, International network for comparison of HIV neutralization assays: the NeutNet report II, PLoS One 7 (2012) e36438, https://doi.org/10.1371/journal.pone.0036438.
[36] M. Sarzotti-Kelsoe, R.T. Bailer, E. Turk, C. Lin, M. Bilska, K.M. Greene, H. Gao, C. A. Todd, D.A. Ozaki, M.S. Seaman, J.R. Mascola, D.C. Montefiori, Optimization and validation of the TZM-bl assay for standardized assessments of neutralizing antibodies against HIV-1, J. Immunol. Methods 409 (2014) 131–146, https://doi.org/10.1016/j.jim.2013.11.022.
[37] J.F. Scheid, H. Mouquet, B. Ueberheide, R. Diskin, F. Klein, T.Y.K. Oliveira, J. Pietzsch, D. Fenyo, A. Abadir, K. Velinzon, A. Hurley, S. Myung, F. Boulad, P. Poignard, D.R. Burton, F. Pereyra, D.D. Ho, B.D. Walker, M.S. Seaman, P. J. Bjorkman, B.T. Chait, M.C. Nussenzweig, Sequence and structural convergence of broad and potent HIV antibodies that mimic CD4 binding, Science 333 (2011) (1979) 1633–1637, https://doi.org/10.1126/science.1207227.
[38] T.-C. Chou, P. Talalay, Quantitative analysis of dose-effect relationships: the combined effects of multiple drugs or enzyme inhibitors, Adv. Enzyme Regul. 22 (1984) 27–55, https://doi.org/10.1016/0065-2571(84)90007-4.
[39] M. Pardons, A.E. Baxter, M. Massanella, A. Pagliuzza, R. Fromentin, C. Dufour, L. Leyre, J.-P. Routy, D.E. Kaufmann, N. Chomont, Single-cell characterization and quantification of translation-competent viral reservoirs in treated and untreated HIV infection, PLoS Pathog. 15 (2019) e1007619, https://doi.org/10.1371/journal.ppat.1007619.
[40] H. Ji, C. Bracken, M. Lu, Buried polar interactions and conformational stability in the simian immunodeficiency virus (SIV) gp41 Core, Biochemistry 39 (2000) 676–685, https://doi.org/10.1021/bi991893e.
[41] M. Cano-Muñoz, S. Cesaro, B. Morel, J. Lucas, C. Moog, F. Conejero-Lara, Extremely Thermostabilizing Core mutations in coiled-coil mimetic proteins of HIV-1 gp41 produce diverse effects on target binding but do not affect their inhibitory activity, Biomolecules 11 (2021) 566, https://doi.org/10.3390/biom11040566.
[42] V. Buzon, G. Natrajan, D. Schibli, F. Campelo, M.M. Kozlov, W. Weissenhorn, Crystal structure of HIV-1 gp41 including both fusion peptide and membrane proximal external regions, PLoS Pathog. 6 (2010) e1000880, https://doi.org/10.1371/journal.ppat.1000880.
[43] D.B. Volkin, A.M. Klibanov, Thermal destruction processes in proteins involving cystine residues, J. Biol. Chem. 262 (1987) 2945–2950, https://doi.org/10.1016/S0021-9258(18)61451-6.
[44] T. Muster, F. Steindl, M. Purtscher, A. Trkola, A. Klima, G. Himmler, F. Rüker, H. Katinger, A conserved neutralizing epitope on gp41 of human immunodeficiency virus type 1, J. Virol. 67 (1993) 6642–6647, https://doi.org/10.1128/jvi.67.11.6642-6647.1993.
[45] S. Crespillo, S. Casares, P.L. Mateo, F. Conejero-Lara, Thermodynamic analysis of the binding of 2F5 (fab and immunoglobulin G forms) to its gp41 epitope reveals a strong influence of the immunoglobulin fc region on affinity, J. Biol. Chem. 289 (2014) 594–599, https://doi.org/10.1074/jbc.C113.524439.
[46] P. Luo, R.L. Baldwin, Mechanism of Helix induction by Trifluoroethanol: a framework for extrapolating the Helix-forming properties of peptides from Trifluoroethanol/water mixtures Back to water, Biochemistry 36 (1997) 8413–8421, https://doi.org/10.1021/bi9707133.
[47] S. Serrano, A. Araujo, B. Apellániz, S. Bryson, P. Carravilla, I. de la Arada, N. Huarte, E. Rujas, E.F. Pai, J.L.R. Arrondo, C. Domene, M.A. Jiménez, J.L. Nieva, Structure and immunogenicity of a peptide vaccine, including the complete HIV-1 gp41 2F5 epitope, J. Biol. Chem. 289 (2014) 6565–6580, https://doi.org/10.1074/jbc.M113.527747.
[48] M. Cano-Muñoz, S. Jurado, B. Morel, F. Conejero-Lara, Conformational flexibility of the conserved hydrophobic pocket of HIV-1 gp41, Implications for the discovery of small-molecule fusion inhibitors, Int J Biol Macromol 192 (2021) 90–99, https://doi.org/10.1016/j.ijbiomac.2021.09.198.
[49] S. Jurado, M. Cano-Muñoz, D. Polo-Megías, F. Conejero-Lara, B. Morel, Thermodynamic dissection of the interface between HIV-1 gp41 heptad repeats reveals cooperative interactions and allosteric effects, Arch. Biochem. Biophys. 688 (2020) 108401, https://doi.org/10.1016/j.abb.2020.108401.
[50] C. Moog, C. Spenlehauer, H. Fleury, F. Heshmati, S. Saragosti, F. Letourneur, A. Kirn, A.M. Aubertin, Neutralization of primary human immunodeficiency virus type 1 isolates: a study of parameters implicated in neutralization *in vitro*, AIDS Res. Hum. Retroviruses 13 (1997) 19–27, https://doi.org/10.1089/aid.1997.13.19.
[51] M.K. Louder, A. Sambor, E. Chertova, T. Hunte, S. Barrett, F. Ojong, E. Sanders-Buell, S. Zolla-Pazner, F.E. McCutchan, J.D. Roser, D. Gabuzda, J.D. Lifson, J. R. Mascola, HIV-1 envelope pseudotyped viral vectors and infectious molecular clones expressing the same envelope glycoprotein have a similar neutralization phenotype, but culture in peripheral blood mononuclear cells is associated with decreased neutralization sensitivity, Virology 339 (2005) 226–238, https://doi.org/10.1016/j.virol.2005.06.003.
[52] Y.Z. Cohen, J.C.C. Lorenzi, M.S. Seaman, L. Nogueira, T. Schoofs, L. Krassnig, A. Butler, K. Millard, T. Fitzsimons, X. Daniell, J.P. Dizon, I. Shimeliovich, D. C. Montefiori, M. Caskey, M.C. Nussenzweig, Neutralizing activity of broadly neutralizing anti-HIV-1 antibodies against clade B clinical isolates produced in peripheral blood mononuclear cells, J. Virol. 92 (2018), https://doi.org/10.1128/JVI.01883-17.
[53] A. Yasmeen, R. Ringe, R. Derking, A. Cupo, J.-P. Julien, D.R. Burton, A.B. Ward, I. A. Wilson, R.W. Sanders, J.P. Moore, P.J. Klasse, Differential binding of neutralizing and non-neutralizing antibodies to native-like soluble HIV-1 Env trimers, uncleaved Env proteins, and monomeric subunits, Retrovirology 11 (2014) 41, https://doi.org/10.1186/1742-4690-11-41.
[54] I.A. Abela, L. Berlinger, M. Schanz, L. Reynell, H.F. Günthard, P. Rusert, A. Trkola, Cell-cell transmission enables HIV-1 to evade inhibition by potent CD4bs directed antibodies, PLoS Pathog. 8 (2012) e1002634, https://doi.org/10.1371/journal.ppat.1002634.
[55] Y.Z. Cohen, J.C.C. Lorenzi, M.S. Seaman, L. Nogueira, T. Schoofs, L. Krassnig, A. Butler, K. Millard, T. Fitzsimons, X. Daniell, J.P. Dizon, I. Shimeliovich, D. C. Montefiori, M. Caskey, M.C. Nussenzweig, Neutralizing activity of broadly neutralizing anti-HIV-1 antibodies against clade B clinical isolates produced in peripheral blood mononuclear cells, J. Virol. 92 (2018), https://doi.org/10.1128/JVI.01883-17.
[56] N.E. Webb, D.C. Montefiori, B. Lee, Dose–response curve slope helps predict therapeutic potency and breadth of HIV broadly neutralizing antibodies, Nat. Commun. 6 (2015) 8443, https://doi.org/10.1038/ncomms9443.
[57] C. Gaebler, L. Nogueira, E. Stoffel, T.Y. Oliveira, G. Breton, K.G. Millard, M. Turroja, A. Butler, V. Ramos, M.S. Seaman, J.D. Reeves, C.J. Petropoulos, I. Shimeliovich, A. Gazumyan, C.S. Jiang, N. Jilg, J.F. Scheid, R. Gandhi, B. D. Walker, M.C. Sneller, A. Fauci, T.-W. Chun, M. Caskey, M.C. Nussenzweig, Prolonged viral suppression with anti-HIV-1 antibody therapy, Nature 606 (2022) 368–374, https://doi.org/10.1038/s41586-022-04597-1.
[58] D. Polo-Megías, M. Cano-Muñoz, A.G. Berruezo, G. Laumond, C. Moog, F. Conejero-Lara, Investigating vulnerability of the conserved SARS-CoV-2 spike's heptad repeat 2 as target for fusion inhibitors using chimeric miniproteins, Int. J. Biol. Macromol. 262 (2024) 130132, https://doi.org/10.1016/j.ijbiomac.2024.130132.
[59] M. Cano-Muñoz, D. Polo-Megías, A. Cámara-Artigas, J.A. Gavira, M.J. López-Rodríguez, G. Laumond, S. Schmidt, J. Demiselle, S. Bahram, C. Moog, F. Conejero-Lara, Novel chimeric proteins mimicking SARS-CoV-2 spike epitopes with broad inhibitory activity, Int. J. Biol. Macromol. 222 (2022) 2467–2478, https://doi.org/10.1016/j.ijbiomac.2022.10.031.
[60] V. Mangala Prasad, D.P. Leaman, K.N. Lovendahl, J.T. Croft, M.A. Benhaim, E. A. Hodge, M.B. Zwick, K.K. Lee, Cryo-ET of Env on intact HIV virions reveals structural variation and positioning on the gag lattice, Cell 185 (2022) 641–653. e17, https://doi.org/10.1016/j.cell.2022.01.013.
[61] G.B. Melikyan, HIV entry: a game of hide-and-fuse? Curr. Opin. Virol. 4 (2014) 1–7, https://doi.org/10.1016/j.coviro.2013.09.004.
[62] K. Miyauchi, Y. Kim, O. Latinovic, V. Morozov, G.B. Melikyan, HIV enters cells via endocytosis and dynamin-dependent fusion with endosomes, Cell 137 (2009) 433–444, https://doi.org/10.1016/j.cell.2009.02.046.
[63] M. Marin, Y. Kushnareva, C.S. Mason, S.K. Chanda, G.B. Melikyan, HIV-1 fusion with CD4+ T cells is promoted by proteins involved in endocytosis and intracellular membrane trafficking, Viruses 11 (2019) 1–16, https://doi.org/10.3390/v11020100.
[64] C. Wu, I.T. Raheem, D.D. Nahas, M. Citron, P.S. Kim, D.C. Montefiori, E. A. Ottinger, R.W. Hepler, R. Hrin, S.B. Patel, S.M. Soisson, J.G. Joyce, Stabilized trimeric peptide immunogens of the complete HIV-1 gp41 N-heptad repeat and their use as HIV-1 vaccine candidates, Proc. Natl. Acad. Sci. U. S. A. 121 (2024) e2317230121, https://doi.org/10.1073/pnas.2317230121.
[65] M.M. Alam, T. Kuwata, K. Tanaka, M. Alam, S. Takahama, K. Shimura, M. Matsuoka, N. Fukuda, H. Morioka, H. Tamamura, S. Matsushita, Synergistic inhibition of cell-to-cell HIV-1 infection by combinations of single chain variable fragments and fusion inhibitors, Biochem. Biophys. Rep. 20 (2019) 100687, https://doi.org/10.1016/j.bbrep.2019.100687.
[66] G. Ozorowski, J. Pallesen, N. De Val, D. Lyumkis, C.A. Cottrell, J.L. Torres, J. Copps, R.L. Stanfield, A. Cupo, P. Pugach, J.P. Moore, I.A. Wilson, A.B. Ward, Open and closed structures reveal allostery and pliability in the HIV-1 envelope spike, Nature 547 (2017) 360–361, https://doi.org/10.1038/nature23010.
[67] K.A. Nagashima, D.A.D. Thompson, S.I. Rosenfield, P.J. Maddon, T. Dragic, W. C. Olson, Human immunodeficiency virus type 1 entry inhibitors PRO 542 and T-20 are potently synergistic in blocking virus-cell and cell-cell fusion, J. Infect. Dis. 183 (2001) 1121–1125, https://doi.org/10.1086/319284.
[68] N.N. Mkhize, A.E.J. Yssel, H. Kaldine, R.T. van Dorsten, A.S. Woodward Davis, N. Beaume, D. Matten, B. Lambson, T. Modise, P. Kgagudi, T. York, D.H. Westfall, E.E. Giorgi, B. Korber, C. Anthony, R.E. Mapengo, V. Bekker, E. Domin, A. Eaton, W. Deng, A. DeCamp, Y. Huang, P.B. Gilbert, A. Gwashu-Nyangiwe, R. Thebus, N. Ndabambi, D. Mielke, N. Mgodi, S. Karuna, S. Edupuganti, M.S. Seaman, L. Corey, M.S. Cohen, J. Hural, M.J. McElrath, J.I. Mullins, D. Montefiori, P.

L. Moore, C. Williamson, L. Morris, Neutralization profiles of HIV-1 viruses from the VRC01 Antibody Mediated Prevention (AMP) trials, PLoS Pathog. 19 (2023) e1011469, https://doi.org/10.1371/journal.ppat.1011469.

Supplementary Information to:

Potent HIV-1 miniprotein inhibitors targeting highly conserved gp41 epitopes

Daniel Polo-Megías[a], Mario Cano-Muñoz[a,1], Pierre Gantner[b], Géraldine Laumond[b], Thomas Decoville[b], Jasmine Grezzani[a], Ilaria La Rocchia[a], M. Carmen Salinas-Garcia[a], Ana Cámara-Artigas[c], José A. Gavira[d], Francisco Conejero-Lara[a,*] & Christiane Moog[b,e,*]

[a] Departamento de Química Física, Instituto de Biotecnología e Unidad de Excelencia de Química Aplicada a Biomedicina y Medioambiente (UEQ), Facultad de Ciencias, Universidad de Granada, 18071 Granada, Spain.

[b] Laboratoire d'ImmunoRhumatologie Moléculaire, Institut National de la Santé et de la Recherche Médicale (INSERM) UMR_S 1109, Institut Théematique Interdisciplinaire (ITI) de Médecine de Précision de Strasbourg, Transplantex NG, Faculté de Médecine, Fédération Hospitalo-Universitaire OMICARE, Fédération de Médecine Translationnelle de Strasbourg (FMTS), Université de Strasbourg, F-670. 00 Strasbourg, France.

[c] Department of Chemistry and Physics, University of Almería, Agrifood Campus of International Excellence (ceiA3), Research Centre for Agricultural and Food Biotechnology (BITAL), Carretera de Sacramento s/n, Almería, 04120, Spain

[d] Laboratorio de Estudios Cristalográficos, CSIC, Armilla, 18100 Granada, Spain.

[e] Vaccine Research Institute (VRI), F-94000 Créteil, France.

[1]Present address: Department of Biotechnology and Environmental Protection, Estación Experimental del Zaidín, Consejo Superior de Investigaciones Científicas, Granada, 18008, Spain.

Table of Contents

1. Design of covNHR-N miniproteins

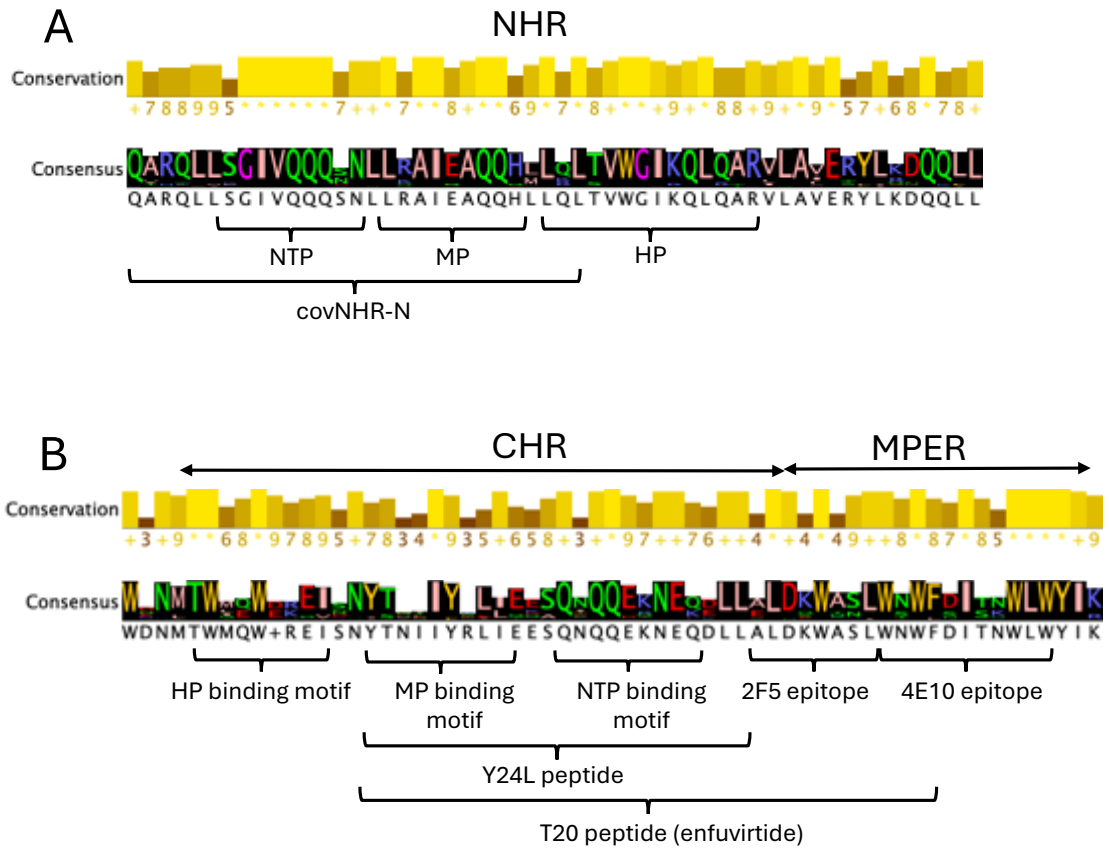

Figure S1. Sequence conservation and consensus sequence of NHR, CHR and MPER in gp41. The plots have been made with Jalview [1] using the 2022 Compendium sequence alignment from Los Alamos Sequence Database (https://www.hiv.lanl.gov). **A)** NHR region. The sequence location of the N-terminal polar pocket (NTP), the middle pocket (MP) and the hydrophobic pocket (HP) are indicated with braces [2]. The NHR sequence covered by the mimetic covNHR-N miniprotein is also indicated. **B)** CHR and MPER regions. The different braces indicate the sequence locations of the conserved HP and NTP binding motifs and the positions of the 2F5 and 4E10 core epitopes. The sequences covered by the Y24L and T20 (enfuvirtide) peptides are also indicated.

Appendix S1. Computer modeling of FPPR-extended NHR-mimetic miniproteins

We used as scaffold a previously designed covNHR-N miniprotein [3,4], which was modelled using the crystallographic structure of our previous covNHR construct in complex with the C34 peptide [5]. The covNHR-N mimetic protein imitates the N-terminal half of the gp41 NHR region in a trimeric coiled-coil conformation and binds the C-terminal half of CHR. This miniprotein construct was further stabilized by a triad of Gln-Ile mutations (Q23I, Q41I and Q86I; Table S1) as described in the main text, giving rise to a hyperstable miniprotein (named here Q23I).

To graft in the Q23I miniprotein an additional motif that would interact with the MPER region downstream of the CHR, we used as template the crystallographic structure of a gp41 construct in a fusion-intermediate conformation [6] that includes the fusion-peptide proximal region (FPPR) and the membrane proximal external region (MPER) (PDB id. 2X7R). We structurally aligned the NHR helical regions between Q23I and 2X7R (Figure S2A). Then, we removed the loop connecting the second and third helices of Q23I and extended N-terminally the first and third helices with the corresponding gp41 sequence, following as a guide the conformation of the template structure 2X7R. Similarly, the second inverse helix in Q23I was extended C-terminally with the corresponding reversed sequence (Figure S2B). We created two versions of the extended constructs with different lengths of the FPPR extensions.

The extended second and third helices were then linked with short poly-Gly loops modelled manually, trying to set a similar loop conformation as that of the Q23I construct, while keeping the psi and phi angles at allowed values. Once the loops were built, we designed a disulfide bond tethering the N-terminus with the loops by mutating residues to Cys at appropriate positions, compatible with disulfide bond formation. The constructs were then relaxed by energy minimization using YASARA Structure[7]. Finally, residues at the loops and near the loop anchors were rationally engineered with the aid of RosettaDesign [8], designing stabilizing interactions (Figure S3). In this engineering process, the groove between helix 1 and helix 3 was left intact. All the protein sequences contain a C-terminal His-tag to facilitate purification. The final sequences and physical properties are collected in Tables S1 and S2.

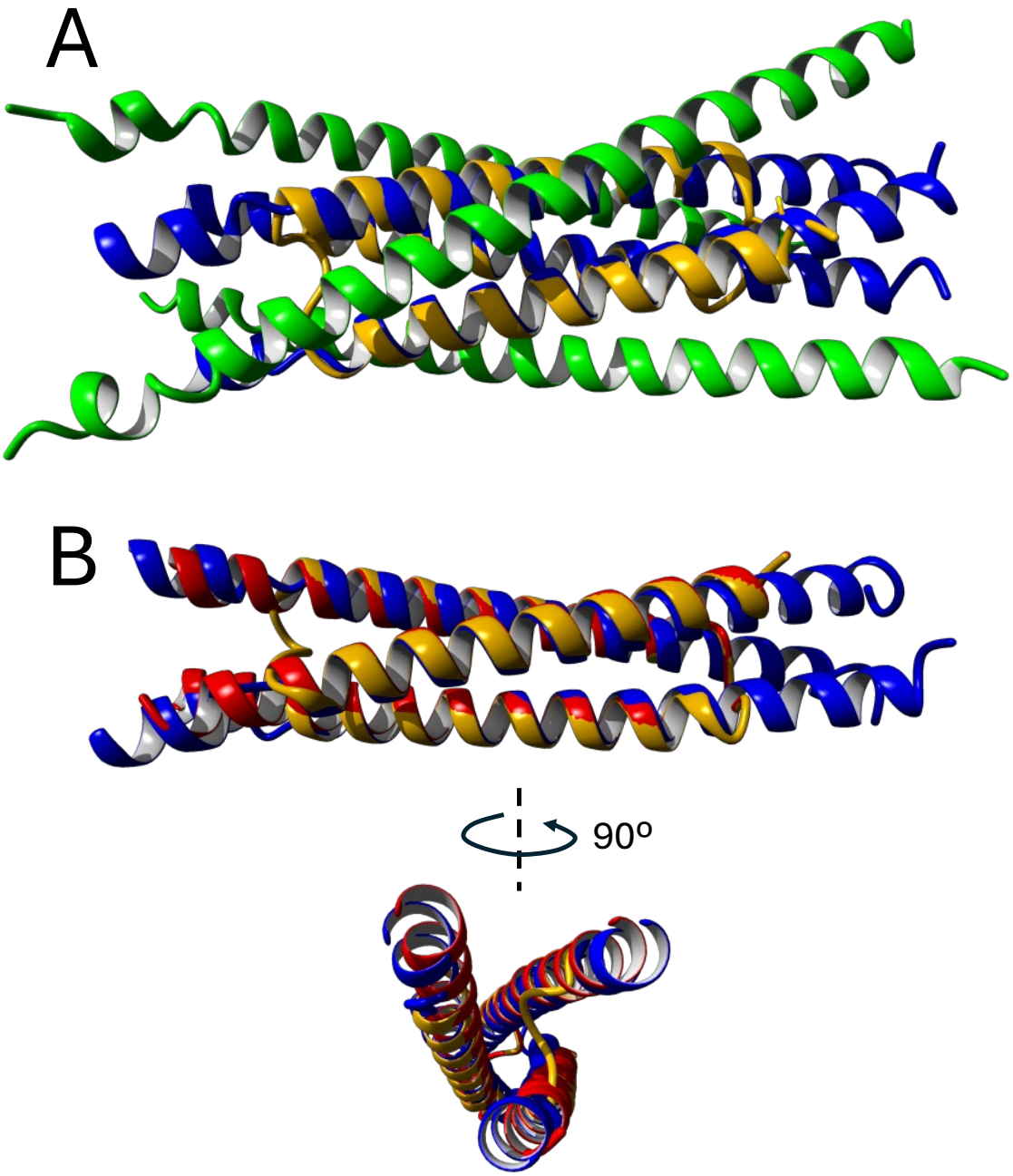

Figure S2: Templated modeling covNHR-N miniproteins. A) Structural alignment between the covNHR-N miniprotein model and the gp41 construct including the FPPR and MPER regions in a fusion intermediate conformation (PDB id. 2X7R [6]). In the 2X7R construct, the FPPR-NHR chains (gp41 residues 534-581) are colored in blue and the CHR-MPER chains (gp41 residues 624-677) in green. The covNHR-N miniprotein is colored in orange. B) Superposition between the FPPR-NHR region of 2X7R (blue), the Q23I miniprotein (orange) and a construct with FPPR-extended helices (red).

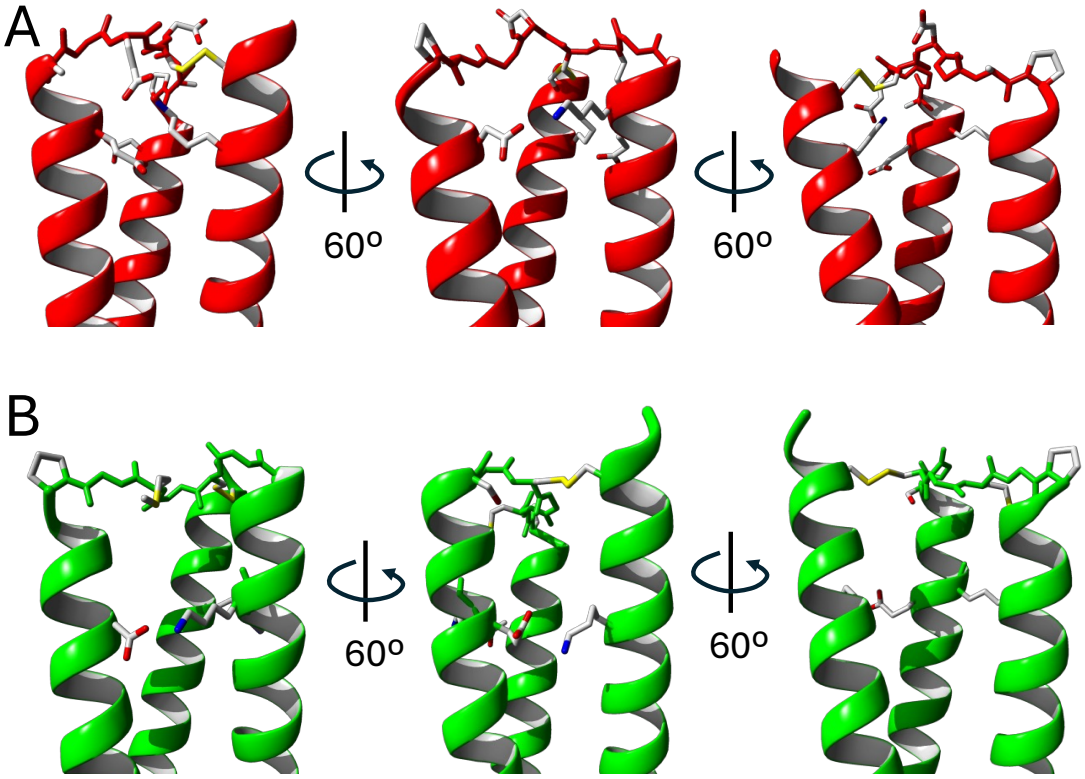

Figure S3. Loop design connecting the covNHR-N helices. Schematic representation of the loop designs for the extended constructs Q23I-ex1 **(A)** and Q23I-ex2 **(B)**. The loops have been represented with sticks, whereas the rest of the polypeptide chain is represented with ribbons. The residue side chains that were engineered to additionally stabilize the constructs are also highlighted with sticks and colored in CPK scheme.

Table S1. Amino acid sequences of the covNHR-N miniproteins

covNHR-N-dSS[(a)]	Helix 1	MCRQKLSGIVQKQNNLLRKIEAQQHLLQR
Q23I		MCRQKLSGIVQKQNNLLRKIEAIQHLLQR
Q23I-ex1		MACMTKTVQARQKLSGIVQKQNNLLRKIEAIQHLLQR
Q23I-ex2		MTCGAASMTKTVQARQKLSGIVQKQNNLLRKIEAIQHLLQR
covNHR-N-dSS	Loop 1	GLICG
Q23I		GLICG
Q23I-ex1		GLICG
Q23I-ex2		GLICG
covNHR-N-dSS	Helix 2	PQLLHQQAEIERELNNQEQEIGSLKQR
Q23I		PQLLHQIAEIERELNNQEQEIGSLKQR
Q23I-ex1		PQLLHQIAEIERELNNQEQEIGSLKQRAQVEKTA
Q23I-ex2		PQLLHQIAEIERELNNQEQEIGSLKQRAQVEKTMSAAS
covNHR-N-dSS	Loop 2	GCIDG
Q23I		GCMG
Q23I-ex1		GECDGA
Q23I-ex2		GCGMG
covNHR-N-dSS	Helix 3	PLLSGIDQQQNNLKRAIEAQKHLLQLTCW
Q23I		PLLSGIDQQQNNLKRAIEAIKHLLQLTCW
Q23I-ex1		PTLDVQARQLLSGIDQQQNNLKRAIEAIKHLLQLTCW
Q23I-ex2		PASMTLDVQARQLLSGIDQQQNNLKRAIEAIKHLLQLTCW

[(a)] Ref. [4]
[(b)] All the proteins contain the C-terminal sequence GGGGSHHHHHH

Table S2: Molecular characteristics of covNHR-N miniproteins

Protein	Number of residues	Molar mass (Da)	Extinction coeff. at 280 nm [(a)] (M^{-1} cm^{-1})	α-helix % (number of residues) at pH 7.4 and 25°C [(b)]
Q23I	106	12010.83	5750	58.0% (62)
Q23I-ex1	130	14568.69	5750	53.6% (70)
Q23I-ex2	140	15423.74	5750	57.0% (80)

[(a)] Estimated according to Expasy ProtParam (https://web.expasy.org/protparam/).
[(b)] Calculated from the mean-residue molar ellipticity at 222 nm of the CD spectra according to Luo & Baldwin [9].

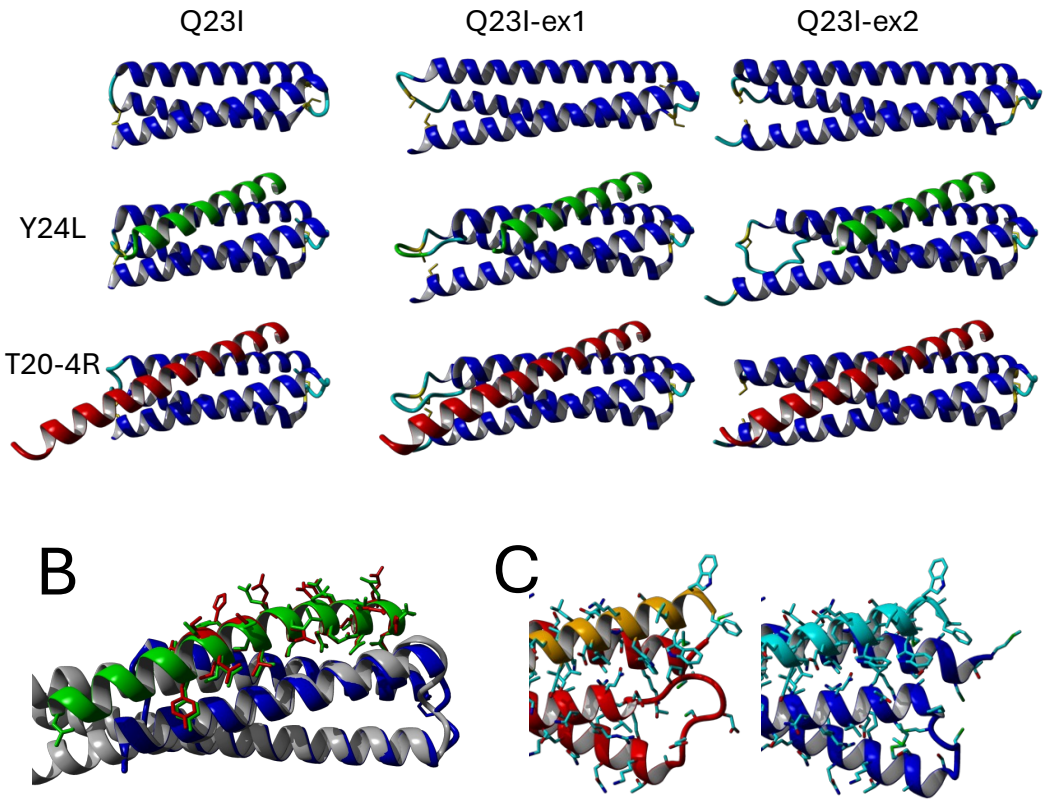

Figure S4. Structure predictions with Alphafold 2. (A) Predictions of the three-dimensional structures of the covNHR-N miniproteins and their complexes with the gp41 peptides from their amino acid sequences using Alphafold 2 server "Colabfold" with no template option [10]. The images show ribbon representations of each predicted structure. The miniproteins are colored in blue (helical regions) and cyan (loop regions). The Cys side chains are represented with sticks and colored in yellow. The Y24L peptide is colored in green and the T20-4R peptide in red. The His-tags in the proteins and the four Arg residues in T20-4R were omitted for clarity. **(B)** Structural alignment between the Q23I-Y24L complex predicted by Alphafold2 and the crystallographic structure of the covNHR protein in complex with the C34 peptide (PDB code 6R2G) [5]. **(C)** Details of the predicted interactions of the MPER residues of T20-4R (orange and cyan, respectively) with the FPPR extensions of Q23I-ex1 (left, color red) and Q23I-ex2 (right, color blue). The predicted structures of the three miniproteins are very similar to the designed models, except for local differences in the loops connecting the helices and the absence of some disulfide bonds in some of the predicted models. The interactions at the protein-peptide interface resemble very much to those observed in the experimental structures used as templates in the designs. Remarkably, the MPER region of the T20-4R peptide is predicted to have a helical structure in the complexes, irrespectively of the presence of the FPPR extension.

2. Biophysical characterization of covNHR-N miniproteins

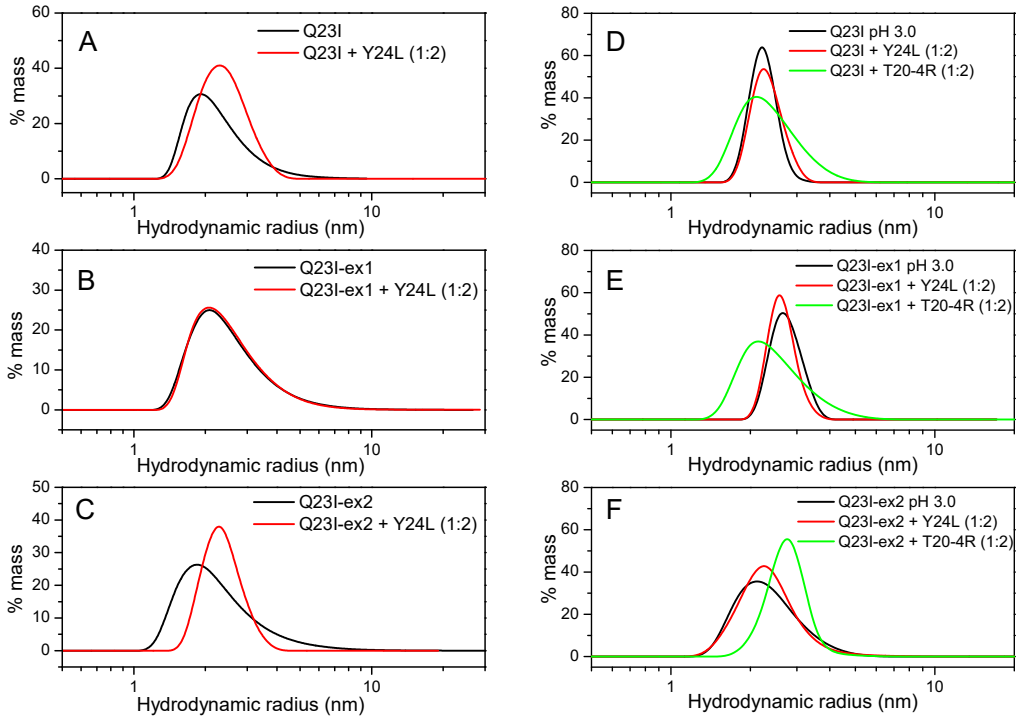

Figure S5: Molecular size of covNHR-N miniproteins. Hydrodynamic radius distributions measured by dynamic light scattering (DLS). Measurements were carried out at 25 °C in 50 mM sodium phosphate buffer pH 7.4 (A-C) and 50 mM glycine/HCl pH 3.0 (D-F). (A) and (D) Q23I; (B) and (E) Q23I-ex1; (C) and (F) Q23I-ex2. Black lines represent the hydrodynamic radius distribution of the free proteins and red and green lines correspond to the mixtures of each protein with a 2:1 excess of Y24L or T20-4R peptide.

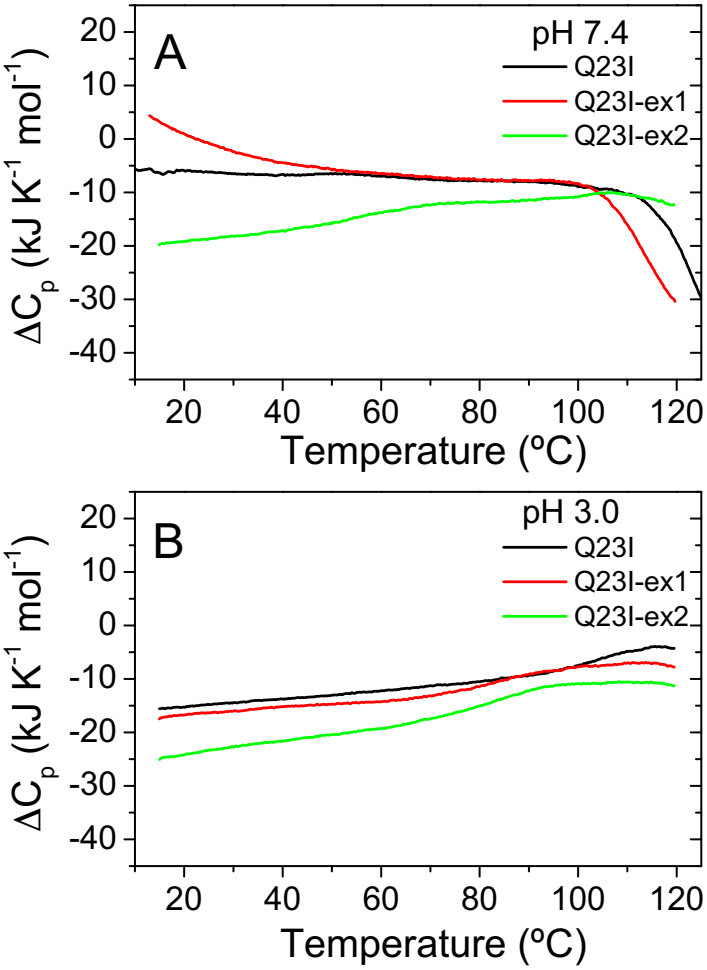

Figure S6: Thermal stability of the covNHR-N miniproteins. DSC thermograms measured in 50 mM sodium phosphate buffer pH 7.4 (A) and 50 mM glycine/HCl pH 3.0 (B). Scans were carried out at 90 °C/h with 30 μM protein solutions.

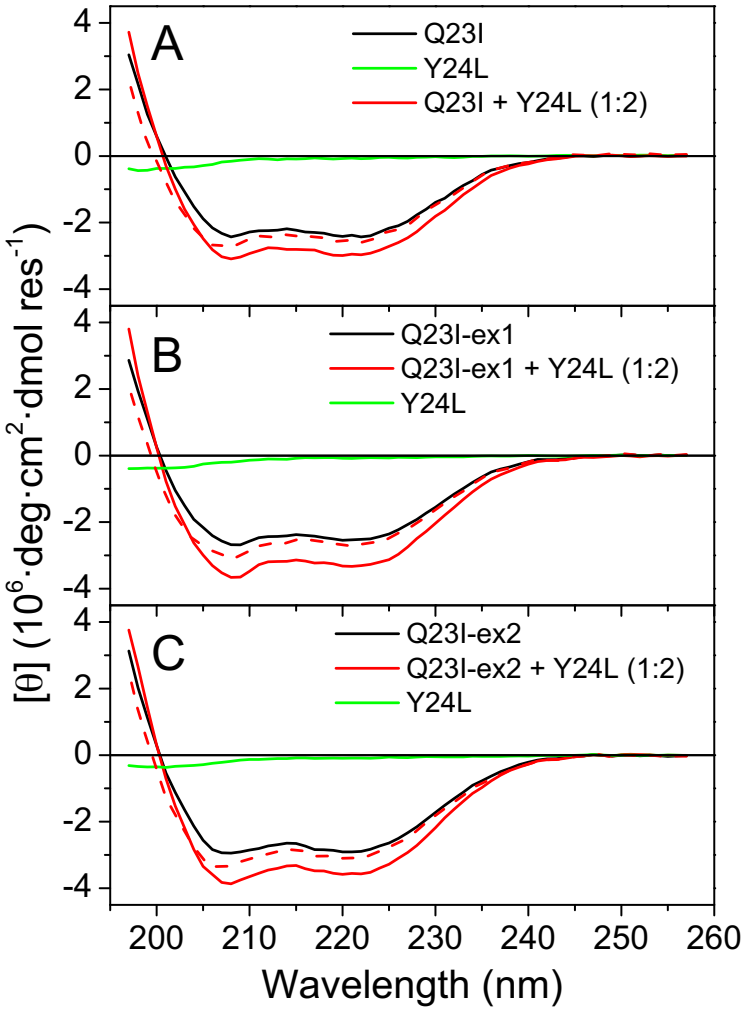

Figure S7: Effect of peptide binding on α-helix structure (pH 7.4). Far-UV CD spectra of the covNHR-N miniproteins in free form (black) and in 1:2 mixtures with Y24L peptides (red). Spectra were recorded in 50 mM sodium phosphate buffer pH 7.4 at 25 °C and normalized as ellipticity per mole of protein or peptide. For comparison, the CD spectra of the free peptide (green) and the theoretical sum of the spectra of the free molecules in 1:2 ratio (red dashed lines) are also shown. Data are plotted as follows: Q23I (A); Q23I-ex1 (B); Q23I-ex2 (C).

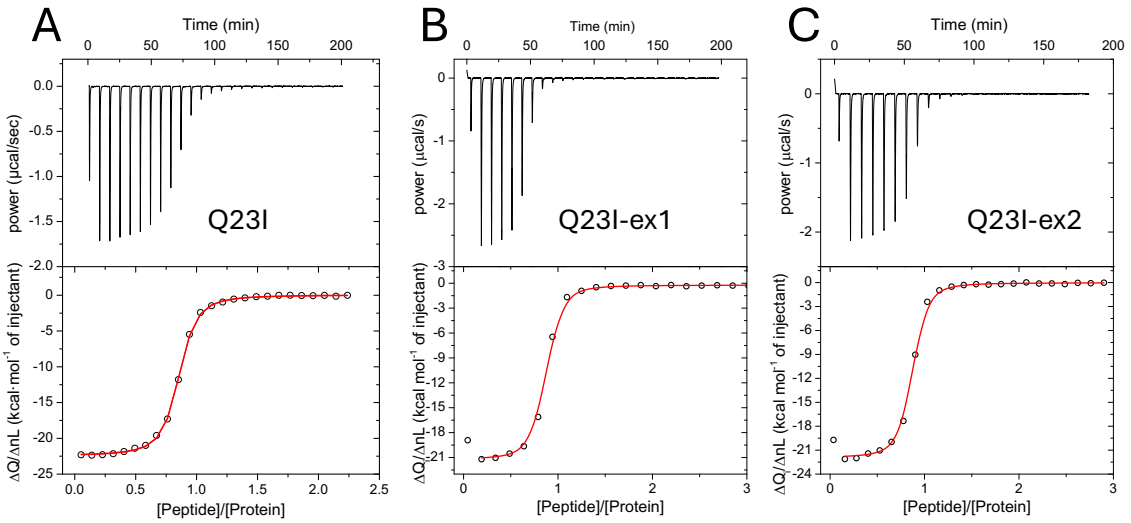

Figure S8: ITC titrations of each covNHR-N miniprotein with CHR-derived peptide at pH 7.4. Isothermal titration calorimetry (ITC) experiments carried out by titration with Y24L peptide (gp41 residues Tyr638–Leu661) on each covNHR-N miniprotein. (A) Q23I; (B): Q23I-ex1; (C) Q23I-ex2. Experiments were carried out at 25 °C in 50 mM sodium phosphate buffer pH 7.4. Upper panels correspond to the baseline-corrected thermograms obtained with 25-30 injections of peptide sample on a protein solution. Bottom panels correspond to the heats normalized per mole of injected ligand (symbols) versus the protein:peptide molar ratio. The red solid lines correspond to the best fits of the binding curves using a binding model of n independent and identical sites.

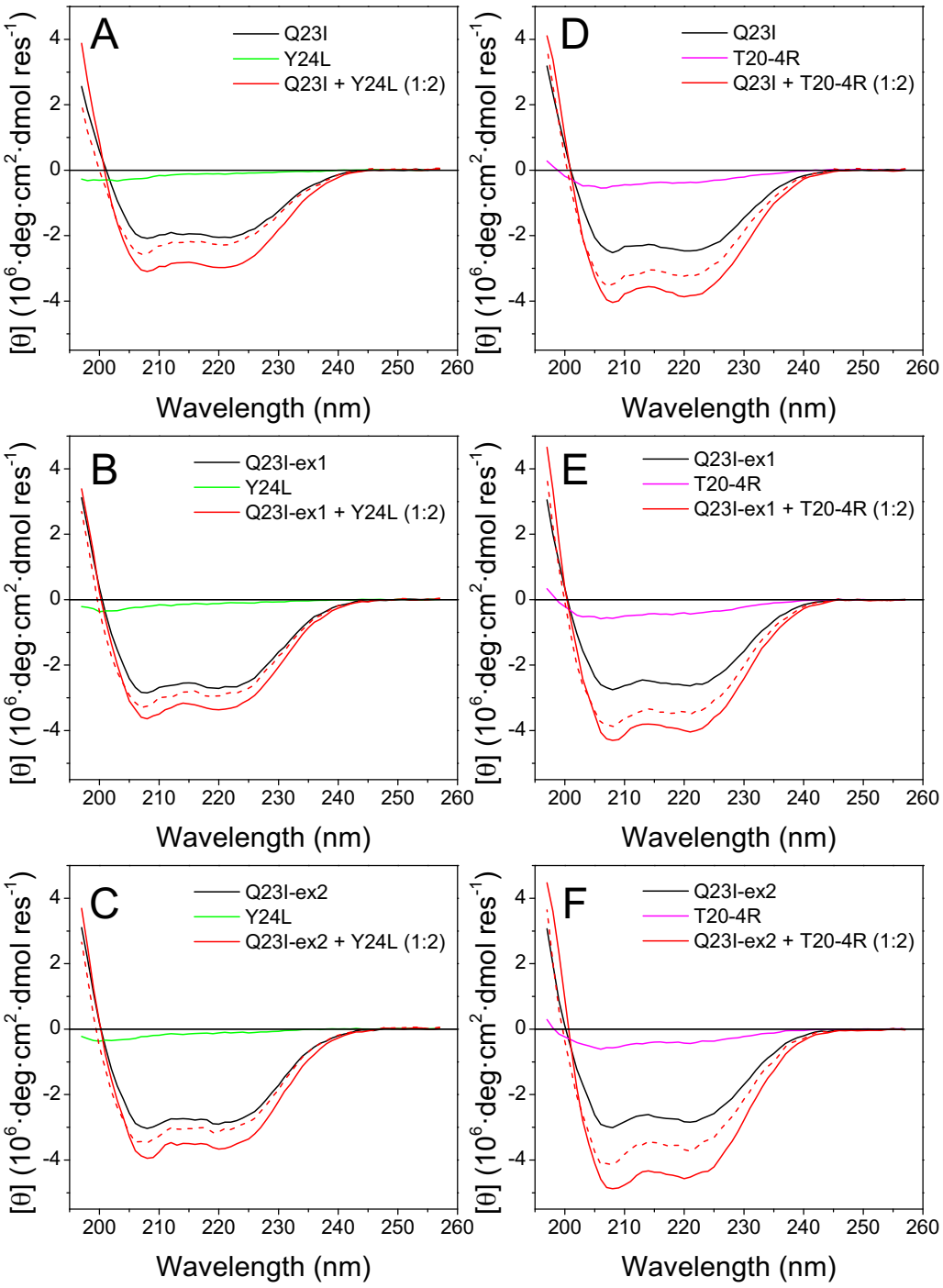

Figure S9: Effect of peptide binding on α-helix structure (pH 3.0). Far-UV CD spectra of the covNHR-N miniproteins in free form and in 1:2 mixtures with gp41 peptides. Spectra were recorded in 50 mM glycine/HCl buffer pH 3.0 at 25 °C and normalized as ellipticity per mole of protein or peptide.For comparison, the CD spectra of the free peptide and the theoretical sum of the spectra (dashed lines) of the free molecules in 1:2 ratio are also shown. Data are plotted as follows: Q23I (A and B); Q23I-ex1 (C and D); Q23I-ex2 (E and F); Y24L (A,C and E); T20-4R (B,D and F).

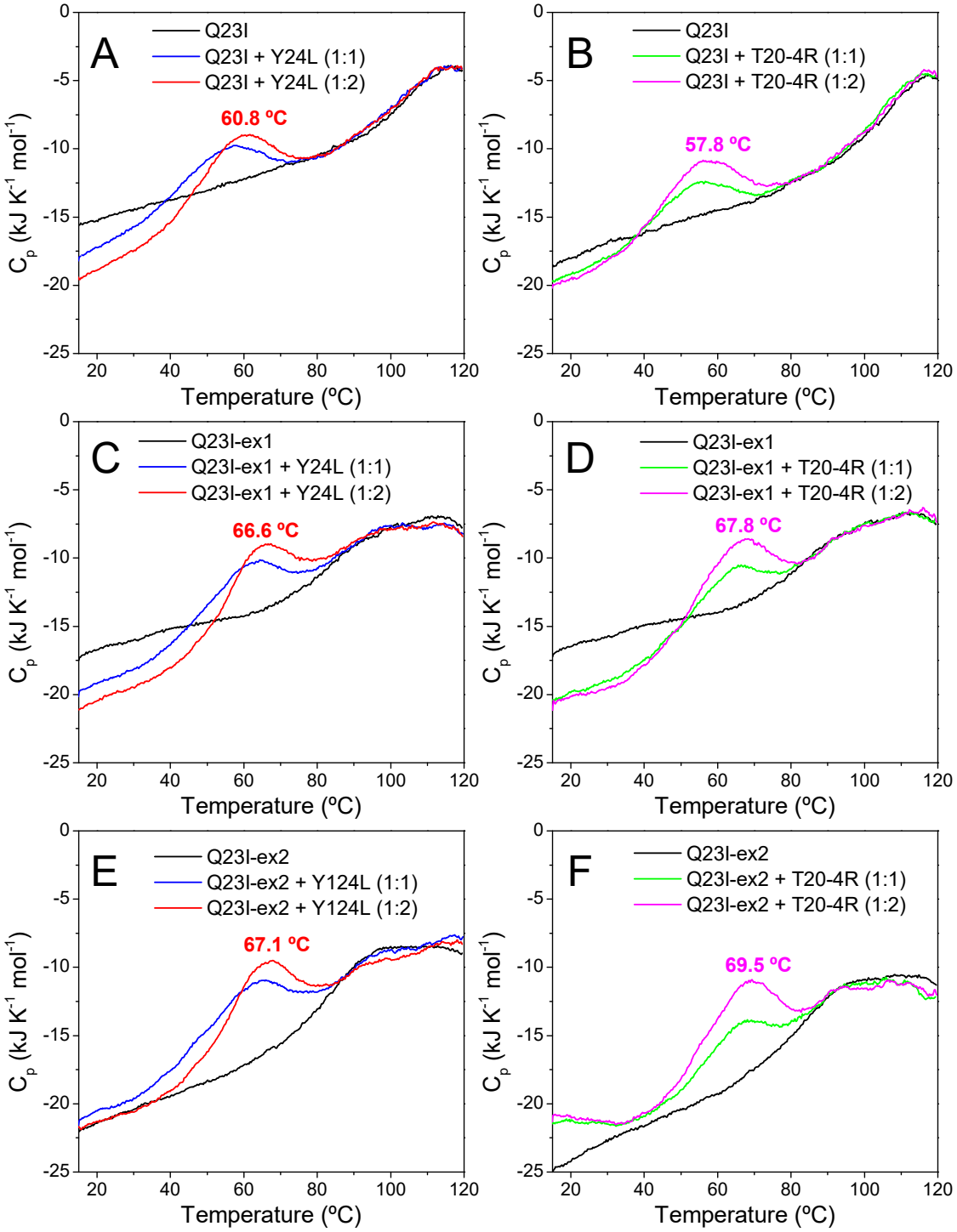

Figure S10: Effect of peptide binding on the thermal stability of the covNHR-N miniproteins. DSC experiments were performed using a scan rate of 90 °C/h. Samples were prepared at 30 µM of protein concentration in 50 mM glycine/HCl buffer pH 3.0. Peptides were added in the mixtures at the indicated molar ratios. Data are plotted as follows: Q23I (A and B); Q23I-ex1 (C and D); Q23I-ex2 (E and F); Y24L (A,C and E); T20-4R (B,D and F). The heat capacity of the free peptides was recorded independently and subtracted from the thermograms for the sake of clarity of the observed effects. The temperature of the dissociation peak at 1:2 molar ratio is indicated along each curve.

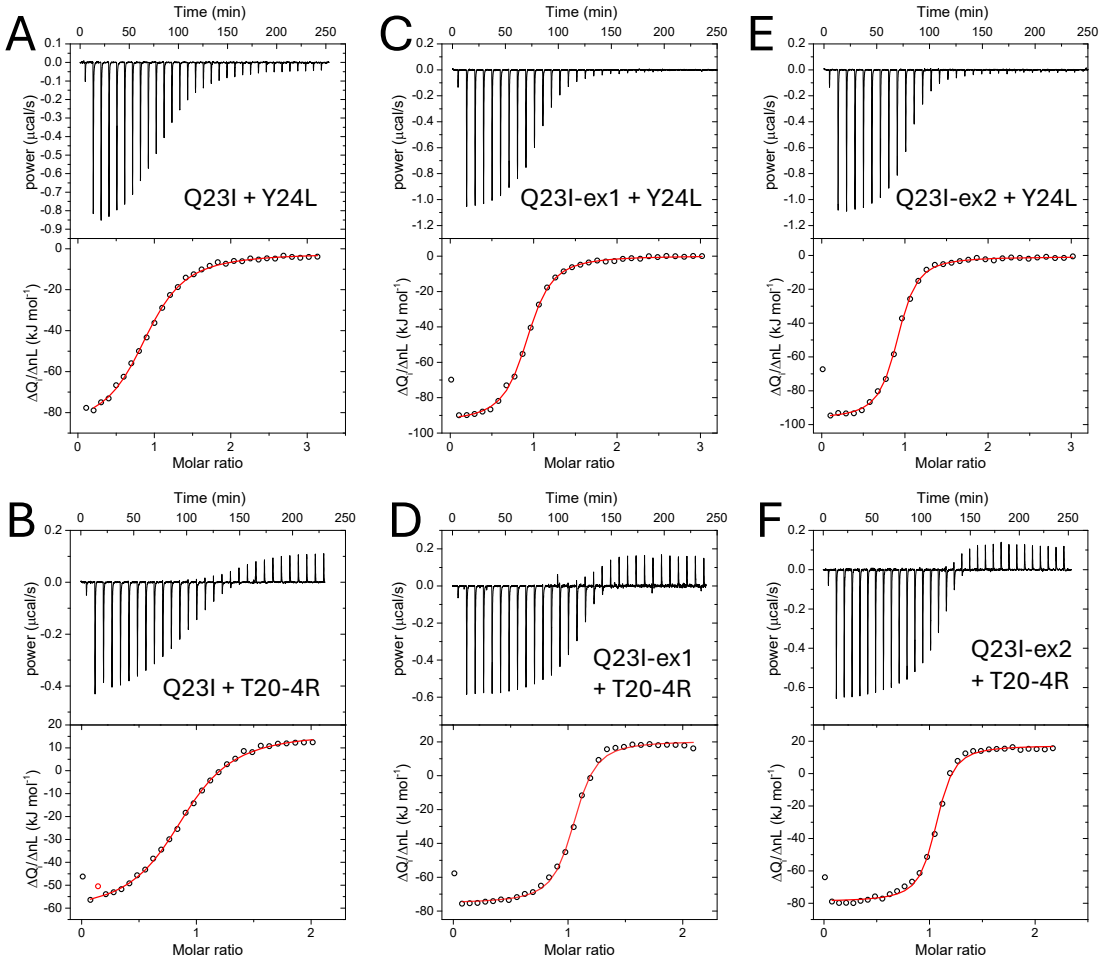

Figure S11: ITC titrations of each covNHR-N miniprotein with gp41 derived peptides at pH 3.0. Q23I (A and B), Q23I-ex1 (C and D) and Q23I-ex2 (E and F) were titrated with the Y24L (A, C, E) or T20-4R (B, D, F) peptides. Experiments were carried out at 25 °C in 50 mM glycine/HCl buffer pH 3.0. Upper panels in each graph show the baseline corrected thermograms. Lower panels show the normalized binding heats (open symbols) and the corresponding fittings (red lines) using a binding model of independent and identical sites.

3. X-Ray Crystallography

Table S3.-X-Ray diffraction data collection and refinement statistics

PDB entry	9HS7
Beamline	XALOC (ALBA)
Data collection temperature (K)	100
Wavelength (Å)	0.979
Resolution range (Å)	19.29-1.70 (1.90-1.70)
Space group	*P*65
a, b, c (Å)	65.44 65.44 88.77
α, β, γ (°)	90 90 120
Total reflections	117185 (5732)
Unique reflections	11436 (572)
Multiplicity	10.2 (10.0)
Completeness (%)	99.81 (100.00)
Mean *I/σ(I)*	24.52 (3.71)
spherical	48.1 (8.2)
ellipsoidal	94.1 (86.9)
Wilson *B* factor (Å^2)	35.92
R_{merge}	0.075 (0.991)
$CC_{1/2}$	1 (0.752)
Reflections used in refinement	11432 (416)
R_{work}	0.203 (0.318)
R_{free}	0.239 (0.242)
No. of non-H atoms	1026
Ligands	1
Solvent	35
No. of protein residues	126
R.m.s.d., bonds (Å)	0.014
R.m.s.d., angles (°)	1.401
Ramachandran favoured (%)	95.97
Ramachandran allowed (%)	100.00
Ramachandran outliers (%)	0
Rotamer outliers (%)	0
Clashscore	0
Average *B* factor (Å^2)	58.62

4. TZM-Bl inhibition assays

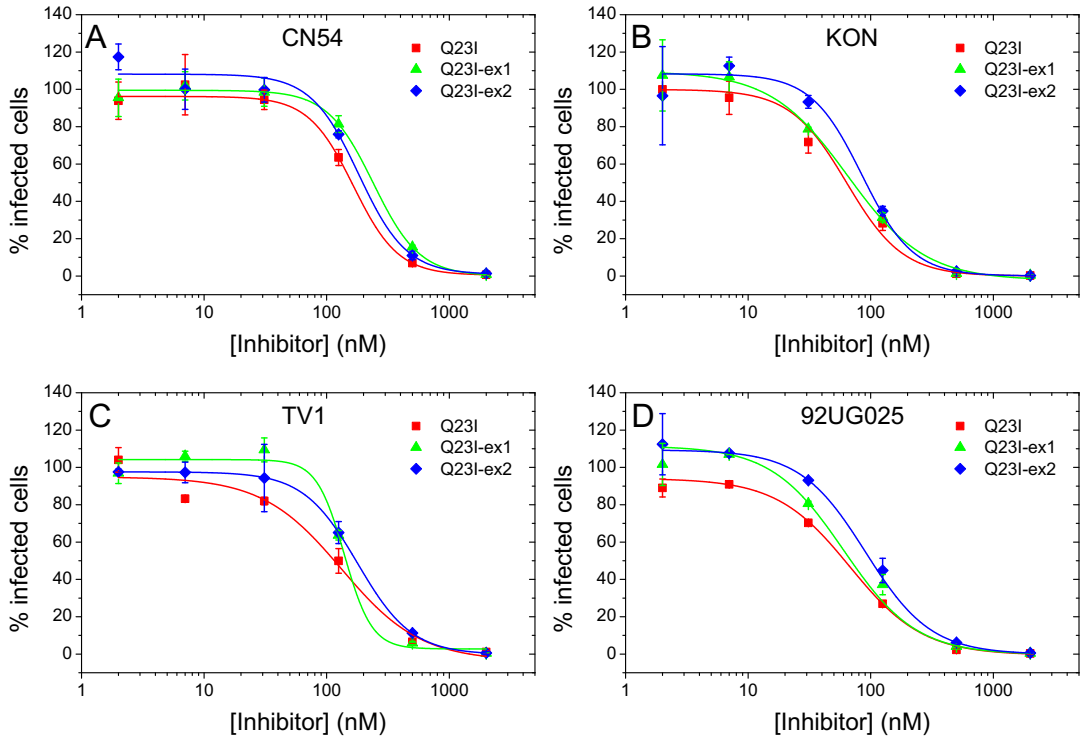

Figure S12: TZM-Bl cell infection assays in presence of the inhibitory covNHR-N miniproteins for several viral strains. TZM-Bl cells were infected with different Tier 2 HIV isolates in presence of variable concentrations of covNHR-N miniproteins. HIV used were CN54 **(A)**, KON **(B)**, TV1 **(C)** and 92UG025 **(D)**. Data correspond to the percentage of infected cells relative to the controls in absence of inhibitor. The lines represent the best fit using a Hill's sigmoidal function. Error bars correspond to the standard deviation from the mean values from duplicates.

Table S4. 50% inhibitory concentrations (IC_{50}) in nM of covNHR-N miniproteins in TZM-Bl assay for several HIV-1 strains

Virus strain	CN54	KON	TV1	92UG025
Subtype (tropism)	C (R5)	CRF02-AG (X4)	C (R5)	C (R5)
Q23I	165 ± 5	64 ± 13	132 ± 52	68 ± 4
Q23I-ex1	240 ± 9	65 ± 6	139 ± 38	60 ± 4
Q23I-ex2	182 ± 16	85 ± 8	178 ± 0.4	91 ± 2

The 50% inhibitory concentrations (IC_{50}) have been obtained by fitting the change in percentage of infected cells with the inhibitor concentration using a Hill's sigmoidal function.

5. Cytotoxicity assays

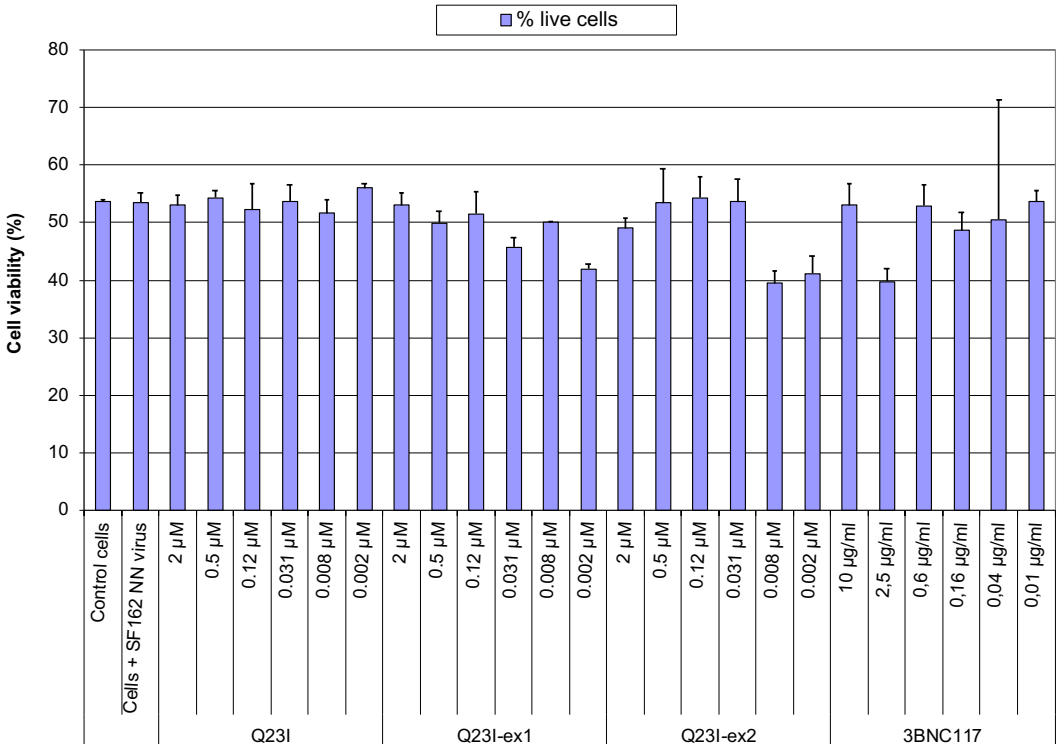

Figure S13: Cytotoxicity of the covNHR-N miniproteins on PMBC cells. LIVE/DEAD™ experiments were in parallel to p24 detection by ELISA in the PMBC infection assays with SF162 NN virus. Percents of live cells in presence of the miniproteins or the 3BNC117 mAb are compared with control cells and cells with added virus.

6. ELISA binding assays with Env spike

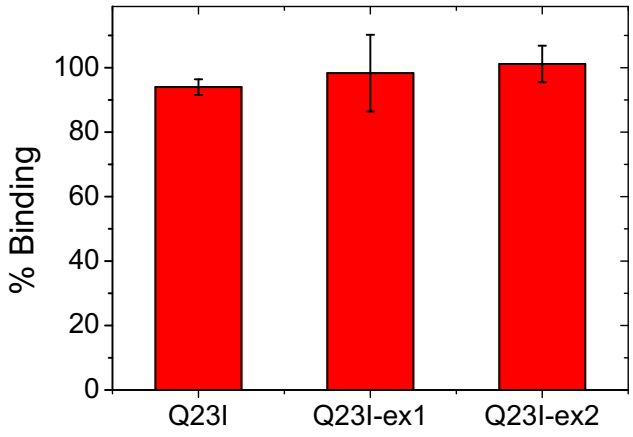

Figure S14: Binding of covNHR-N miniproteins to soluble gp160 MN/LAI Env measured by ELISA. CovNHR-N binding to Env was detected using anti-His tag Ab as primary antibody. Background binding was measured without Env and subtracted from the data. 100% positive control was measured with wells directly coated with a His-tagged Env. Data correspond to mean ± S.D. values of triplicates.

7. Capture of infectious viruses

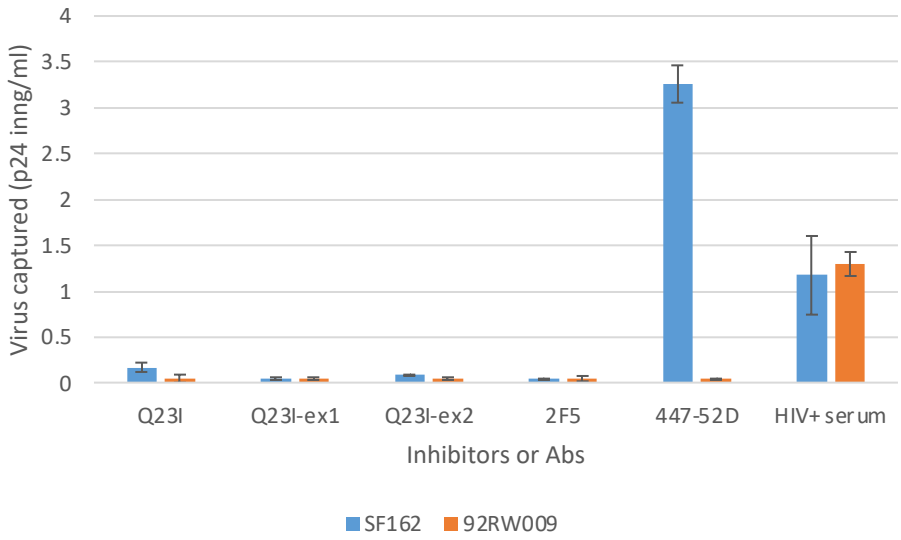

Figure S15: Capture of whole virus particles. Infections virus particles (SF162 in blue and 92RW009 in orange) were captured by miniproteins (at 20 µM) or Abs (at 5 µg/mL) previously coated on an ELISA plate. Supernatant collected after extensive washing were analyzed for p24 detection. Mean and standard deviation of duplicates.

8. Combination inhibition assays

Appendix S2: Analysis of combination inhibition experiments

TZM-Bl or PMBC assays were carried out with mixtures of covNHR-N miniproteins and bnAbs as described in the Material and Methods section of the main text. The mixtures were prepared by serial dilutions at different molar ratios, covering a concentration range around their respective IC_{50} values (see Tables S4A-C below). The percentage of infected cells in each well was calculated according to the number of infected cells, relative to the total number of living cells. Then, the percentage of inhibition for each single inhibitor and for each combination was calculated by comparing the number of infected cells in presence of inhibitor with the number of infected cells in absence of inhibitor (control), according to equation 1.

$$\%\ inhibition = \frac{100 - \%\ infected}{\%\ infected(control)} \qquad (1)$$

The inhibitor concentration leading to 50% inhibition, $IC_{50,}$ and the cooperativity parameter, m, were calculated from linear regression in double logarithmic Hill's plots using equation 2 [11] with data of single inhibitor, bnAb and fixed-ratio mixtures (see Figures S11, S14 and S18).

$$log\left(\frac{\%\ inhibition}{100 - \%inhibition}\right) = m \cdot \log\frac{[inhibitor]}{[IC_{50}]} \qquad (2)$$

Then, the combination index (CI) and dose reduction index (DRI) corresponding to different inhibition percentages were calculated for each inhibitor:bnAb mixture using equations 3 and 4 [11]. Values for fixed-ratio mixtures and for individual mixtures were calculated (Figures S12, S15, S16 and S19), where IC_x corresponds to the concentration of single inhibitor or bnAb corresponding to a certain inhibition percentage x, and $[Inhibitor]_{mix}$ or $[bnAb]_{mix}$ correspond to the concentrations of each species in the mix that produce the same percentage of inhibition. CI < 1 indicates synergism, CI = 1 indicates additive effects, and CI > 1 indicates antagonism.

$$CI_x = \frac{[Inhibitor]_{mix}}{IC_x(inhibitor)} + \frac{[bnAb]_{mix}}{IC_x(bnAb)} \qquad (3)$$

$$DRI_x = \frac{IC_x(inhibitor)}{[Inhibitor]_{mix}} \qquad (4)$$

Finally, isobolograms for each combination were calculated for IC_{50}, IC_{70} and IC_{90} according to equation 5 (Figures S13, S17, S20).

$$\frac{[Inhibitor]_{mix}}{IC_x(inhibitor)} + \frac{[bnAb]_{mix}}{IC_x(bnAb)} = 1$$

Table S5A. Combination inhibition assays with covNHR-N miniproteins and 3BNC117 in TZM-Bl assays using SF162 pseudoviruses

% inhibition in presence of 3BNC117 and Q23I.

	3BNC117 (nM)					
Q23I (nM)	4.67	1.55	0.52	0.17	0.06	0.00
500.00	99.73	99.77	99.71	99.57	98.53	97.57
166.67	99.67	98.82	96.97	93.67	94.14	87.78
55.56	98.74	98.76	91.99	85.96	72.65	75.05
18.52	96.82	91.12	82.03	56.88	43.15	34.90
6.17	92.15	89.25	70.98	45.80	37.20	22.95
0.00	90.67	77.44	76.25	41.64	33.11	38.43

% inhibition in presence of 3BNC117 and Q23I-ex1.

	3BNC117 (nM)					
Q23I-ex1 (nM)	4.67	1.55	0.52	0.17	0.06	0.00
500.00	99.83	99.63	99.80	99.36	97.84	96.99
166.67	99.66	99.21	94.31	90.14	85.64	81.38
55.56	99.17	91.59	87.48	68.61	71.56	46.74
18.52	95.11	83.04	66.90	32.88	34.05	25.20
6.17	92.30	80.56	53.40	35.31	13.39	6.87
0.00	88.88	77.13	62.78	32.01	16.88	8.67

% inhibition in presence of 3BNC117 and Q23I-ex2.

	3BNC117 (nM)					
Q23I-ex2 (nM)	4.67	1.55	0.52	0.17	0.06	0.00
500.00	100.02	99.63	99.74	100.09	97.46	94.71
166.67	100.09	99.27	95.82	87.76	82.53	84.60
55.56	97.44	94.83	83.22	77.61	60.09	51.12
18.52	96.87	88.73	72.95	58.22	29.08	50.32
6.17	95.27	82.80	58.32	36.96	33.37	5.95
0.00	91.65	75.34	66.99	25.85	-0.58	18.91

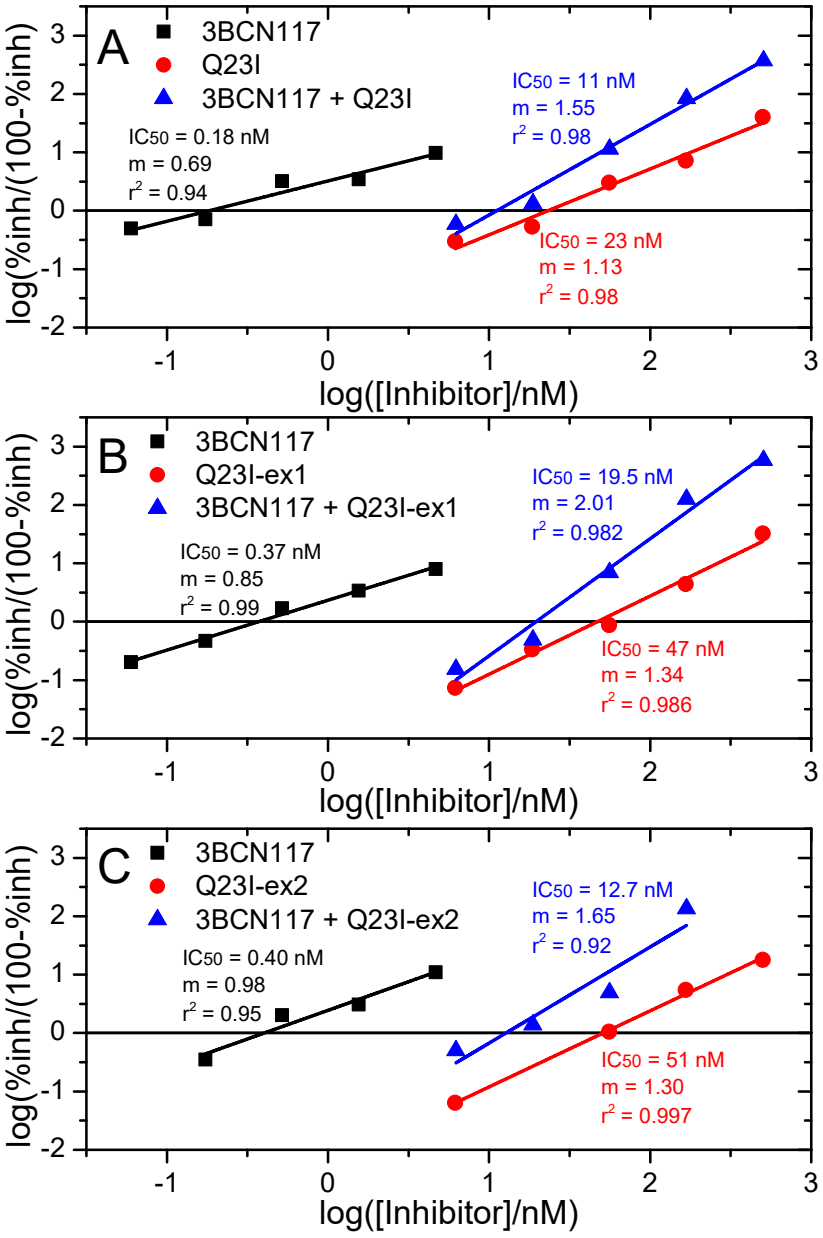

Figure S16. Combination TZM-Bl assays with 3BNC117. Hill's plots corresponding to the individual and combination inhibition assays between the covNHR-N miniproteins and 3BNC117 in TZM-Bl assays using SF162 pseudoviruses. Data correspond only to a constant [protein]/[mAb] molar ratio of 107:1 (diagonal data).

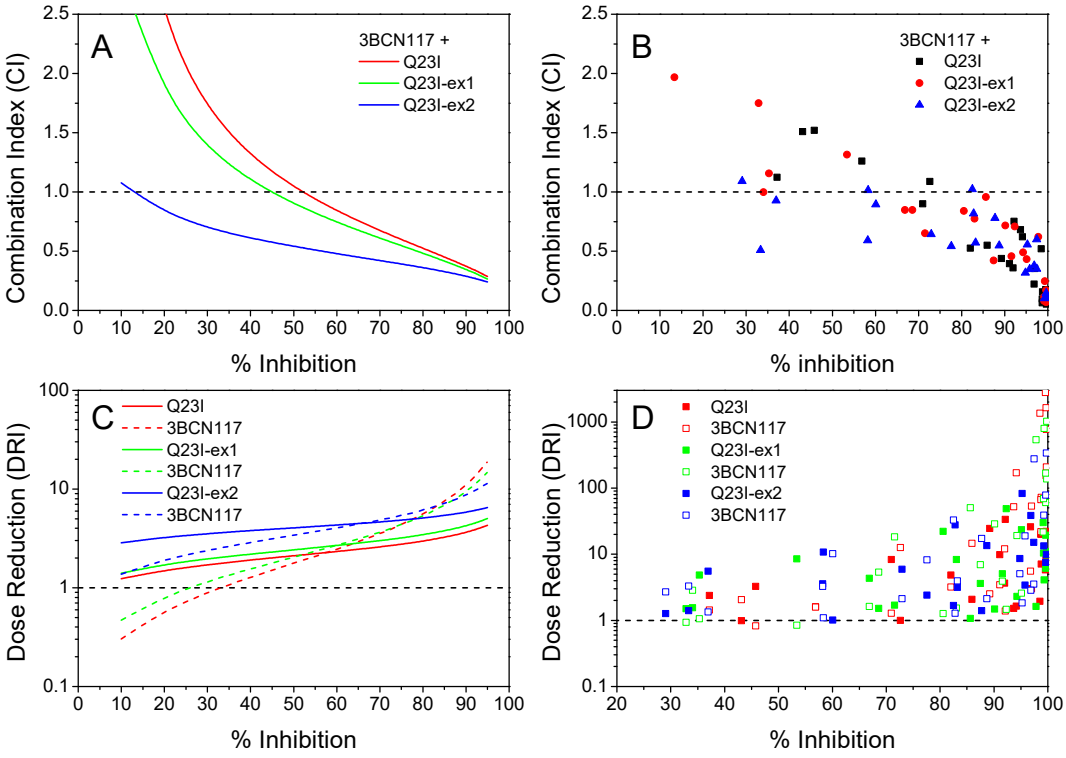

Figure S17. Combination Index (CI) (A and B) and Dose Reduction Index (DRI) with 3BNC117. CI and DRI (C and D) as a function of the percentage of inhibition calculated for the combination TZM-Bl assays between 3BNC117 and the each covNHR-N miniprotein. (A and C) correspond to the calculated values using the parameters derived from the Hill's plots for constant ratio combinations. (B and D) correspond to the individual combination data.

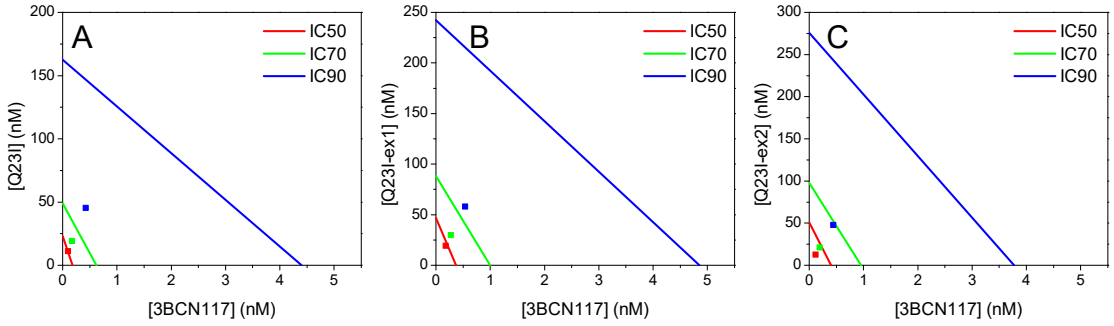

Figure S18. Isobolograms with 3BNC117. Isobolograms were calculated from the parameters of the Hill's plots using the constant ratio combination inhibition data between the different covNHR-N miniproteins, Q23I (A), Q23I-ex1 (B), Q23I-ex2 (C), and 3BNC117 for different inhibition percentages, as indicated. The continuous lines indicate purely additive effects and the symbols the observed effects the inhibitor: bnAb mixtures.

Table S5B. Combination inhibition assays with covNHR-N miniproteins and 2F5 or 4E10 in TZM-Bl assays using SF162 pseudoviruses

% inhibition in presence of 2F5 and Q23I.

	2F5 (nM)					
Q23I (nM)	166.67	55.56	18.52	6.17	2.06	0.00
500.00	99.72	99.99	99.87	98.70	99.80	97.56
166.67	99.88	98.46	97.60	96.91	95.11	91.73
55.56	98.74	94.38	90.71	83.83	75.88	57.28
18.52	98.27	91.90	82.65	66.72	47.54	20.39
6.17	99.53	94.21	77.09	60.05	28.57	4.53
0.00	97.32	91.54	79.82	50.44	38.43	-31.35

% inhibition in presence of 4E10 and Q23I.

	4E10 (nM)					
Q23I (nM)	166.67	55.56	18.52	6.17	2.06	0.00
500.00	99.69	100.01	99.52	98.88	99.38	97.42
166.67	100.21	98.28	96.36	94.48	92.10	90.32
55.56	97.34	89.32	85.80	77.53	68.99	50.72
18.52	93.49	81.66	69.84	56.55	42.05	32.53
6.17	89.56	78.44	63.88	43.72	35.83	-5.38
0.00	87.45	76.91	57.09	52.36	23.74	-7.51

% inhibition in presence of 2F5 and Q23I-ex1.

	2F5 (nM)					
Q23I-ex1 (nM)	166.67	55.56	18.52	6.17	2.06	0.00
500.00	100.31	99.78	99.82	99.22	99.42	102.36
166.67	100.06	97.70	96.14	93.75	90.33	87.89
55.56	98.89	96.15	88.78	78.83	74.34	53.49
18.52	96.71	93.01	80.65	74.03	54.72	30.66
6.17	98.72	89.80	79.72	62.35	53.17	24.31
0.00	95.03	88.44	82.22	54.57	48.58	4.50

Table S5B (Continuation). Combination inhibition assays with covNHR-N miniproteins and 2F5 or 4E10 in TZM-Bl assays using SF162 pseudoviruses

% inhibition in presence of 4E10 and Q23I-ex1.

	4E10 (nM)					
Q23I-ex1 (nM)	166.67	55.56	18.52	6.17	2.06	0.00
500.00	100.26	98.64	99.70	99.20	98.86	97.24
166.67	98.86	96.92	95.56	93.71	93.32	81.20
55.56	97.34	90.93	88.06	79.30	60.92	49.10
18.52	88.28	80.03	77.78	57.50	46.18	24.42
6.17	94.10	81.48	67.20	51.09	27.94	9.41
0.00	91.94	79.32	62.10	46.11	27.45	-6.52

% inhibition in presence of 2F5 and Q23I-ex2.

	2F5 (nM)					
Q23I-ex2 (nM)	166.67	55.56	18.52	6.17	2.06	0.00
500.00	100.09	99.41	99.95	98.63	96.71	97.24
166.67	99.48	98.77	97.76	93.81	89.25	84.19
55.56	97.69	95.88	84.57	82.42	72.20	62.19
18.52	97.42	92.07	84.45	88.30	56.23	31.13
6.17	95.98	89.89	76.28	61.92	41.03	-14.56
0.00	94.56	89.36	71.58	51.51	23.42	1.21

% inhibition in presence of 4E10 and Q23I-ex2.

	4E10 (nM)					
Q23I-ex2 (nM)	166.67	55.56	18.52	6.17	2.06	0.00
500.00	99.90	99.41	99.01	98.82	98.11	98.01
166.67	100.11	97.19	96.53	94.16	92.95	79.61
55.56	94.36	88.48	82.24	69.36	60.17	45.88
18.52	94.66	84.55	75.48	59.34	46.88	23.14
6.17	90.68	77.60	68.85	50.99	28.43	14.44
0.00	89.73	82.26	58.73	36.13	22.89	1.66

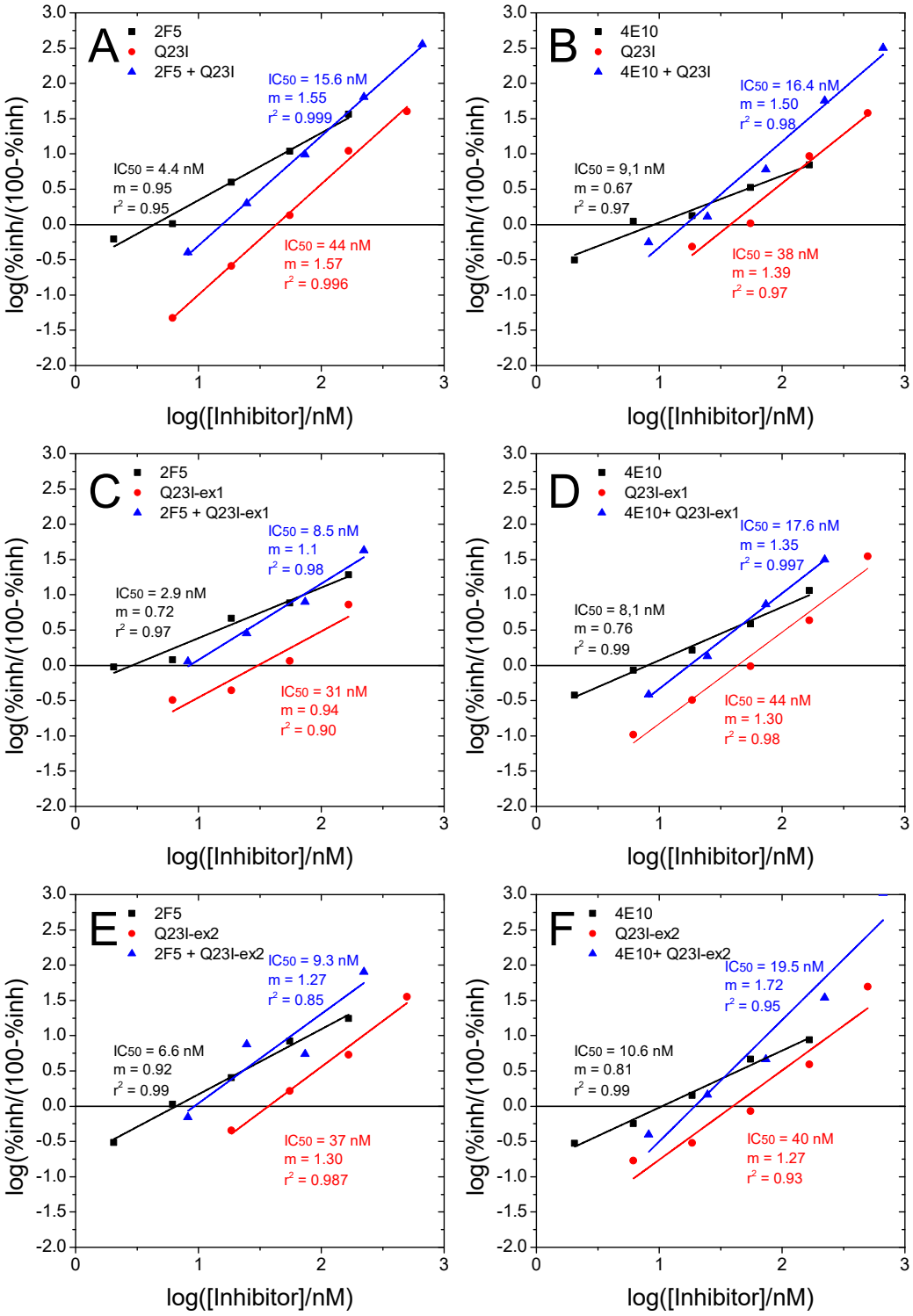

Figure S19. Combination TZM-Bl assays with 2F5 and 4E10. Hill's plots corresponding to the individual and combination inhibition assays between the covNHR-N miniproteins and 2F5 and 4E10 mAbs in TZM-Bl assays using SF162 pseudoviruses. Data correspond to constant [protein]/[mAb] molar ratio of 3:1 (diagonal data).

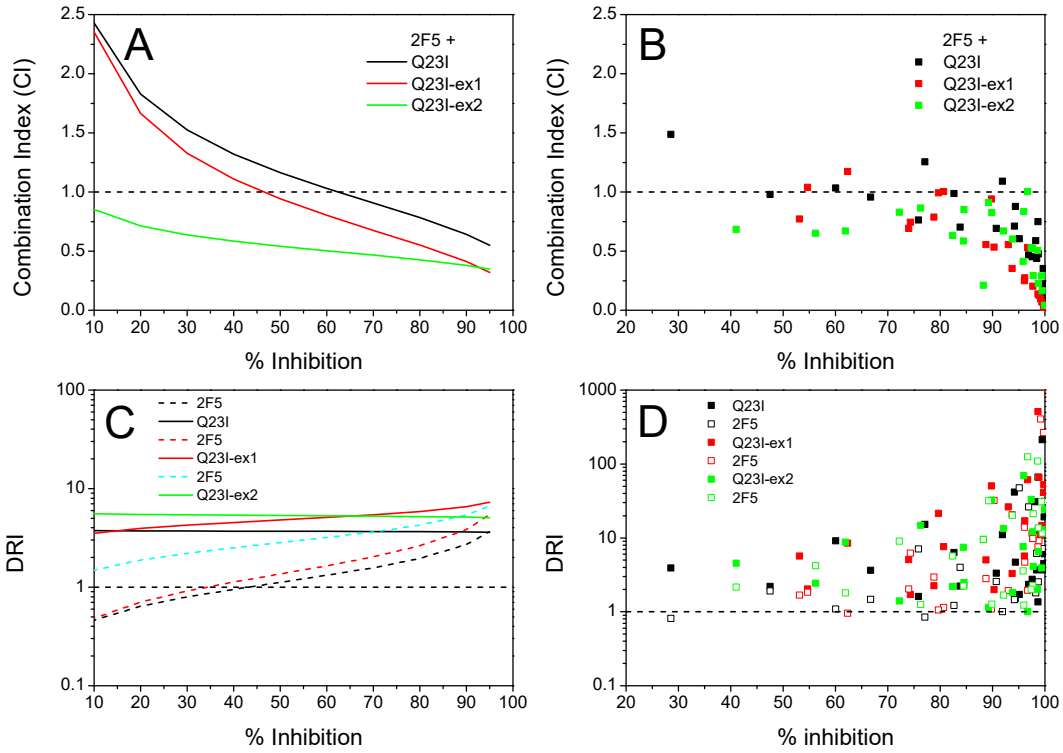

Figure S20. Combination Index (CI) (A and B) and Dose Reduction Index (DRI) with 2F5. Combination Index (CI) (A and B) and Dose Reduction Index (DRI) (C and D) as a function of the percentage of inhibition calculated for the combination TZM-Bl assays between 2F5 and the each covNHR-N miniprotein. (A and C) correspond to the calculated values using the parameters derived from the Hill's plots for constant ratio combinations. (B and D) correspond to the individual combination data.

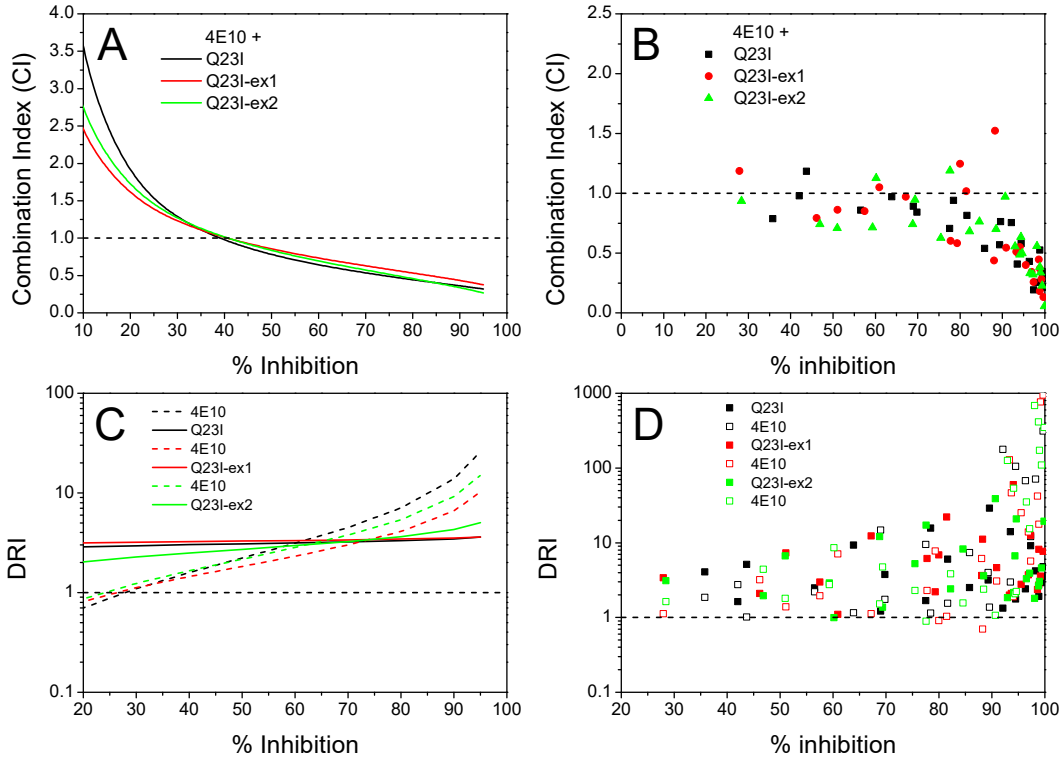

Figure S21. Combination Index (CI) (A and B) and Dose Reduction Index (DRI) with 4E10. Combination Index (CI) (A and B) and Dose Reduction Index (DRI) (C and D) as a function of the percentage of inhibition calculated for the combination TZM-Bl assays between 4E10 and the each covNHR-N miniprotein. (A and C) correspond to the calculated values using the parameters derived from the Hill's plots for constant ratio combinations. (B and D) correspond to the individual combination data.

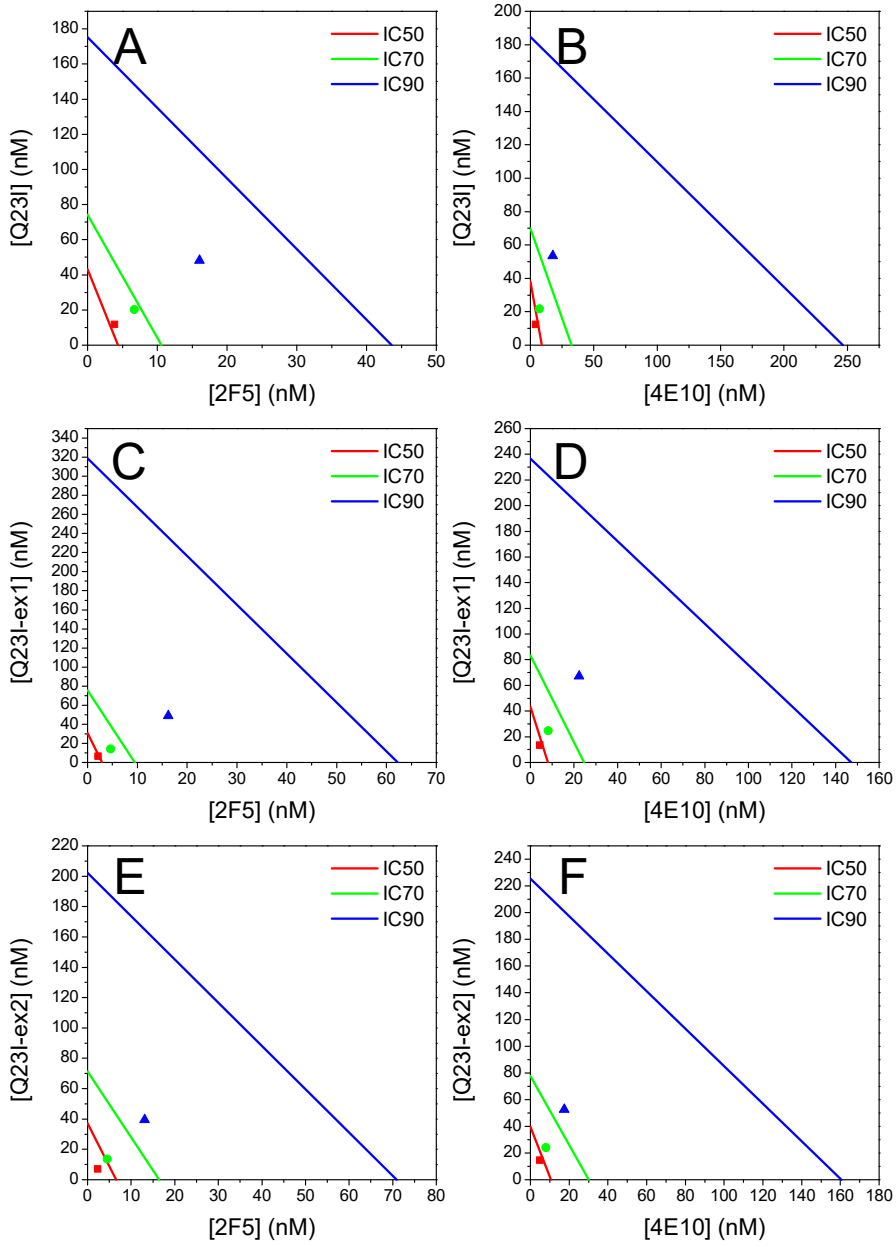

Figure S22. Isobolograms with 2F5 and 4E10. Isobolograms calculated from the parameters of the Hill's plots using the constant ratio combination inhibition data between the different covNHR-N miniproteins, Q23I (A,B), Q23I-ex1 (C,D), Q23I-ex2 (E,F), and 2F5 (A,C,E) and 4E10 (B,D,F) mAbs for different inhibition percentages, as indicated.

Table S5C. Combination inhibition assays with Q23I-ex1 and 3BNC117 in PMBC assays using SF162 and 97RW009 virus isolates.

% inhibition in presence of 3BNC117 and Q23I-ex1 (SF162 virus)

	3BNC117 (nM)						
Q23I-ex1 (nM)	20	6.67	2.22	0.74	0.25	0.08	0.00
60.00	99.91	99.66	98.33	87.98	87.25	83.70	75.97
20.00	99.46	98.85	90.70	67.92	64.89	56.01	46.71
6.67	98.12	96.24	79.10	32.71	16.51	16.20	48.07
2.22	98.01	94.04	63.74	12.54	16.41	21.21	16.41
0.74	97.28	89.86	57.47	35.21	11.39	-10.76	17.76
0.25	95.82	83.91	55.17	25.50	-17.03	1.46	15.36
0.00	92.89	89.86	55.69	10.97	-7.63	13.38	14.63

% inhibition in presence of 3BNC117 and Q23I-ex1 (97RW009 virus)

	3BNC117 (nM)						
Q23I-ex1 (nM)	20	6.67	2.22	0.74	0.25	0.08	0.00
60.00	99.67	98.84	98.89	95.12	95.37	95.89	95.12
20.00	99.56	97.46	91.00	78.66	76.35	73.52	75.58
6.67	98.30	91.77	80.98	61.44	53.73	52.96	37.53
2.22	97.63	86.12	65.04	48.84	49.61	35.73	44.22
0.74	97.43	84.06	62.72	37.28	20.05	9.77	22.88
0.25	95.37	79.18	58.61	45.50	20.31	14.65	24.68
0.00	94.86	79.18	50.64	50.39	25.19	-6.43	19.79

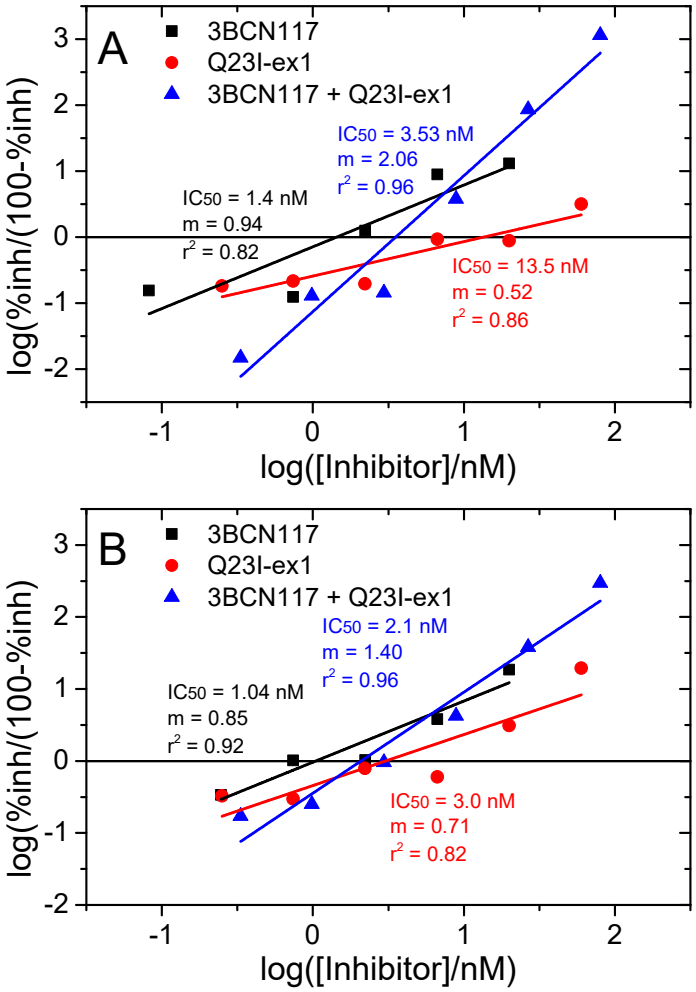

Figure S23. Combination PMBC assays with 3BNC117. Hill's plots corresponding to the individual and combination PBMC inhibition assays between the Q23I-ex1 and 3BNC117 using SF162 **(A)** and 97RW009 **(B)** virus isolates. Combination data correspond to constant [protein]/[mAb] ratio of 3:1 (diagonal data).

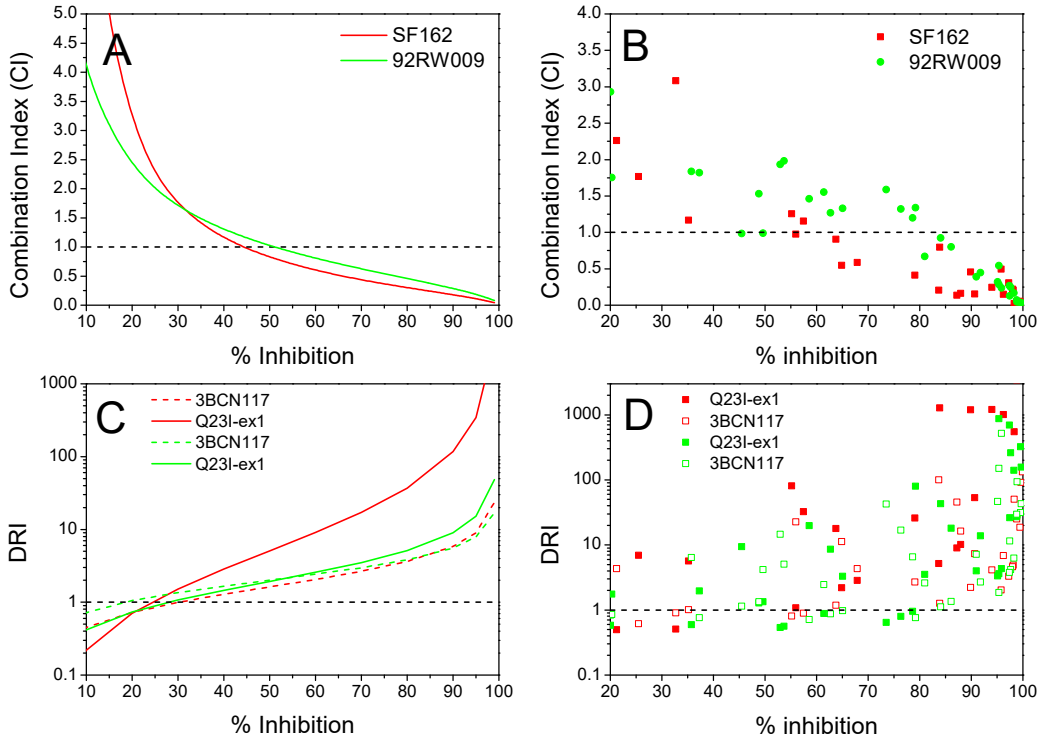

Figure S24. Combination Index (CI) (A and B) and Dose Reduction Index (DRI) with 3BNC117 in PMBC assays. CI (A and B) and DRI (C and D) as a function of the percentage of inhibition calculated for the combination PBMC assays between 3BNC117 and Q23I-ex1 for two virus isolates (SF162 and 97RW009). (A and C) correspond to the calculated values using the parameters derived from the Hill's plots for a constant ratio [protein]/[mAb] of 3:1. (B and D) correspond to the individual combination data.

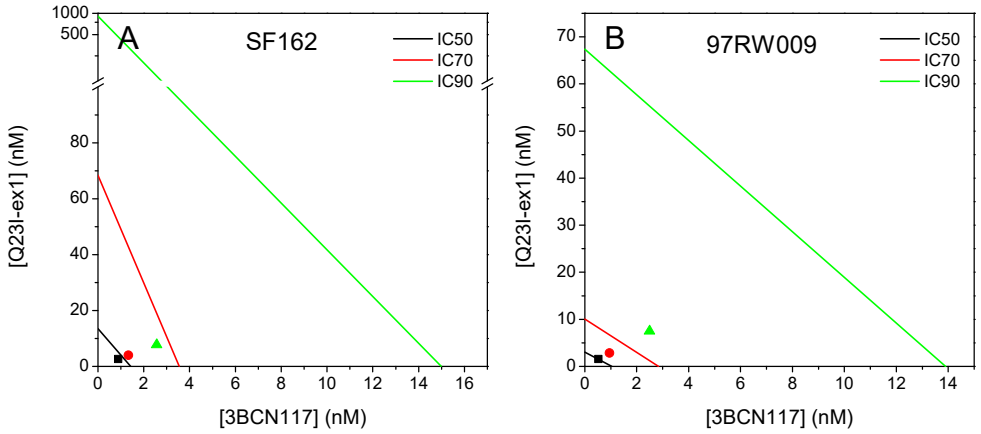

Figure S25. Isobolograms for 3BNC117 in PMBC assays. Isobolograms calculated from the parameters of the Hill's plots using the constant ratio combination inhibition data in PMBC assays with Q23I-ex1 and 3BNC117 for different inhibition percentages, as indicated. (A) SF162 virus; (B) 97RW009 virus.

9. Ex vivo replication assays

Table S6: Participants characteristics included in the APRIL study (Analysis of the Persistence, Reservoir and HIV Latency) who donated PMBCs for the *ex vivo* inhibition analysis

#ID	Sex	Clade	HIV acquistion	CDC stage	Age at visit (years)	Plasma HIV-1 RNA (log copies/mL)	CD4 at visit (/mm^3)	CD8 at visit (/mm^3)	CD4/CD8 ratio	ART at visit
VIR1	F	A	Unknown	A	41	2.96	313	952	0.33	3TC+DRV/r
VIR2	F	CRF02	Heterosexual	A	39	3.36	299	1105	0.27	ABC/3TC/DTG
VIR3	F	C	Heterosexual	A	39	2.55	722	454	1.59	TAF/FTC/BIC
VIR4	M	CRF02	Heterosexual	A	40	1.93	64	369	0.17	TDF/FTC/RPV
VIR5	M	A	MSM	A	31	3.24	784	724	1.08	/
VIR6	F	A1	Heterosexual	C	33	2.93	139	1666	0.08	3TC+ABC+DRV/r
VIR7	M	F1	Heterosexual	B	63	2.66	340	436	0.78	ABC/3TC+RPV
VIR8	M	B	MSM	B	59	2.30	407	710	0.57	ABC/3TC/DTG

MSM, Men who have sex with men; ART, antiretroviral treatment; 3TC, lamivudine; DRV/r, darunavir+ritonavir; ABC, abacavir; DTG, dolutegravir; TAF, tenofovir alafenamide; FTC, emtricitabine; BIC, bictegravir; TDF, tenofovir disoproxil fumarate; RPV, rilpivirine.

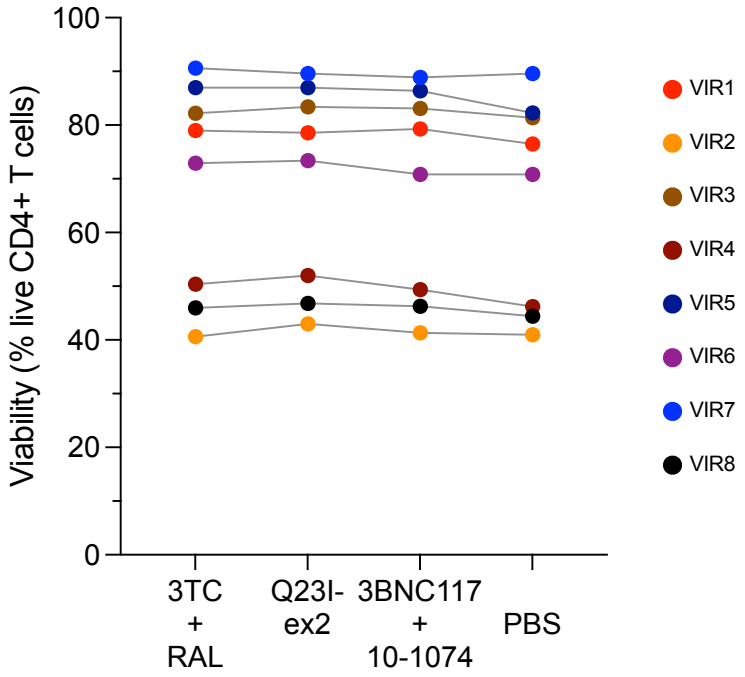

Figure S26: Ex vivo cell viability in presence of Q23I-ex2 or the 3BNC117+10-1074 mAbs or antiretroviral drugs. Isolated CD4+ T cells from viremic HIV-infected individuals failing antiretroviral therapy were treated with either: (i) antiretroviral drugs (raltegravir [RAL] + lamivudine [3TC], 200nM each), (ii) Q23I-ex2 (200nM), (iii) bnAbs (clones 3BNC117 + 10-1074, 7nM each) and (iv) control (PBS). The frequency (%) of live CD4+ T cells is depicted for each participant (VIR1 to 8). Each colored dot represents another viremic infected individual.

10. References

[1] A.M. Waterhouse, J.B. Procter, D.M.A. Martin, M. Clamp, G.J. Barton, Jalview Version 2—a multiple sequence alignment editor and analysis workbench, Bioinformatics 25 (2009) 1189–1191. https://doi.org/10.1093/bioinformatics/btp033.

[2] S. Jurado, M. Cano-Muñoz, D. Polo-Megías, F. Conejero-Lara, B. Morel, Thermodynamic dissection of the interface between HIV-1 gp41 heptad repeats reveals cooperative interactions and allosteric effects., Arch Biochem Biophys 688 (2020) 108401. https://doi.org/10.1016/j.abb.2020.108401.

[3] S. Jurado, C. Moog, M. Cano-Muñoz, S. Schmidt, G. Laumond, V. Ruocco, S. Standoli, D. Polo-Megías, F. Conejero-Lara, B. Morel, Probing Vulnerability of the gp41 C-Terminal Heptad Repeat as Target for Miniprotein HIV Inhibitors, J Mol Biol 432 (2020) 5577–5592. https://doi.org/10.1016/j.jmb.2020.08.010.

[4] M. Cano-Muñoz, J. Lucas, L.-Y. Lin, S. Cesaro, C. Moog, F. Conejero-Lara, Conformational Stabilization of Gp41-Mimetic Miniproteins Opens Up New Ways of Inhibiting HIV-1 Fusion, Int J Mol Sci 23 (2022) 2794. https://doi.org/10.3390/ijms23052794.

[5] S. Jurado, M. Cano-Muñoz, B. Morel, S. Standoli, E. Santarossa, C. Moog, S. Schmidt, G. Laumond, A. Cámara-Artigas, F. Conejero-Lara, Structural and Thermodynamic Analysis of HIV-1 Fusion Inhibition Using Small gp41 Mimetic Proteins, J Mol Biol 431 (2019) 3091–3106. https://doi.org/10.1016/j.jmb.2019.06.022.

[6] V. Buzon, G. Natrajan, D. Schibli, F. Campelo, M.M. Kozlov, W. Weissenhorn, Crystal Structure of HIV-1 gp41 Including Both Fusion Peptide and Membrane Proximal External Regions, PLoS Pathog 6 (2010) e1000880. https://doi.org/10.1371/journal.ppat.1000880.

[7] E. Krieger, G. Vriend, YASARA View-molecular graphics for all devices-from smartphones to workstations, Bioinformatics 30 (2014) 2981–2982. https://doi.org/10.1093/bioinformatics/btu426.

[8] Y. Liu, B. Kuhlman, RosettaDesign server for protein design, Nucleic Acids Res 34 (2006) W235–W238. https://doi.org/10.1093/nar/gkl163.

[9] P. Luo, R.L. Baldwin, Mechanism of Helix Induction by Trifluoroethanol: A Framework for Extrapolating the Helix-Forming Properties of Peptides from Trifluoroethanol/Water Mixtures Back to Water, Biochemistry 36 (1997) 8413–8421. https://doi.org/10.1021/bi9707133.

[10] M. Mirdita, K. Schütze, Y. Moriwaki, L. Heo, S. Ovchinnikov, M. Steinegger, ColabFold: making protein folding accessible to all, Nat Methods 19 (2022) 679–682. https://doi.org/10.1038/s41592-022-01488-1.

[11] T.-C. Chou, P. Talalay, Quantitative analysis of dose-effect relationships: the combined effects of multiple drugs or enzyme inhibitors, Adv Enzyme Regul 22 (1984) 27–55. https://doi.org/10.1016/0065-2571(84)90007-4.